

Universidade de São Paulo
Instituto de Astronomia, Geofísica e Ciências Atmosféricas
Departamento de Astronomia

Nilo Sérgio Souza de Almeida

**Explorando aglomerados de galáxias com
XMM-Newton e SDSS: propriedades físicas
do ICM e fotometria de galáxias**

São Paulo

2021

Nilo Sérgio Souza de Almeida

**Explorando aglomerados de galáxias com
XMM-*Newton* e SDSS: propriedades físicas
do ICM e fotometria de galáxias**

Dissertação apresentada ao Departamento de
Astronomia do Instituto de Astronomia, Geofísica
e Ciências Atmosféricas da Universidade de
São Paulo como requisito parcial para a ob-
tenção do título de Mestre em Ciências.

Área de Concentração: Astronomia

Orientador: Prof. Dr. Gastão Bierrenbach
Lima Neto

São Paulo

2021

Acknowledgements

Firstly, I want to thank my family for the support in these troubled times.

Secondly, my supervisor professor Gastão Lima Neto for the unlimited patience and guidance.

Thirdly, my close friends and the staff of the Astronomy Department of IAG-USP, who offered the comfort of a great infrastructure.

Finally, the financial support of Coordenação de Aperfeiçoamento de Pessoal de Nível Superior (CAPES) who made this work possible.

Resumo

Neste trabalho são investigadas as propriedades fotométricas (índices de cores) de galáxias de 20 aglomerados próximos ($0.03 < z < 0.3$), observados pelo XMM-*Newton* e presentes no SDSS, e são estabelecidas correlações com a emissão em raios-X do meio intra-aglomerado, discernindo entre aglomerados com e sem *cool-core*. Foco é dado para o estudo da metodologia da redução e análise de dados em raios-X, onde aplicamos a técnica desenvolvida em Snowden et al. (2008). Também apresentamos um novo método para subtrair galáxias de background e foreground nos casos em que informações espectroscópicas são limitadas, usando Kernel Density Estimators (KDEs) somos capazes de estimar a probabilidade de cada galáxia ser membro. Depois de obtermos perfis de temperatura e metalicidade, foi demonstrada a auto-similaridade evidente nos perfis térmicos. Embora há alguma variância nas regiões mais centrais (presença ou não de um *cool-core*), as regiões mais intermediárias e externas são muito similares. Além disso, comparando a metalicidade da região central ($r < 0.15 R_{500}$) com a intensidade dos *cool-cores*, foi demonstrada uma forte correlação onde aglomerados com *cool-cores* mais proeminentes são mais ricos em metais nas regiões centrais. Explorando a relação entre propriedades fotométricas e em raios-X, foi estabelecido que a metalicidade média, a temperatura e a cor da população galáctica estão intimamente relacionados, além de uma dependência com a massa do aglomerado. Nenhuma correlação com a presença de *cool-cores* foi estabelecida. É demonstrado que aglomerados menos massivos (mais frios) são mais ricos em metais e possuem uma população de galáxias mais azul. Também foi notado que sistemas menos massivos apresentam um gradiente de cor mais forte, enquanto que aglomerados mais massivos possuem uma população galáctica mais uniforme (e vermelha).

Abstract

We investigate the photometric properties (color indices) of galaxies from 20 nearby clusters ($0.03 < z < 0.3$), observed by *XMM-Newton* and present in the SDSS footprint, and find correlations with the intracluster medium X-ray emission, discerning between clusters that present or not a cool-core. Focus is given to the study of the methodology of the X-ray data reduction and analysis, where we employed the techniques presented in Snowden et al. (2008). We also develop a novel technique for subtracting background and foreground galaxies when few or none spectroscopical information is present, using Kernel Density Estimators (KDEs) to obtain PDFs representing the galaxy distribution in the $(g - r) \times r$ color-magnitude diagram, and assign a probability of membership for each galaxy. After obtaining temperature and metallicity profiles for our sample, we showed the self-similarity evident in the normalized temperature profiles. Although some scatter is present in the core region (presence or not of a cool-core), the profiles are very similar in the intermediate region and the outskirts. Also, comparing the core metallicity ($r < 0.15 R_{500}$) with the cool-core strength, we noted a strong correlation where clusters with more prominent cool-cores have a metal rich core region. By exploring the relationship between X-ray and photometric properties, we demonstrate that the ICM mean metallicity, mean temperature and mean $(g - r)$ color are intertwined, with an underlying dependence on mass. No correlation with the presence of cool-cores was found. It is shown that less massive (cooler) clusters are more metal rich and have a bluer galactic population. The likely explanation is the varying stellar mass over gas mass ratio. Moreover, we note that less massive clusters present a higher color gradient when compared to more massive systems, while the latter present a more uniform (and redder) galactic population.

List of Figures

2.1	Virgo Cluster	23
2.2	Abell 85	27
2.3	Jellyfish galaxy ESO 137-001	32
2.4	Red-sequence of ZwCl1215	33
3.1	XMM- <i>Newton</i> interior	36
3.2	XMM-MOS	37
3.3	MOS and pn CCDs	39
3.4	pn CCD	39
3.5	MOS1 damage	40
3.6	Count rates from unexposed corners	43
3.7	Filter wheel closed observations	44
3.8	Fluorescent lines	45
4.1	Lightcurve	49
4.2	Cheese mask of Abell 2065	49
4.3	Annuli used for the spectral fitting of the cluster Abell 85	51
4.4	A1795 and QPB spectra	52
5.1	The probability problem when binning	59
5.2	Bandwidth effects on KDEs	60
5.3	Bad field choice for Abell 85	61
5.4	KDE method schematics	64
5.5	Histogram of the distance to the red sequence	65

6.1	KDE background subtraction of A85	72
6.2	<i>Clean</i> PDF of A1795	72
6.3	Temperature profiles illustrating self-similarity	74
6.4	Profiles comparison with Pratt et al. (2007)	75
6.5	Central temperature drop dependence on core metallicity	76
6.6	Core metallicity versus pseudo-entropy ratio from (Leccardi et al., 2010)	77
6.7	(g-r)-X-ray correlations	78
6.8	Mean Z versus mean kT	78
6.9	Mean metallicity versus color gradient	80
6.10	Mean Temperature versus color gradient	82
A.1	RXCJ0043.4-2037, Abell 85, Abell 773.	93
A.2	Abell 963, Abell 1650, Abell 1689, Abell 1763.	94
A.3	Abell 1775, Abell 1795, RXJ2129.6+0005, E1455+2232.	95
A.4	Abell 2390, Abell 1914, Abell 2034, Abell 2065.	96
A.5	ZwCl1215, RXCJ1720.1+2638, Abell 1201, Abell 1413.	97
A.6	Abell 2261.	98
B.1	RXCJ0043.4-2037 dirty, field, and clean.	99
B.2	Abell 85 dirty, field, and clean.	99
B.3	Abell 773 dirty, field, clean.	100
B.4	Abell 963 dirty, field, clean.	100
B.5	Abell 1763 dirty, field, clean.	100
B.6	Abell 1689 dirty, field, clean.	100
B.7	RXJ2129.6+0005 dirty, field, clean.	101
B.8	Abell 1650 dirty, field, clean.	101
B.9	Abell 1795 dirty, field, clean.	101
B.10	Abell 1775 dirty, field, clean.	101
B.11	NSCS-J—E1455+2232 dirty, field, clean.	102
B.12	Abell 2390 dirty, field, clean.	102
B.13	Abell 1914 dirty, field, clean.	102
B.14	Abell 2034 dirty, field, clean.	102
B.15	Abell 2065 dirty, field, clean.	103

B.16 ZwCL 1215 dirty, field, clean.	103
B.17 Abell 781 dirty, field, clean.	103
B.18 RXCJ1720.1+2638 dirty, field, clean.	103
B.19 Abell 1201 dirty, field, clean.	104
B.20 Abell 1413 dirty, field, clean.	104
B.21 Abell 2261 dirty, field, clean.	104
C.1 RXCJ0043.4-2037, Abell 85, Abell 773	105
C.2 Abell 963, Abell 1763, Abell 1689	106
C.3 Abell 1795, E1455+2232, Abell 2390	106
C.4 Abell 1914, Abell 2034, Abell 2065	106
C.5 ZwCl1215, Abell 1413, Abell 1201	107
C.6 Abell 2261, Abell 1650.	107

List of Tables

6.1	Cluster sample	69
6.2	Overall cluster properties	81

Contents

1. <i>Introduction</i>	17
2. <i>Clusters of Galaxies</i>	21
2.1 Historical Prelude	21
2.2 General properties of galaxy clusters	22
2.3 The intracluster medium	26
2.3.1 Cooling flow and cool-core clusters	29
2.3.2 Differences between cool-core and non-cool-core clusters	30
2.3.3 Galaxy interactions with the ICM	31
3. <i>XMM-Newton: Instruments and Particle Background</i>	35
3.1 The XMM-Newton Observatory	36
3.2 European Photon Imaging Camera	37
3.2.1 Charge-Coupled Devices	37
3.2.2 Micrometeoroid damage and pixel defects in EPIC	39
3.2.3 Pulse-height amplitude conversion to energy or wavelength	40
3.3 The particle induced background of XMM-Newton observations	41
3.3.1 Quiescent Particle Background (QPB)	42
3.3.2 Soft Protons (Flares)	43
3.3.3 Fluorescent Lines	44
4. <i>X-ray Data Reduction</i>	47
4.1 Methodology of the X-ray Data Reduction	47
4.1.1 Calibration files and clean event files	47

4.1.2	Cheese and the masking of point-sources	48
4.1.3	X-ray peak detection and annuli determination	50
4.1.4	Modelling and subtracting the Quiescent Particle Background	50
4.2	Spectral fitting	51
4.3	Summary	54
5.	<i>Galaxy selection using Kernel Density Estimators</i>	57
5.1	Motivation and the classical binning method	57
5.2	Kernel density estimators	59
5.2.1	Statistical background subtraction using KDEs	61
5.2.2	Overall photometric properties	63
5.3	Final remarks	65
6.	<i>Results and Analysis</i>	67
6.1	Sample and overall cluster properties	67
6.2	Applicability and performance of the X-ray spectral fitting and data reduction algorithm	69
6.3	The KDE method for background galaxy subtraction	70
6.4	The “universal” temperature profile and self-similarity	71
6.5	Metal content in the core of galaxy clusters	73
6.5.1	Comparison with Lecardi et al. (2010) results	74
6.6	Correlations between galaxy photometry and X-ray properties	76
7.	<i>Conclusion</i>	83
	<i>Bibliography</i>	85
	<i>Appendix</i>	91
A.	<i>Temperature and metallicity profiles</i>	93
B.	<i>Color-magnitude diagrams</i>	99
C.	<i>Model particle background subtracted images</i>	105

Introduction

The interplay between galaxies and their environment is a long withstanding topic of discussion in astrophysics. Galaxy clusters are permeated by a hot ($\sim 10^7$ – 10^8 K) and rarefied gas, that radiates in X-ray mainly through thermal bremsstrahlung (Sarazin, 1986). The interaction between galaxies and this intra-cluster medium (ICM) leaves footprints in these galaxies, and conversely the galaxies contribute to the ICM enrichment with metals, stars (intra-cluster light), energy, among others.

As the metals originate from stellar populations inside galaxies (e.g., Heckman et al., 1990), Böhringer and Werner (2010) argue that the bulk of the metal enrichment happens due to early starbursts, with little to no evolution afterwards. Many (e.g., De Grandi and Molendi, 2001) saw an increase in metallicity in the core region, showing that there is some evolution, at least in the innermost regions, but still corroborating the early enrichment hypothesis (see also Vogelsberger et al., 2018). How, where, and when these metals were thrown into the ICM, and how it correlates with the photometric properties of the galaxy population, are a central topic of investigation in this work. This problem involves both the ICM and galaxy chemical evolution, together with physical mechanisms that push the metal enriched interstellar gas from galaxies (for instance, ram-pressure and supernovae explosions).

Galaxy clusters may fall victims of being seen as a merely agglomeration of galaxies, while in actuality the bulk of its mass lies in the form of X-ray emitting gas and more importantly as dark matter (Sarazin, 1986; Böhringer and Werner, 2010). As X-ray objects, they are primarily studied by observatories aboard satellites, since the atmosphere is opaque to high energy photons. The telescopes that were more relevant in the last three decades were the *Chandra* observatory, run by NASA, and the *XMM-Newton*, launched by

the European Space Agency, and from which archival data were obtained for this work.¹

A great part of this work deals with X-ray observations of cluster of galaxies, with special attention to data reduction and, in particular, the background X-ray emission and energetic particles that are always present. We will concentrate on the reduction and analysis of XMM-*Newton* observations of extended sources (which differs in some aspects from the analysis of point-sources, such as distant AGNs).

We discriminate between background components whose origins are either of instrumental (particle) or of cosmic (X-ray photons) origin (Snowden et al., 2008) and subtract the former and fit the second explicitly using models in the spectral fitting process. We avoid usage of blank-sky data, which takes average images of regions devoid of source emission to estimate the background, because that may change with time, depends on the galactic coordinates, and it does not offer information on the background components.

Due to the time and resources necessary for a complete spectroscopic coverage of a single cluster of galaxies, cluster membership identification using solely photometrical information is of the essence. While cluster membership is of course a problem to be solved, the reverse problem, of identifying background galaxies, is also of great importance for several reasons, most notably weak lensing analysis. While the photometric redshift estimations of the SDSS (Sloan Digital Sky Survey) are notoriously problematic, surveys in current development, such as the JPAS (Javalambre Physics of the Accelerating Universe Astrophysical Survey) with its 56 optical narrow band filters, will offer photometric redshifts with unprecedented precision (Benítez et al., 2015).

To explore photometric properties of the galaxy population we must solve the problem of assigning galaxy membership with limited or no spectroscopic information, using SDSS data. We improved on existing methods (Pimbblet et al., 2002; Kodama and Bower, 2001) to establish a probability of galaxy membership, using optical and near IR broad band imaging. Our novel method consists of using kernel density estimators (KDEs) to determine the probability of membership of every galaxy, and also improving on this probability with photometric redshift information (provided by the SDSS).

¹ Also noteworthy were ROSAT (*Röntgensatellit*), a German satellite (with UK and NASA collaboration), BeppoSAX, a joint Italian–Netherlands project, and ASCA and Suzaku both operated by JAXA and NASA. More recently, eROSITA started its operation and is currently doing the deepest X-ray all-sky survey.

Another goal of this work is to implement a so-called pipeline based on the Extended Source Analysis Software (ESAS) package (Snowden, 1998) that will go from data acquisition (from publicly available archives) to the production of temperature and metallicity radial profiles, taking into account all possible sources of contamination of the data.

This Master's dissertation is organized as follows: in the next chapter it is outlined some general properties of galaxy clusters; chapter 3 deals with the XMM-*Newton* satellite instrumentation and more importantly the particle background; chapter 4 explores the X-ray data reduction and analysis method from Snowden et al. (2008) and implemented in this work; chapter 5 presents the novel method of exclusion of background (and foreground) galaxies using KDEs as well general optical data analysis; chapter 6 showcases our results and analysis, as well pointing flaws and advantages of our methods; finally, chapter 7 summarizes our conclusions, possible improvements and future prospects.

Clusters of Galaxies

2.1 Historical Prelude

The year of 2020 marked the hundredth anniversary of the famous “Great Debate”, held in April 1920 in Washington, USA. Under the topic “The Scale of the Universe”, forty-minute talks were given by Harlow Shapley of the Mount Wilson Observatory and Herber D. Curtis of the Lick Observatory. The main focus of the talks were the nature of the so-called “spiral nebulae” and the size of our own Galaxy (Hoskin, 1976), and despite their short duration they made history.

Although the subject of galaxy clusters was not exactly debated, these talks, followed by the more complete 1921 set of papers, are of extreme importance for the history of extragalactic astronomy. Not only they summarized the landscape of ideas that were mainstream, but shortly after in 1924, Edwin Hubble observed variable stars of type Cepheid in NGC 6822 and Andromeda which once and for all established the extragalactic nature of the “spiral nebulae”. This of course, opened up the modern study of galaxy clusters, since they were newly understood as cosmological objects of megaparsec scales.

But even before we understood the extragalactic nature of these mysterious nebulae, their first written recorded observations were done by Charles Messier in 1784. While compiling his well-known catalogue, he noticed a concentration of nebulae in the direction of the Virgo constellation, which is today known as the Virgo Cluster. Curiously, the main motivation of Messier’s study of nebulae was to not confuse them with passing comets. Contemporary to Messier, William Herschel also took note of unusual concentrations of nebulae in the direction of the Coma Berenice constellation, today known as the Coma Cluster. He noted a “remarkable collection of many hundreds of nebulae”. Other nota-

ble clusters or groups observed by Herschel are Leo, Ursa Major, Hydra and NGC 4169 (Biviano, 2000).

At the beginning of the 1930s, the idea of an expanding universe took root and extragalactic astronomy started to quickly flourish. Eventually the study of the large scale distribution of galaxies showed that groups and clusters of galaxies are not only far from rare, but are arguably the structural building blocks of the Universe (e.g., Shapley, 1933; Shane and Wirtanen, 1954; Zwicky et al., 1968).

An important aspect of the study of galaxy clusters is the construction of catalogs. Probably, the most influential “hand-made” catalog (i.e., before catalogs made by automatically identifying galaxies in digitized images) is from Abell and collaborators (Abell, 1958; Abell et al., 1989). The Abell cluster catalog is all-sky (although strongly affected by the avoidance zone) with about 4000 objects (and roughly 10% of false positives). The strength of the Abell catalog is that it is based on objective criteria, selecting rich clusters (more than 30 bright galaxies inside $1.72'/z$, where z is the estimated cluster redshift).

At the turn of the 21st century it became common to build catalogs from galaxies automatically identified in surveys. The SDSS¹ in particular revolutionized the field due to its depth and multi-band coverage of the sky (York et al., 2000). It uses a dedicated 2.5m telescope at Apache Point Observatory in New Mexico. Initially comprising 2099 deg² and using the five bands u, g, r, i, z , their primary objective was to investigate the large scale structure observed in the distribution of galaxies and quasars, with the first data release in 2003 (Abazajian et al., 2003). Today, at the 16th data release (DR16), the SDSS survey covers 14,555 square degrees with over 1.23 billion objects catalogued including 208 million galaxies, of which almost 1.8 million have measured spectra.

2.2 General properties of galaxy clusters

Galaxy clusters, as the largest collapsed structures in the universe, may contain hundreds to thousands of galaxies in the case of the richest systems. However, since the works of Zwicky in the 1930s, the first to propose the existence of an “invisible matter”, it is known that clusters are not merely a collection of galaxies (Böhringer and Werner, 2010). This idea was further corroborated in the 1970s with the launch of Uhuru, the first

¹ www.sdss.org

X-ray observatory to orbit Earth, which provided evidence that clusters are also strong emitters of X-ray radiation. A few years later, after the first observations of their X-ray spectra, it was established that this emission originates from a hot plasma, usually called the intracluster medium (ICM).



Figure 2.1: The nearby Virgo Cluster. The image has about 2×1.4 square degree. At the lower left, we can see the giant elliptical galaxy, M87. Credit: NOIRLab/NSF/AURA (image obtained with the KPNO 0.9-meter telescope).

Clusters of galaxies are, according to the hierarchical scenario, one of the last structures to collapse in the Universe, within the “Cosmic Web”, a network of filamentary structures dominated by dark matter. Specifically, they reside in “knots” or in the intersection of filaments and span a range of masses from $10^{13}M_{\odot}$, which are more commonly called groups, up to a few $10^{15}M_{\odot}$, such as the Virgo (figure 2.1) and Coma clusters.

The main components of rich clusters in terms of mass may be divided in baryonic and dark matter, where the baryonic component is further divided in stars (mostly observed in galaxies) and diffuse matter, the ICM. In rich clusters, galaxies only comprise 2 – 5%, and the ICM about 12 – 15%. The bulk of the mass of clusters are in the form of dark matter, making up to about 85%. Although the ratio between baryonic and dark matter is roughly independent of the cluster total mass, the ratio of galaxy to ICM mass varies with total mass: the larger the cluster mass, the larger the ICM mass with respect to the mass in galaxies (Laganá et al., 2013).

The size of diffuse objects is always a matter of definition. Taking the Abell radius, $1.72'/z$ and using the approximation $cz = H_0 D$, where H_0 is the Hubble-Lemaître constant and D the distance, we have $R \sim 2.1h_{70}^{-1}$ Mpc, the typical radius of rich clusters.

Nowadays, it is common to refer to groups and clusters size with respect to R_{200} . This size is defined in terms of the ratio between the mean density of the object, ρ_{200} , and the mean density of the universe:

$$\frac{\rho_{200}}{\Omega_M \rho_{\text{cr}}(z)} = 200 ; \quad \rho_{200} \equiv \langle \rho(R_{200}) \rangle = \frac{M_{200}}{4\pi R_{200}^3/3}, \quad (2.1)$$

where Ω_M is the density parameter of the universe today and $\rho_{\text{cr}}(z)$ is the critical density at redshift z . For practical reasons², we often see the R_{500} being used to characterize the size of a cluster or group. For realistic mass distributions, $R_{500} \approx 0.7R_{200}$. The radius R_{500} is defined the same way as R_{200} , but the density ratio in Eq. (2.1) is 500.

The use of R_{200} is motivated by the top-hat model of spherical collapse in a Einstein-de Sitter universe (a.k.a., SCDM model). In this simple model, the virial radius of a collapsing sphere is $R_{\text{vir}} \simeq R_{170}$, which was then rounded to R_{200} .

Clusters are dominated by a population of early-type galaxies, elliptical and lenticulars, in contrast with the field where spiral galaxies abound. In groups, we have a mixed situation, with both early and late-type can be the dominant morphological type.

The total mass in clusters is of course not directly observed. Nowadays, we have basically three forms to estimate the cluster masses: (I) using the virial theorem, (II) the hydrostatic equilibrium, and (III) gravitational lensing effect.

The first method employed to determine the total mass in clusters was based on the virial theorem by Fritz Zwicky in 1933. It is based on the assumption that galaxies are in equilibrium within the cluster gravitational potential, so that measuring their velocity dispersion may be used to estimate the total mass.

Besides the fact that is not always clear if the equilibrium hypothesis is valid (many clusters show sign of recent dynamical activity related to past or even present mergers), there are additional difficulties. First, we only have access to one component of the 3 dimensional velocity vector of each galaxy, along the line-of-sight. Second, we only have 2 coordinates for each galaxy, perpendicular to the line-of-sight. Finally, for most clusters,

² R_{500} is roughly the radius up to where a bright cluster X-ray emission can be detected with an observation of a few tens of kilo-seconds.

we have only tens of galaxies with spectral observations (the velocity is obtained measuring the redshift of each galaxy).

Therefore, not only we have to rely on the equilibrium hypothesis but also on the hypotheses on the spatial distribution and velocity distribution (isotropical or radial or something else). Nevertheless, this is a successful method of mass determination since simulations show that an accuracy better than one order of magnitude is achievable for the total mass.

Another method, also based on an equilibrium hypotheses, is based on the hydrostatic equilibrium of the ICM and its X-ray observation. The short relaxation time-scale of the gas makes it a useful probe of the gravitational potential.

Assuming an ideal gas and spherical symmetry, the total mass can be obtained by the hydrostatic equilibrium equation:

$$\frac{1}{\rho} \vec{\nabla} P = -\vec{\nabla} \Phi \quad \Rightarrow \quad M(r) = -\frac{kT}{G \mu m_{\text{H}}} r \left(\frac{d \ln \rho}{d \ln r} + \frac{d \ln T}{d \ln r} \right), \quad (2.2)$$

where, μ is the mean-molecular weight (about 0.6 for a totally ionized gas of low metallicity), m_p is the proton mass, $T(r)$ is the gas temperature radial profile (sometimes, we just use $T(r) = T_0$, assuming an isothermal gas), and $\rho(r)$ is the gas density radial profile.

Another method of galaxy cluster mass determination based on the hydrostatic equilibrium of the ICM is the thermal Sunyaev-Zel'dovich effect, which in combination with X-ray observations can constraint the ICM mass. It was first detected at a high level of significance in 1978 (Birkinshaw et al., 1978). It originates when photons from the Cosmic Microwave Background (CMB) interact with hot electrons in the ICM, gaining energy due to inverse Compton scattering. Therefore it is dependent on the electron temperature and electron density (Birkinshaw, 2004).

In section 2.3 we will show how X-ray observations are used to measure the density and temperature of the ICM.

The third method to measure the total mass of clusters are based on the effect of gravitational lensing. This method has a great advantage of not depending on any equilibrium hypothesis.

The idea, based on the general theory of relativity, is that the cluster mass acts like a lens, deflecting and deforming the images of background galaxies around the line-of-sight of the cluster. The last decades saw the rise of a particular method of gravitational

lensing analysis called weak-lensing. It consists of the weak shape distortion, or shear, and magnification of the images of background galaxies by the potential well of the cluster. It has a statistical nature, since there must be a sufficient number of lensed background galaxies, and also the information concerning their true properties is never complete, which makes the assumption of a few hypotheses mandatory (Umetsu, 2020).

2.3 The intracluster medium

The diffuse intracluster plasma has a typical temperature between 10^7 to 10^8 K, which we find more generally in the literature in terms of the energy kT and in units of kilo electron-volt. Therefore the typical temperature of clusters is between 2 keV and 12 keV, approximately. Below about 2 keV the object is usually classified as a galaxy group. The gas has also a very low density, reaching up to 10^{-2} cm^{-3} in the central cluster region, much lower than the typical interstellar gas in disk galaxies.

The hot gas between galaxies in clusters is not of primordial composition, devoid of any metals. On the contrary, the ICM has a mean metallicity around 1/3 of the solar value (Mushotzky and Loewenstein, 1997). Since metals are produced by stars and stellar formation occurs almost solely in galaxies, the ICM is enriched by metals which resided in its cluster member's interstellar medium, which is stripped by ram-pressure or ejected by supernovae wind.

Such a tenuous hot gas is a powerful X-ray emitter. The main mechanism is the free-free scattering of electrons by ions, known as thermal *bremsstrahlung* (breaking radiation, in German). For a fully ionized, optically thin gas, This process produces a continuum emission with an emissivity, $\varepsilon(\nu)$, as a function of the frequency ν , given by (Rybicki and Lightman, 1986):

$$\varepsilon_\nu = 6,84 \times 10^{-38} Z^2 n_e n_i T^{-1/2} e^{-h\nu/kT} g(E, T) \text{ erg s}^{-1} \text{cm}^{-3} \text{Hz}^{-1}, \quad (2.3)$$

where Z is the mean atomic number, n_e and n_i are the electron and ion number densities, respectively, and $g(E, T)$ is the Gaunt factor, that takes into account relativistic and quantum corrections. For a plasma with temperature above ~ 1 keV, this is the main cooling process.

Integrating Eq. (2.3) over all frequencies, we obtain the bolometric bremsstrahlung

emission:

$$\varepsilon = 1,4 \times 10^{-27} Z^2 n_e n_i T^{1/2} g(T) \text{ erg s}^{-1} \text{ cm}^{-3}. \quad (2.4)$$

From Eq. (2.4), we see that the broad band X-ray emissivity is proportional to $n^2 T^{1/2}$, i.e., depends much more on the number density than on the gas temperature. In other words, an X-ray broad band image gives approximately a projected gas density map, such as shown in Fig. 2.2, as we will show this explicitly below.



Figure 2.2: Abell 85 with its X-ray emission in purple, as observed by the Chandra observatory, overlaid an optical image showing the galaxies (and some Milky Way stars). The X-ray emission is roughly proportional to the projected gas density. X-ray image (NASA/CXC/SAO/A.Vikhlinin et al.); Optical (SDSS).

The second most important cooling mechanism is though collisional excitation, which is the way that emission lines are produced in the ICM. For galaxy clusters, with temperature above $kT \sim 2$ keV, the most important lines are from Fe XXV and Fe XXVI around energy of 6.8 keV (rest-frame). With the present day X-ray facilities in space, these lines are observed as a blend. Since these lines are formed when the iron ion decays to the fundamental level, they are called Fe K lines.

At energies around 1 keV we also observe another blend of lines, the Fe L lines. This blend is stronger in groups of galaxies, that have $kT \sim 1$ keV.

Other notable lines are emitted by some alpha elements (O, S, Si, Mg) and Ni (an iron group element). The lower the gas temperature, the more important are the line emission

with respect to the bremsstrahlung continuum.

There is a feature in the observed X-ray spectrum that we must take into account, which is due to the absorption along the line-of-sight. This absorption comes mainly from the neutral HI in our galaxy. It starts to get noticed at energies around 2 keV and get stronger for lower energies. Even observing in a direction perpendicular to the Galactic plane, where the HI column density is roughly 10^{-20} cm^{-3} , the observed X-ray spectra is almost completely absorbed at energies below $\sim 0.2 \text{ keV}$ (wavelength above $\sim 60 \text{ \AA}$).

The observed X-ray surface brightness is proportional to the projected emissivity,

$$I(R) = \int_{-\infty}^{+\infty} \varepsilon(r) dz = 2 \int_R^{\infty} \varepsilon(r) \frac{r dr}{\sqrt{r^2 - R^2}}, \quad (2.5)$$

where, for the last term, it is assumed spherical symmetry. If we further simplify, assuming that most of the emission is from thermal bremsstrahlung, then we have:

$$I(R) \propto 2 \int_R^{\infty} n^2(r) T^{1/2}(r) \frac{r dr}{\sqrt{r^2 - R^2}}, \quad (2.6)$$

As we will see in the temperature profiles of our sample of clusters (appendix A), the range in gas temperatures (excluding shocks or intense heating by AGN jets and SN explosion) is at most a factor of 10 (usually even less). On the other hand, the gas density can be as low as $\sim 10^{-5} \text{ cm}^{-3}$ at the virial radius. Therefore, we can assume an isothermal profile with temperature T_0 and the surface brightness becomes:

$$I(R) \propto T_0^{1/2} \int_R^{\infty} n^2(r) \frac{r dr}{\sqrt{r^2 - R^2}}, \quad (2.7)$$

showing that observing $I(R)$ we can derive the density profile $n(r)$.

One of the most popular analytical forms used to describe $n(r)$ is the β -model, introduced by Cavaliere and Fusco-Femiano (1976):

$$n(r) = \frac{n_0}{[1 + (r/r_c)^2]^{3\beta/2}}, \quad (2.8)$$

where r_c is a scale radius known as core-radius, n_0 is the central density, and β is a shape parameter that controls the asymptotic power-law behavior for $r \gg r_c$.

The β -model, besides being very simple, has a very useful property: the corresponding isothermal surface brightness radial profile has also the same mathematical form, i.e.:

$$I(R) = \frac{I_0}{[1 + (R/R_c)^2]^{3\beta-1/2}}, \quad (2.9)$$

where I_0 is the central surface brightness.

2.3.1 Cooling flow and cool-core clusters

The ICM loses energy through photon emission and, therefore, should get colder with time. The time-scale for an optically thin gas to cool can be estimated approximately as:

$$t_c \simeq \frac{E}{dE/dt}, \quad (2.10)$$

where, E is the thermal energy of the gas, $E = (3/2)nkT$ for a ideal, monoatomic gas (by far, most of the ions are single protons).³ Assuming the main cooling process is the thermal bremsstrahlung mechanism, we may use the fact that $dE/dt = \varepsilon \propto n^2 T^{1/2}$. Therefore, the cooling time is

$$t_c \approx 9.3 \times 10^9 \frac{(kT_{\text{keV}})^{1/2}}{n_3} \text{years}, \quad (2.11)$$

where we have units of keV for the “temperature” kT and $n_3 \equiv n/10^{-3} \text{ cm}^{-3}$. Clearly, the higher the density, the shorter is t_c (the dependence in temperature is weaker, going with its square-root). In the central region of clusters, where the numerical density is high enough, the cooling time is smaller than the age of the cluster. This short time-scale led Fabian and Nulsen (1977) to propose a subsonic accretion of cooling gas in clusters, the so-called cooling-flow. The picture we had up to the turn of the century is described by (Fabian et al., 1984; Nulsen, 1986).

We can define a characteristic cooling radius, r_c , where the cooling-time is equal to the age of the cluster. Within a factor of 2 or 3, we can adopt H_0^{-1} as the cluster age. Thus, by solving the following equation:

$$\frac{1}{H_0} = t_c, \quad (2.12)$$

we can estimate r_c , if we know $n(r)$, the density radial profile. It turns out that, for clusters with high central density, r_c is usually between a few 10s to a few 100s kpc.

An order of magnitude way of computing how much mass deposits because of the cooling-flow is done by dividing the gas mass inside the cooling radius by the cooling time-scale. We have, thus:

$$\frac{dM}{dt} \approx \frac{M(r_{\text{cf}})}{t_{\text{cf}}} \approx 500 \left(\frac{[kT_{\text{keV}}]^{1/2}}{n_3} \right)^{-1} M_{\odot}/\text{yr}. \quad (2.13)$$

³ Some authors, (e.g., Peterson and Fabian, 2006), define the cooling time-scale in terms of the gas enthalpy divided by the energy loss ratio. The cooling time thus defined is a factor 5/3 larger than t_c defined in Eq. (2.10). the argument behind this is that the gas is also compressed as it cools, raising its heat capacity compared to the cooling of an incompressible gas.

The above equation implies that a large mass may deposit in the center of clusters. If this flow lasts for roughly 10^{10} years, we should have something between 10^{12} to $10^{13} M_{\odot}$ of gas piling up in the center of cooling flows. It was thought that such a high quantity of gas could be the main mechanism behind the formation of cD galaxies⁴ (Prestwich and Joy, 1991).

However, during the 1990s, this cooling-flow scenario showed some problems. Such a huge gas mass flowing to the center should quickly cool and form molecules and then stars, but neither one was observed in a quantity compatible with the predicted cooling flow. The nail in the coffin, so to speak, came with RGS spectra obtained from *cool-core* clusters that show little evidence for gas cooling below $1 - 2$ keV (Kaastra et al., 2001; Peterson et al., 2001). These led to revisions of the classical cooling flow model as well to a search for heating mechanisms.

Around the same time strong evidence of interaction between the central AGN and the surrounding ICM started to appear in the cases of Hydra A (David et al., 2001) and the Centaurus cluster (Fabian et al., 2005). Soon the best candidate for the quenching of the cooling flow became the AGN feedback in the form of X-ray cavities and shocks. In this scenario, cool gas from the ICM falls towards the central AGN, which in turn is activated or has its activity enhanced, with a renewed relativistic jet emission the AGN deposits its energy in the surrounding ICM, heating and quenching the cooling-flow, which completes the feedback cycle. Although nowadays it is generally accepted that AGN feedback is central to balance out radiative cooling in cool cores, exactly how the AGN deposits its energy in the ICM is still a very active area of research (Li et al., 2017).

2.3.2 Differences between cool-core and non-cool-core clusters

When exploring different definitions of cool-cores (CCs) and non-cool-core clusters (NCCs), Hudson et al. (2010) shows that the dichotomy between CCs and NCCs is not so simple as the presence or absence of a central temperature drop might suggest, with a distinct intermediate class being present. They employ three classifications: strong cool-cores (SCCs) are defined as having very short central cooling times ($< 1 h_{71}^{-1/2}$ Gyr), low central entropy, systematical central temperature drops (with $T_0/T_{vir} \approx 0.4$) and the BCG

⁴ cD galaxies are giant elliptical galaxies, with an extended stellar envelope, found almost always in the bottom of the gravitational potential of clusters.

in close proximity to the X-ray peak; non-cool-cores (NCCs) have long central cooling times ($> 7.7 h_{71}^{-1/2}$ Gyr), are characterized by large central entropies and a flat temperature profile or that rises towards the center. Moreover, they identified an intermediate or transitional class named weak cool-cores (WCCs).

To further shed light on the nature and diversity of these distinct classes of clusters, several authors employed numerical simulations to try to recreate and make predictions concerning the observed population of clusters at $z \approx 0$. These works suggest that there are very important evolutionary differences between CCs and NCCs. It has been established that CCs have in general less violent merger histories, accreting halos more slowly via hierarchical mergers. When an eventual major merger occurred in the life of these systems, the cool-core survived. In contrast, NCCs generally suffer violent major mergers early on that destroys proto-cool-cores and create conditions that prevent the cooling of the central regions (Henning et al., 2009; Burns et al., 2008). The more violent and merger rich evolutionary life of NCCs produce a greater mass range in these systems, generating more massive systems with ease compared to CCs. From the cluster sample simulated in Burns et al. (2008), the mean mass of the 10 most massive CCs at $z = 0$ is $2.4 \pm 1.4 \times 10^{14} M_{\odot}$, while the mean mass of the 10 most massive NCCs is $11.3 \pm 4.0 \times 10^{14} M_{\odot}$.

2.3.3 Galaxy interactions with the ICM

Galaxies are embedded in the ICM, and therefore several feedback mechanisms occur that affect galaxy evolution. This interplay between galaxy and the ICM, and between galaxy themselves in this crowded environment, is responsible to the demographics of galaxy morphology and color observed in clusters. One important interaction is ram-pressure stripping (with an extreme case shown in fig. 2.3). In this process, a galaxy that is traveling through the ICM loses part of its gas content due to hydrodynamic interactions with the hot gas, which is proportional to the relative velocity and local density.

This, together with galactic winds and AGN feedback, are the major mechanisms of taking the metal rich interstellar medium away from its original galaxy and enriching the ICM.

Another consequence of the galaxy-cluster interaction is the ubiquitous red-sequence of early-type galaxies. First unequivocally detected in in the 70s (Faber, 1973; Visvanathan and Sandage, 1977), it is a linear relation present in the color-magnitude diagram (CMD)

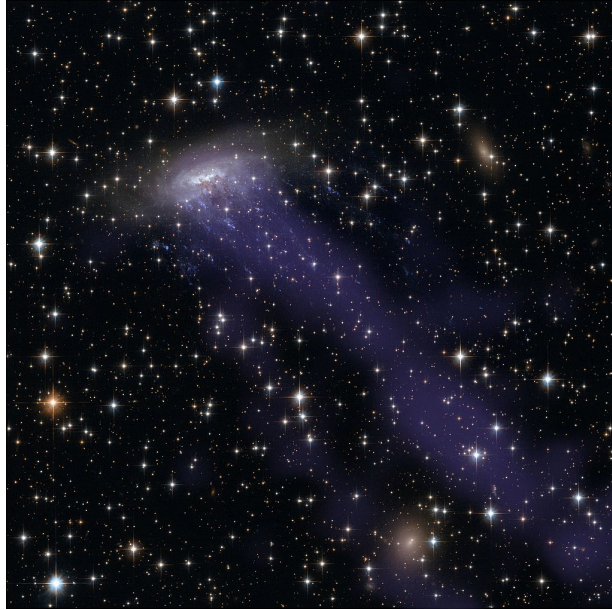


Figure 2.3: ESO 137-001 is a famous example of the so called jellyfish galaxies, where a strong ram pressure stripping is present. Credit: NASA, ESA, CXC

of the cluster galaxies. Figure 2.4 shows the red-sequence of the cluster ZwCl1215 fitted by a simple linear regression.

Several works suggest that the red-sequence slope has its origin in a metallicity-luminosity relation of the early-types (Ferreras et al., 1999; Terlevich et al., 1999). It is long known that age and metallicity have an influence in the colours of early-type galaxies, making their spectral energy distribution (SED) redder. Thus the red-sequence is formed because the most massive (and luminous) galaxies have a deeper potential well, which retains more efficiently the supernova ejecta from its stars, which in turn is reprocessed back into new stars, contributing to a redder population.

Due to its ubiquity and ease to detect, the red-sequence has been widely used to identify galaxy clusters in optical surveys (Gladders and Yee, 2000). They use the red-sequence as a direct indicator of overdensity. Some remarkable results were obtained, being able to detect small groups with velocity dispersions as low as $\sim 300 \text{ km s}^{-1}$ and a redshift accuracy of 10%.

Another direct evidence of galaxy evolution inside clusters is the Butcher–Oemler effect (Butcher and Oemler, 1984). It consists of the observation that the fraction of blue galaxies increase with redshift, which is a photometric footprint of morphological evolution, more specifically a transition from late to early-types, which happens with more intensity in the

cores of rich clusters.

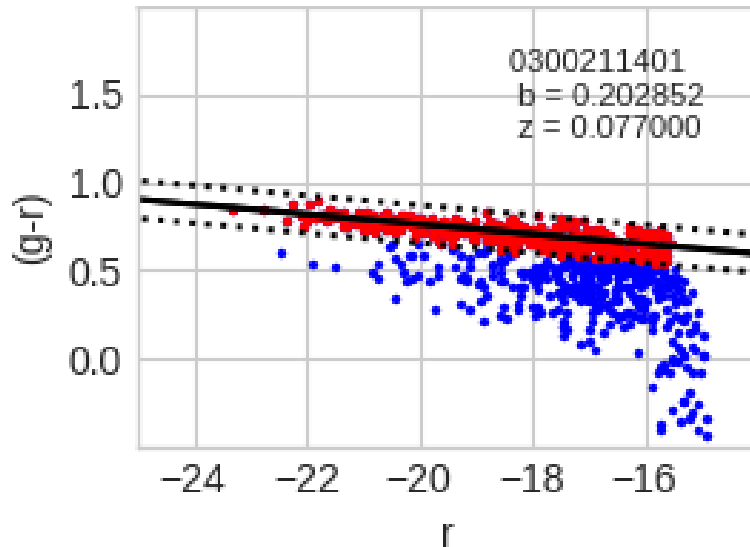


Figure 2.4: Red-sequence of ZwCl1215, fitted by a simple linear regression. The linear coefficient is b , the angular coefficient is fixed at -0.028 and z is the redshift. In red are galaxies within $1\text{-}\sigma$ (standard deviation) distance from the linear fit.

It is still not clear how the different environments, such as in CC and in NCC clusters, may affect the evolution of the galaxy population. As explained in section 2.3.2, CCs and NCCs have on average very different merger histories, which in turn might be reflected on galaxy properties, such as color, star formation and morphology. One of the objectives of this work is to investigate if this dichotomy (CCs and NCCs) is reflected in the galactic population.

XMM-*Newton*: Instruments and Particle Background

There are a few peculiarities of X-ray astronomy that, although not exclusive to this waveband, contribute significantly to the complexity of the spectral and image analysis. They are:

- The low photon counts.
- The fact that it is made exclusively by the use of satellites, due to the opacity of the atmosphere. (On the earlier days balloons and ballistic rockets were also used.)

Regarding the first one, high-energy astrophysics has this idiosyncrasy, which leads to some say that the field is “photon hungry”. This is a problem, due to poor photon statistics, but also offers some advantages. Given the high energy of each X-ray photon, the flux is limited to a few counts per second, and therefore we have a situation where we can detect each photon individually and record its energy, which offers some spatial spectral information (although with limited resolution, when compared to gratings). This is a tremendous advantage, that may give insights specially to the study of extended sources (as galaxy clusters).

The other particular feature, regarding the exclusiveness of exospheric observations, leaves the detectors exposed to a plethora of particle backgrounds, both of local and cosmic origin, that may vary with time, with pointing direction, and also with orbital position of the satellite. In this work, the X-ray data we use were acquired by the XMM-*Newton* space telescope.

Before we dwell on the problems of data reduction and spectral analysis in chapter 4, it is useful to have a grasp of some of the XMM-*Newton* characteristics and functionalities that, being exclusive or not, defines it as an X-ray observatory. These are important to

not only assist us in having an accurate interpretation of the data processing pipelines, but also help when dealing with the unavoidable problems and limitations of X-ray astronomy in general, or of the instrumentation in particular.

3.1 The XMM-Newton Observatory

The X-ray Multi-Mirror satellite, also named after Sir Isaac Newton, was launched from Kourou, French Guiana, on 10 December 1999 aboard an Ariane 5 rocket. Part of the ESA Horizon 2000 program, it is stationed in a highly eccentric orbit with a 48h period (Jansen et al., 2001).

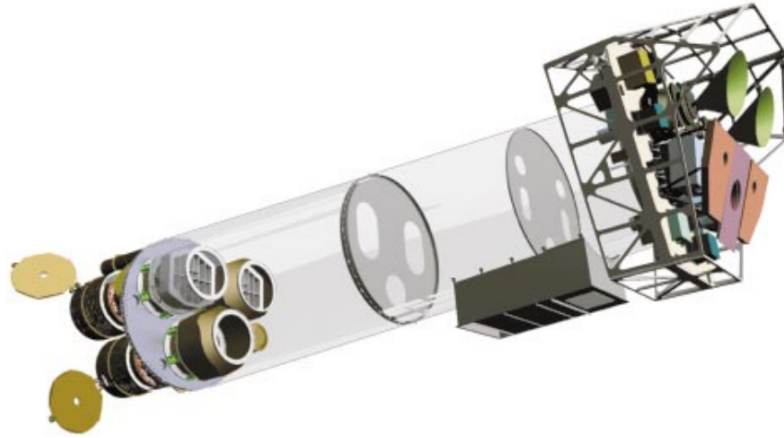


Figure 3.1: Schematics of the XMM-Newton observatory. To the left lies the three Wolf Type I mirrors in the open position, while at the right, on the Focal Plane Assembly, resides the three cameras, the two Reflection Grating Spectrometer (RGS) and other instruments. (Turner et al., 2001)

It consists of three telescopes, each with 58 Wolf type I mirrors nested in a coaxial and co-focal configuration, of focal length 7.5 m and a geometric effective area of 1500 cm² (Aschenbach et al., 2000). At the focal plane lies the EPIC imaging instruments (European Photon Imaging Camera) each with a 30 arcmin field of view (FoV). Two of these telescopes have gratings in the optical path that deflects around 50% of the flux towards two arrays of CCDs. These Reflection Grating Spectrometers (RGS) offers a resolving power from $E/\Delta E \approx 150$ to 800 at the 0.33–2.5 keV range (den Herder et al., 2001).

3.2 European Photon Imaging Camera

The three EPIC instruments in the telescope's focal plane offers imaging and spectral capabilities at 0.2 – 10 keV. The two cameras with gratings in the optical path are comprised by seven MOS (metal–oxide–semiconductor) CCDs each (Fig 3.2), while the third unobstructed beam have at the focal plane 12 CCDs divided in 4 quadrants that use p-n junctions technology (Turner et al., 2001).

The front part of each camera holds a filter wheel door, calibration source and radiation shielding. The filter wheel can operate in three modes (thin, medium and thick) or completely closed, when no photon reaches the CCDs. The closed position is important for calibration purposes and plays a crucial role in determining the high energy particle background.

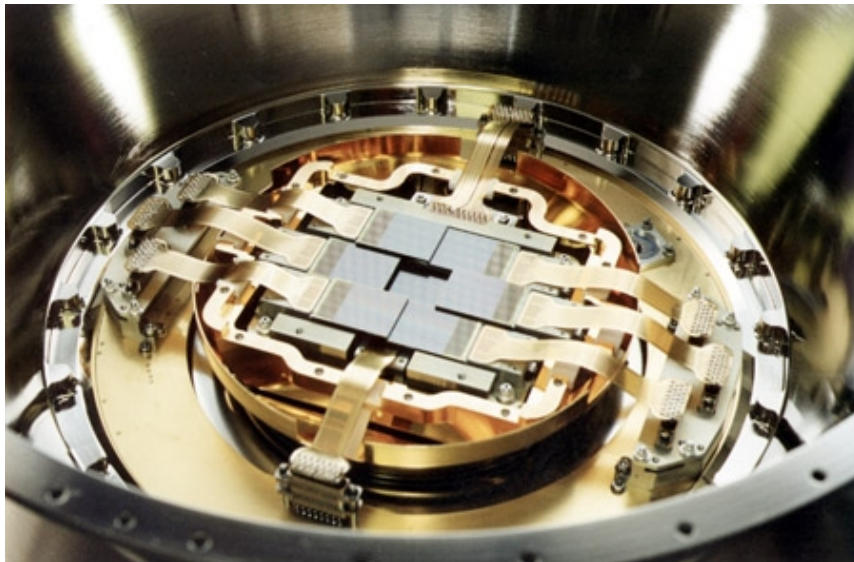


Figure 3.2: One of the MOS cameras inside a cryostat. (Turner et al., 2001)

EPIC also includes the Radiation Monitor System, that registers the ambient proton and electron flux. Besides the scientific value obtained from recording the local particle environment, it also works as a safety mechanism that warns when the particle flux surpasses a threshold that is potentially dangerous to the CCDs or other components.

3.2.1 Charge-Coupled Devices

Developed in 1969 at the famous Bell Laboratories, CCDs were first used in X-ray astronomy in 1987, aboard a sub-orbital rocket, to observe the supernova SN 1987A. The

first satellite with an X-ray CCD camera came shortly after in 1993, with Japan's ASCA. Since then it became an ubiquitous tool that revolutionized the field.

CCDs are basically arrays of capacitors organized in pixels, each one coupled with the next along series of rows, which allows charge transfer between neighbours. After a photon interaction, a electron-hole pair is created and stored, and at the end of the frame time (exposure time before readout), this charge is transported pixel to pixel towards the readout amplifier.

Figure 3.3 shows the schematics of the CCD geometry on the MOS1 and pn detectors, with MOS2 being identical to MOS1, only with a 90° rotation. Also shown is the 30 arcmin diameter FOV. All CCDs operate in photon counting mode, with a high read-out frequency, producing event-lists. They are constantly calibrated by an on board radio-active source. Only the pn-camera receives 100% of the flux, since 50% of the flux is diverged to the RGS before reaching the MOS detectors, as mentioned above. One important feature that marks the uniqueness of the pn detector is that its CCDs are back-illuminated (Fig. 3.4), this means that particles have to travel $290\mu m$ of silicon before damaging the transfer channel and decreasing charge transfer efficiency. In this sense, for low energy protons the pn-CCDs are “self-shielding” compared to MOS (Strüder et al., 2001).

As opposed to optical applications, where an individual photon is barely detected and therefore long frame times are needed to accumulate thousands of photons and consequently charge, in X-ray astronomy the high energy of each photon, and its aforementioned scarcity, makes it possible to measure the energy of each one individually. This, together with the location of the detection (pixel position), offers the unique advantage of having spatial spectral information.

This convenience comes not without its drawbacks. If more than one photon is absorbed by the same pixel, or by neighbouring ones, before readout, they will be identified as a single photon with double (or more) energy, a problem that is referred to as pile up. In a related scenario, photons might be detected during the readout phase, when it assumed that all the charges stored were in place before readout. This will cause the event to have a wrong time and position assigned to it. These are called out-of-time events, and are particularly problematic to the pn camera.

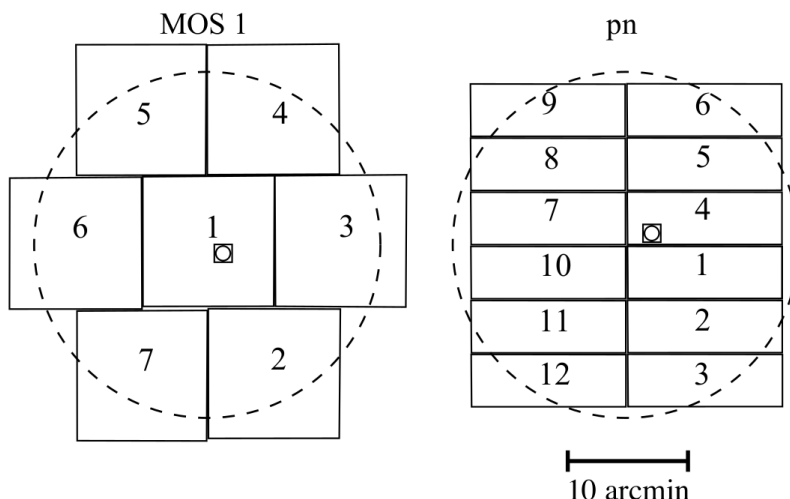


Figure 3.3: MOS1 and pn CCD geometry, with the FOV superimposed as a dashed circle, to scale. The telescope optics only focus X-rays (and, unfortunately, soft protons) inside the dashed circle. The CCD regions exterior to it are called *unexposed corners*, that, despite its name, are exposed to the high energy particle background and fluorescent emission from the inside of the telescope. Image based on XMM-Newton Users Handbook.

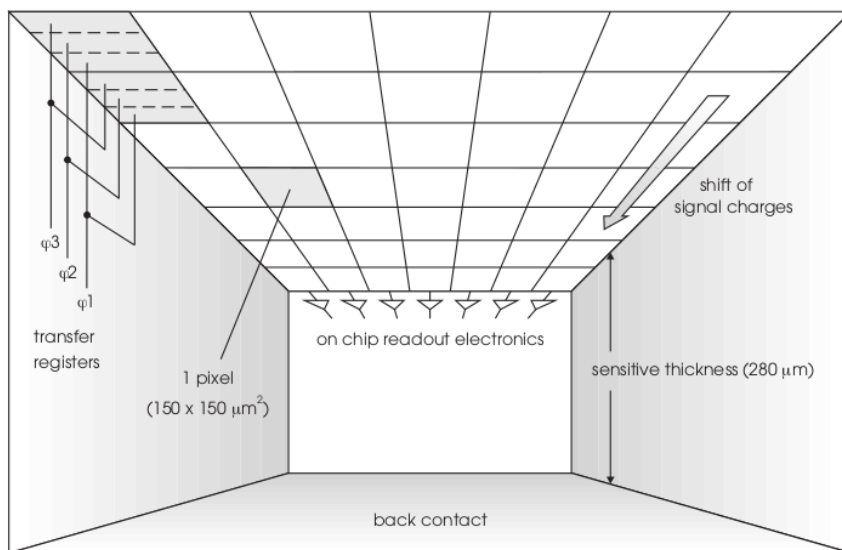


Figure 3.4: Interior of a pn-CCD. In the image, the photons enter from the bottom side, marked “back contact”, and deposit its energy $10\mu\text{m}$ from the surface containing the pixel structure. Figure from Strüder et al. (2001).

3.2.2 Micrometeoroid damage and pixel defects in EPIC

Another problem faced by space observatories is that not only photons and subatomic particles reach the detectors. Micron-sized particles might travel along the optical path and eventually damage the CCDs at the focal plane. The resultant damage vary greatly,

from simple pixel defects to entire CCDs being completely unusable. In the case of XMM-Newton, the MOS1 camera served as a cosmic bulls-eye to not one, but two sizeable micrometeoroid hits that completely disabled CCDs #3 and #6. A collateral damage was also suffered by CCD #4 after CCD #3 was lost, causing an excess signal to lower energy events towards the border (Fig. 3.5).

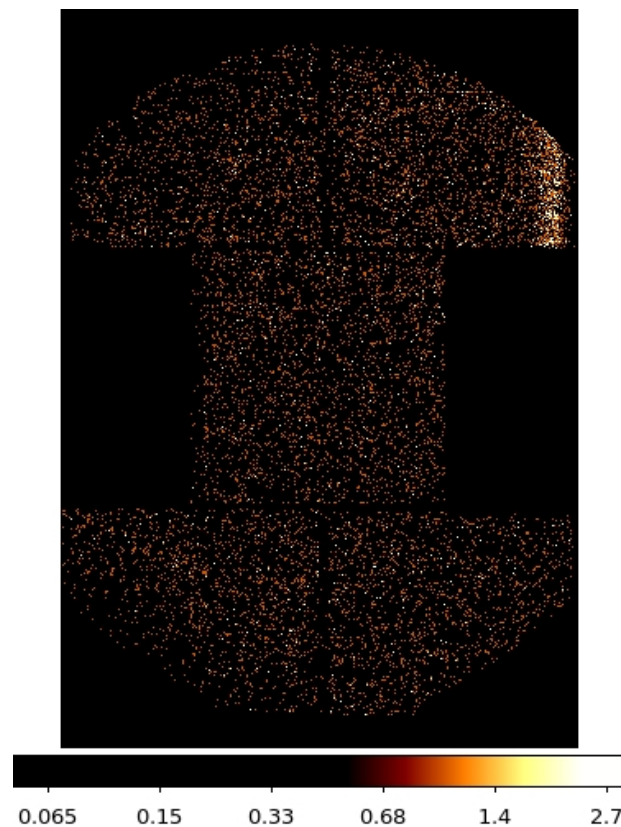


Figure 3.5: Raw count image of MOS1 after the meteoroid hit in revolution 2382. Note the collateral damage to CCD #4 causing an enhanced signal. Source: <https://www.cosmos.esa.int/web/xmm-newton/mos1-ccd3-impact>

In the less catastrophic scenario, single pixels (or entire rows) might stop working due to age, manufacture defects or even radiation damage. Furthermore, some anomalies might occur with excessive dark currents in pixels, that might be completely ignored on board to avoid wasting telemetry, or are flagged and eventually dismissed during data analysis.

3.2.3 Pulse-height amplitude conversion to energy or wavelength

After an X-ray photon interacts with a pixel on a CCD, a charge is stored. For historical reasons this amount of charge is referred to as PHA (pulse-height amplitude). The

conversion from PHA to “true” photon energy is not linear and varies with position, time and energy. The final photon energy recorded then must take into account: the probability of a photon of given energy generating the given PHA (energy resolution), quantum efficiency, position dependency (vignetting), filter transmission and pixel/CCD current status. These information are collected in the *Response Matrix* (RSP), that is in itself the product of two other matrices: the *Ancillary Response*, that describes how the effective area varies on the detector, and the *Redistribution Matrix*, which maps from energy space into PHA space (or position).

With all the energy information in hands, we can therefore start spectral analysis. Moreover, the RSP is also important for image analysis, more specifically for the creation of *Exposure Maps*, the X-ray analogue of flat fields in the optical regime. These not only include vignetting, but also CCDs gaps, dead pixels and dead rows.

3.3 The particle induced background of XMM-Newton observations

For an accurate spectral analysis, it is fundamental to determine precisely the background emission which is detected together with the source of interest. For point-sources, the analysis may be hugely simplified by measuring the background in a annulus around the source. For extended sources this method cannot be used because of the strong variation of the CCD gain and, sometimes, the extended source may cover all the field-of-view. Therefore, a rigorous analysis of the background is needed.

It is useful to differentiate between two different kinds of background: cosmic and instrumental. The first is composed of photons that originate from astrophysical sources, while the latter is from particles that are either directly detected by the CCDs, or indirectly when they hit other components of the telescope and generate fluorescent emission. The instrumental background is composed of:

- Quiescent particle background (QPB): probably associated with galactic cosmic rays (GCR), it comprises high energy particles that interact directly with the detector’s CCDs. They are only considered constant throughout the duration of typical observations, since, as we shall see, it varies both in longer time scales and in sky position.
- Flares: comprised mostly of low energy (soft) protons ($E \sim 100$ keV) of likely solar

origin, or originating in the upper atmosphere, it varies in shorter timescales than the QPB. It also changes with spacecraft location in orbit.

- Fluorescent lines (also called FX, from Fluorescent X-rays): they originate when energetic particles interact with electronic components within the camera interior, and excite the atoms which end up emitting X-ray photons. Therefore it is no surprise that we detect lines corresponding to commonly used elements in the spacecraft (Si, Cu, Au and Al to name a few).

Some background components are exclusive to the XMM-Newton and Chandra observatories, as for example, the fact that the telescope optics focuses soft protons (consequence of the Wolf type configuration). On the other hand, telescopes like the older ROSAT and the more modern Suzaku, that are stationed in low earth orbit, experience other kinds of backgrounds that are more prevalent closer to Earth, such as exospheric emission of X-rays (Kuntz et al., 2007).

The instrumental background, as the name implies, is highly dependent on camera configuration, satellite position and attitude, and also on aspects of the telescope environment, such as solar activity. Therefore this is a suitable moment to address these components in more detail. The cosmic background component on the other hand, that includes X-ray emission from the solar neighbourhood and the galactic halo, will be addressed in section 4.2.

3.3.1 Quiescent Particle Background (QPB)

It is the dominant component above 2 keV, and also referred to as unfocused particle background, since as opposite to the soft protons, it is not focused by the telescope's optics. Although called "quiescent", it is only so during a single observation because it is time variant on longer time scales as shown in Fig 3.6. This particle background not only have an inherent variability, but it is also anti-correlated with the 11 years solar cycle and, furthermore, depends on the individual CCD's responses, since they also evolve during the telescope's life time.

To further add to the problem, the detector's particle response vary with the position on the detector itself and also with the energy band. In Fig. 3.7 we see MOS1 and MOS2 images produced with the filter wheel in the closed position (FWC), which is a 1 mm thick

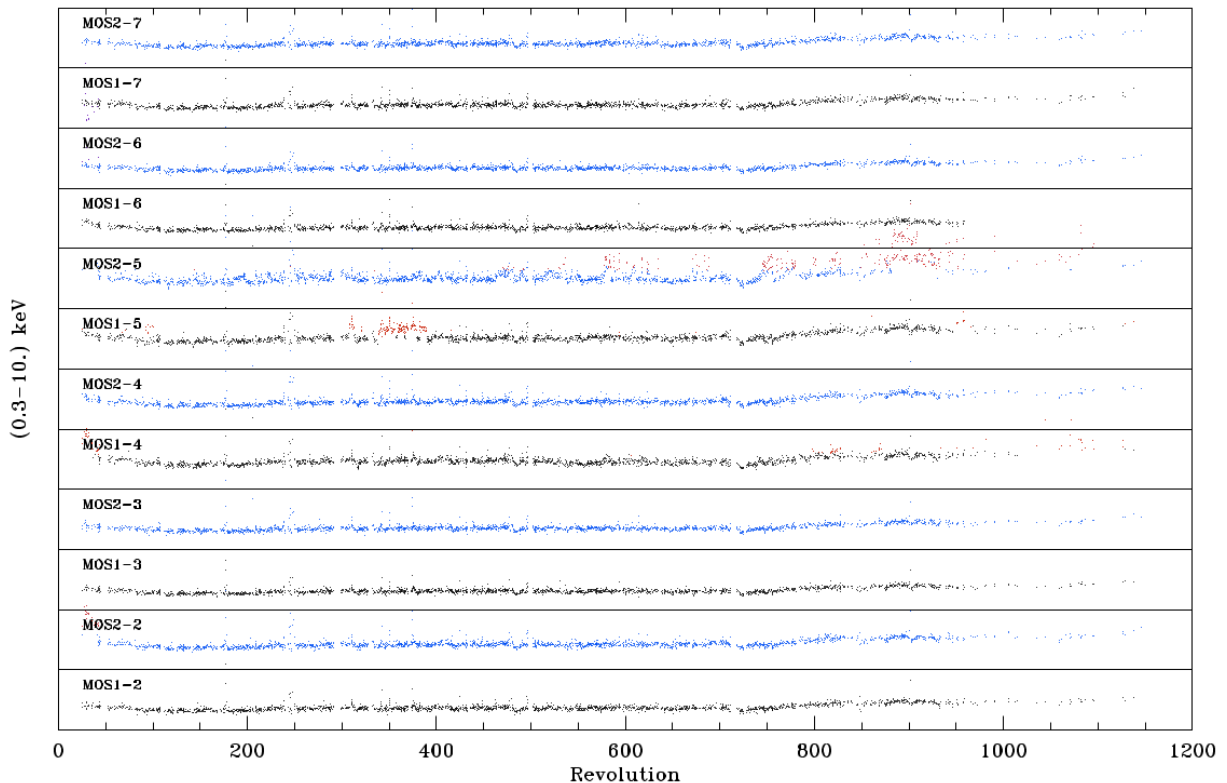


Figure 3.6: MOS1 (black) and MOS2 (blue) count rates from the unexposed corners of the detectors, from each CCD, in the 0.3 – 10.0 keV band. Anomalous periods are in red. A revolution corresponds roughly to 48h. These counts are roughly due to the QPB (Snowden et al., 2008)

aluminum lid that prevents any X-ray photons and soft protons to reach the CCDs, while allowing the detection of high energy particles.

Regarding the physical origin of the QPB, the independence on the magnetospheric environment (satellite altitude), the high energy of the particles (reaching a few MeV) and the anti-correlation with the solar cycle makes galactic cosmic rays (GCRs) the most likely candidate (Gastaldello et al., 2017).

3.3.2 Soft Protons (Flares)

An unfortunate surprise noted after the launch of the XMM-Newton and Chandra observatories was the fact that low energy protons (less than a few 100 keV) were focused by the telescope’s mirrors and detected as a photon count (Snowden et al., 2008; Arnaud et al., 2011). These particles, with a likely solar or atmospheric origin, are circulating in the Van Allen belt and are detected as flares, i.e. their signal vary in very short time scales compared to a observation time frame. This high variability is due to not only the uneven

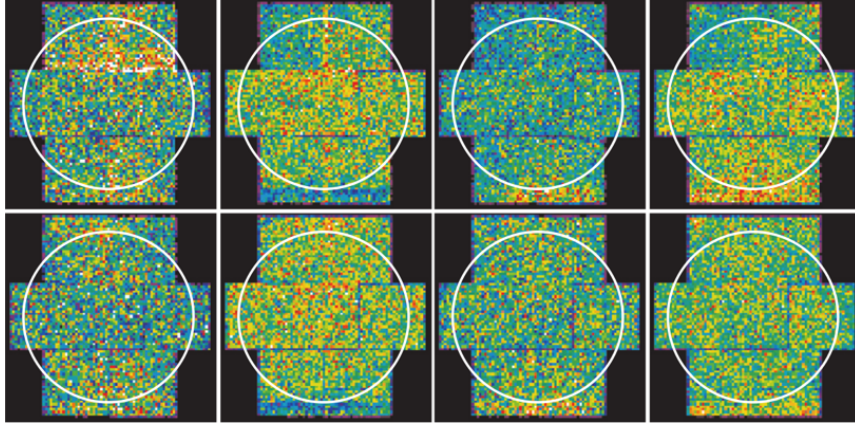


Figure 3.7: Filter wheel closed (FWC) observations with the MOS1 (upper) and MOS2 (lower) cameras. From left to right, each image corresponds to the bands: 0.35 – 1.25, 1.25 – 2.0, 2.0 – 4.0 and 4.0 – 8.0 keV respectively. The white circle represents the limit of the FoV, outside of which are what we refer to ”corners”, the regions that are always shielded from cosmic photons. The 1.25 – 2.0 keV band is mostly contaminated by FX radiation. (Snowden et al., 2008)

distribution of particle density throughout the region, but also due to the elliptical orbit of the satellite, which makes the instruments embedded in very distinct environments, in different altitudes (Ghizzardi et al., 2017).

Unfortunately these flaring events are random and cannot be subtracted directly, which makes the affected time intervals unusable, and therefore they are excluded from the analysis by filtering the light curve (see fig. 4.1). Some observations are so much afflicted by these particles that they are deemed unusable.

3.3.3 Fluorescent Lines

Another instrumental background component that, although also originating from energetic particles, is detected as emission lines in the spectra. High energy particles traveling through the telescope have the probability of, besides interacting directly with the CCDs, being absorbed by atoms that comprises the diverse instrumentation aboard (see figure 3.2 for a close-up of a MOS CCD array). These atoms are excited and eventually emits X-ray photons. Therefore several lines originating from elements used commonly in electronic components are detected as background (for example: Si, Au, Cu and Al. Fig. 3.8).

To complicate the matter even further, since these different elements are not symmetrically distributed around the CCDs, the fluorescent emission will affect different regions of the CCDs with varying intensity, depending on energy band and also on the overall

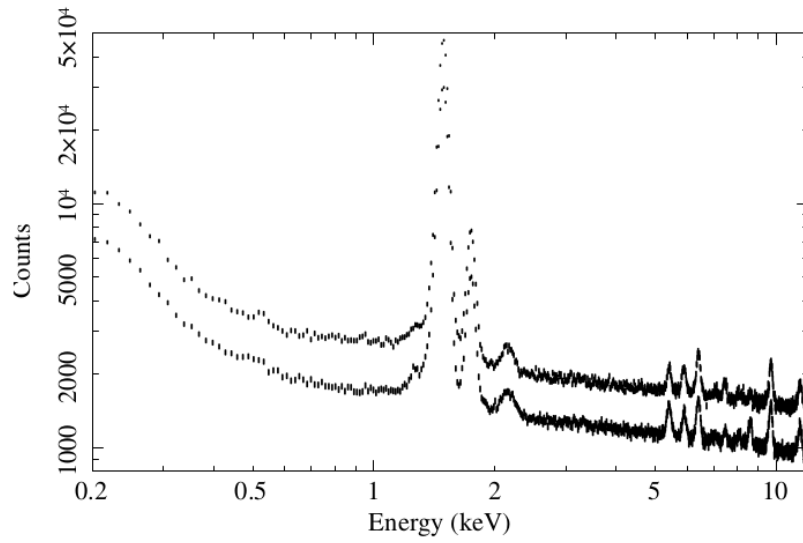


Figure 3.8: MOS1 and MOS2 spectra obtained with the filter-wheel closed. Note the prominent Al-K α and Si-K α emission lines at 1.5 keV and 1.7 keV respectively (Snowden et al., 2008). The MOS2 data have been scaled by a factor of 1.5 in order to separate the spectra for clarity.

instrument configuration, such as filter wheel positions (see figure 3.7).

X-ray Data Reduction

The procedure for XMM-*Newton* data reduction and preparation for analysis is not simple. The ESAS (Extended Source Analysis Software) method takes a “first principles approach” for the extraction of the X-ray background, not using for example blank-sky images (images constructed by superposing many exposures, without noticeable sources). The modeling of the Quiescent Particle Background (QPB) relies on filter-wheel-closed data, dat from unexposed corners of the detectors and from ROSAT All-sky Survey data, with the model particle background spectrum directly subtracted. All the other background components (such as extragalactic and galactic backgrounds) are treated individually and added explicitly to the model used for spectral fitting.

Although some tasks are performed by simple repetition of commands, other processes involve careful thinking and planning, specially when dealing with the model parameters during the spectral fitting. In this section it will be outlined the problems faced during the implementation, and how some of these issues were circumvented. Focus will be given to the spectral fitting process and how the X-ray background is modeled, which is a critical aspect for X-ray data analysis.

4.1 Methodology of the X-ray Data Reduction

4.1.1 Calibration files and clean event files

To perform analysis of XMM-*Newton* data it is necessary to have the current calibration files (CCF). Since these files contain information regarding the telescope status and inboard calibration specifics, they must be continuously updated. To do so it is recommended to sync the user directory to the mission repository. Besides the basic CCFs, the

ESAS package also demands extra calibration files. These include filter wheel closed data, unexposed corner data, as well calibration data used in the QPB and SP modelling.

With the calibration files in place, the task *cifbuild* will gather all the pertinent files in the observation directory. The next step is to create clean event files, which means filter the observation for flares. This is accomplished by the tasks *pn-filter* and *mos-filter* with the light-curve cleaning. These tasks generates light curves and high energy count rate histograms from the FoV (figure 4.1). Normally a typical observation will have a gaussian distribution around a given mean in the count rate histogram, with an eventual tail from higher count rate intervals. The algorithm will fit a gaussian function to this distribution and determine 1.5 sigma intervals around the mean. This will be the cut out threshold: time intervals with higher count rates will be discarded as flaring. We note that even though the time intervals considered free of flares might appear somewhat flat in the light curve, it is always assumed that a residual SP contamination is present. This residual SP component is modeled in the spectral fitting process. The final product are the so called clean event files.

The task *mos-filter* also outputs important information regarding CCDs operating in anomalous states. This occurs when there is a artificial enhancement of the background with energies $E < 1$ keV. These CCDs must be excluded from the analysis.

4.1.2 Cheese and the masking of point-sources

Since we are interested in the ICM emission, point-sources must be excised. These are normally Active Galactic Nuclei or foreground stars. The task *cheese* is responsible for detecting point-sources and creating masks that are later used when extracting spectra or generating images (Fig. 4.2). The task accepts three input values: a scale that determines the fraction of the PSF of the source that is subtracted; a rate that is a threshold of the source flux, below which it is not considered to be a source and therefore it is ignored; and a minimum distance between sources, that essentially prevents the task from masking extended regions such as the cluster core. Eventually the routine will miss some obvious sources, specially if it is located near the gaps between CCDs or at the edges of the detector. Unfortunately there's no obvious solution to this issues besides visual inspection and eventually running the task again with different parameters, until a satisfactory source masking is achieved. Therefore user visual inspection is encouraged. The task also masks

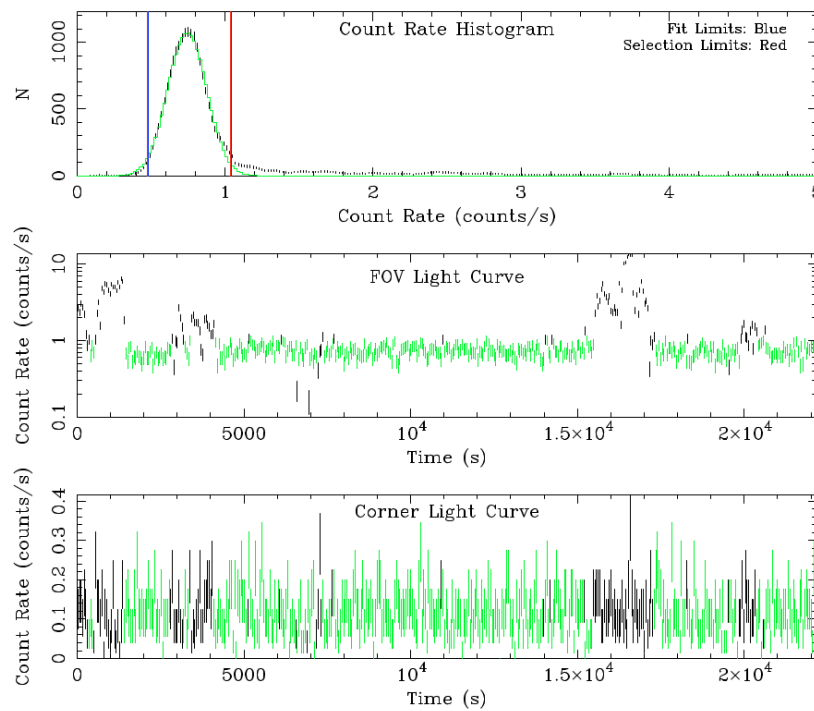


Figure 4.1: Count rate histogram, FoV light curve, and unexposed corner light curve of a typical observation of a galaxy cluster made by XMM-Newton. Note the flaring intervals, with unusually high count rates in black.

CCD defects and gaps, and take into consideration inactive CCDs such as the case with MOS1 CCDs #6 and #3 that were lost due to micro-meteorite impacts.

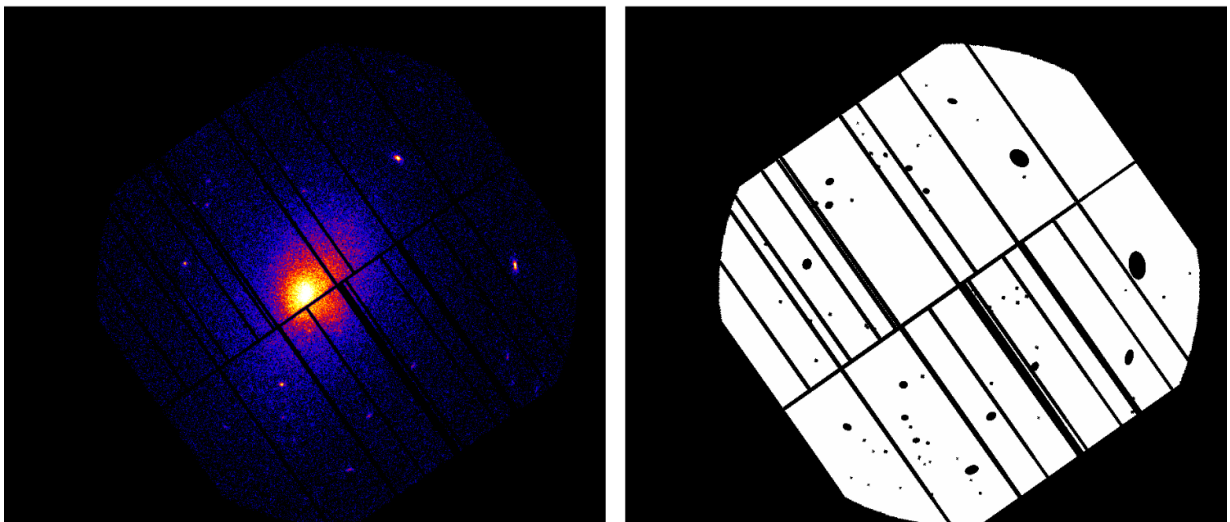


Figure 4.2: “Cheese mask” generated for an observation of Abell 2065, for the PN camera. Note that dead pixels, dead rows and CCD gaps were also masked.

4.1.3 X-ray peak detection and annuli determination

To obtain radial profiles of cluster properties, concentric annuli must be determined from which the spectra are extracted (Fig. 4.3). Therefore it's advantageous to have a pipeline capable of automatically finding the peak of the X-ray emission, and that proceeds to determine the annuli radius given a user defined number of counts. This care must be taken to avoid getting an annulus with too little cluster emission, which would be a problem when fitting the spectrum (the error bars of the model parameters improve with a higher signal-to-noise). To find the X-ray peak we use the task *dmstat* from the CIAO package. CIAO (Chandra Interactive Analysis of Observations) is the software for data analysis of the Chandra observatory. The reason to use a task from CIAO is the absence of a similar routine in the ESAS/SAS software. The task *dmstat* provides several statistics from an input image or region, such as the centroid of the image. By successively calculating the centroid of smaller regions, after a generous initial guess that covers almost the full FoV, the task quickly converges to find the centroid of the image, which coincides with the peak of the X-ray emission.

With the coordinates of the emission peak at hand, next we proceed to establish the radius of the concentric annuli. First, the background is estimated using an annulus large enough that has little to no cluster emission, and on each iteration the background contribution is subtracted to obtain a gross estimate of counts that originate from the cluster ICM alone. Given a initial input with the minimum desired number of counts per region, a loop calculates the amount of counts inside regions with successively larger radii, until the number of counts surpasses the minimum, after which the script proceeds to find the next annulus. The process continues until it reaches some suitable maximum radius or exceeds some number of iterations. Finally, after obtaining the centroid of the image and the radius of the annuli in image coordinates, these must be converted to detector coordinates and printed in text files that are later used for the spectra extraction.

4.1.4 Modelling and subtracting the Quiescent Particle Background

The QPB can be accurately modelled by filter wheel closed data together with data from the unexposed corners. These are present in the CalDB¹ files. But first, the tasks

¹ Calibration files available at: heasarc.gsfc.nasa.gov/FTP/xmm/data/ESAS/esas-caldb.tar

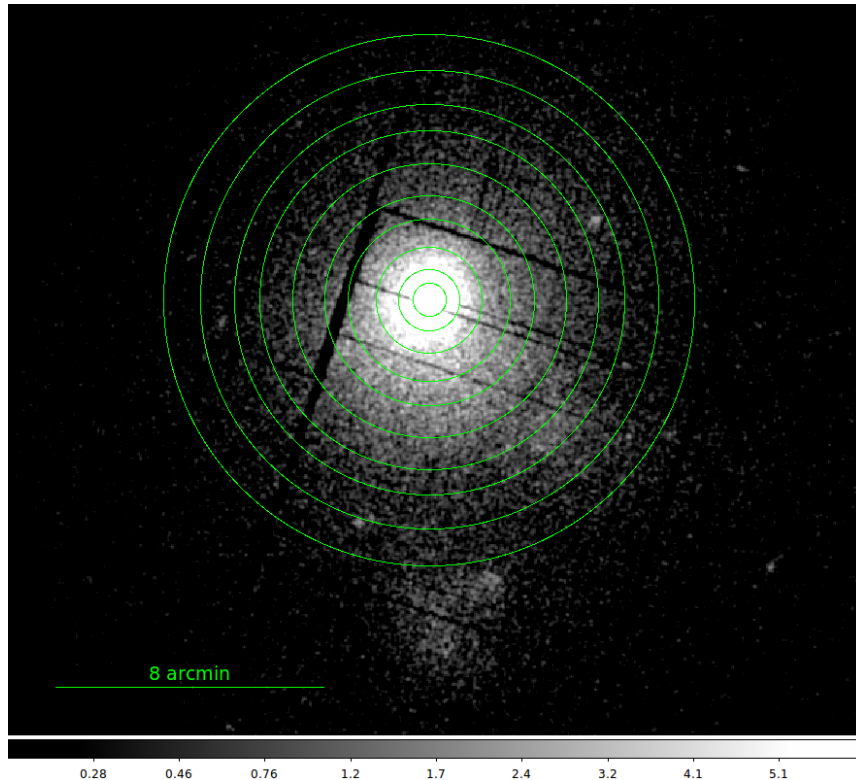


Figure 4.3: Annuli used for the spectral fitting of the cluster Abell 85.

mos-spectra and *pn-spectra* must be run to extract the total (contaminated) spectra from the regions of interest. Also ARFs and RMFs are generated, together with event images and exposure maps. To run these tasks, a “cheese mask” must be present, and also the descriptors of the annuli to be used.

The next step is to run the tasks *mos-back* and *pn-back* which model and generate QPB-subtracted spectra (figure 4.4). In general terms, the tasks searches the corner spectra of archival observations, to find the ones with a similar overall behaviour, and then combine the archival and current observation background spectra, for greater statistical significance. They are then scaled, bin by bin, and combined with FWC data. Finally the resulting model QPB spectra are subtracted from the FoV one (Snowden et al., 2008). This process is repeated for each annulus and each detector.

4.2 Spectral fitting

For the spectral analysis we employ the program *XSPEC* from NASA’s High Energy Astrophysics Science Archive Research Center (HEARSAC). It is an interactive spectral-

97820101 — MOS1S003

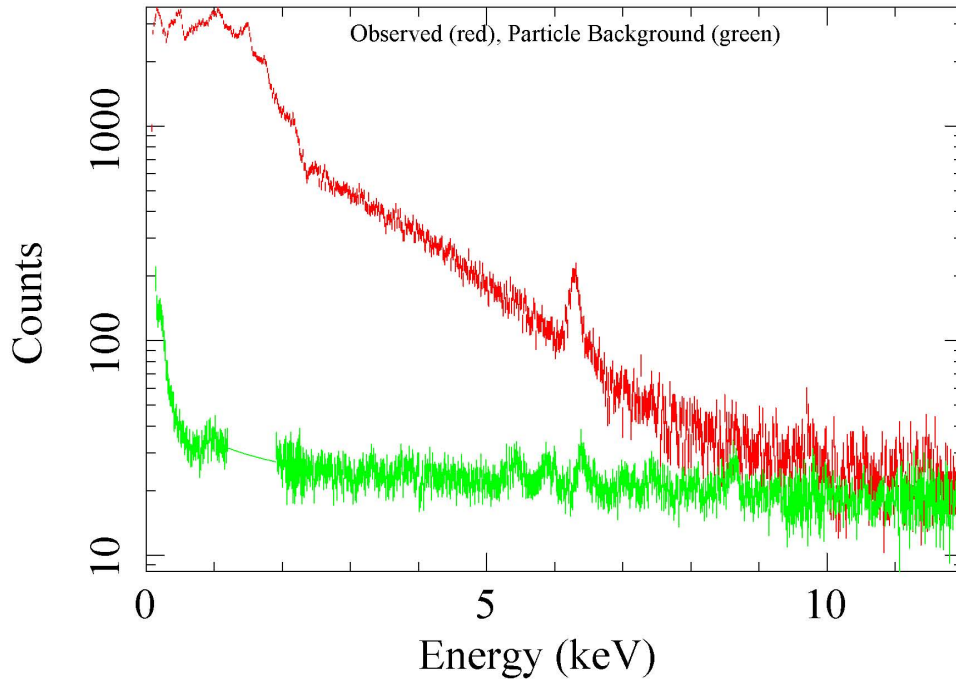


Figure 4.4: Observed spectrum (red) and QPB generated spectrum (green) for a observation of Abell 1795.

fitting program that is detector-independent, therefore it can be used with spectra from any spectrometer. After providing the response files and the total spectra, the user can choose from a list of theoretical models and combine them using simple arithmetic expressions, as shown below (equation 4.1). Also possible is the choice of different statistics to define the goodness-of-fit. For this work χ^2 was used.

Given that the quiescent particle background is subtracted beforehand, and the flare contamination is removed by the light curve screening, the remaining X-ray background must be modeled explicitly during the spectral fitting. This remaining background, called the Cosmic X-ray Background (CXB), is composed by galactic and extragalactic sources.

At higher energies ($E > 1$ keV) the extragalactic component dominates. It is mainly composed of unresolved emission from cosmological sources, mostly AGNs. It can be modeled as a power law with a index of 1.46. At lower energies there are several components

that are treated in the model as thermal emitters and have a galactic origin. Firstly, there's the emission of the Local Hot Bubble (LHB), an irregular shaped cavity in the inter-stellar medium of the solar neighbourhood, filled with hot plasma, of dimensions of up to 100 pc. Due to its proximity it's not absorbed by the galactic column. Secondly, there are two absorbed components that represents emission from the galactic halo, with a cooler $E \sim 0.1$ keV and a hotter component at $E \sim 0.25 - 0.7$ keV. The latter might also contain emission from the Local Group. The spectral model therefore takes the form (using the *XSPEC* notation):

$$\sum_{n=1}^8 \text{gaussians} + \text{con} * \text{con} * (\text{apec} + (\text{apec} + \text{apec} + \text{pow}) * \text{wabs} + \text{apec} * \text{wabs}), \quad (4.1)$$

where *apec* are emission models, *wabs* represent absorption (an absorbed thermal component is therefore *wabs.apec*), *pow* are power laws, *con* are constants while *gaussians* model emission lines. The first two gaussians model the MOS instrumental fluorescent lines, while the last six are lines from the pn instrument. Next, two constants are added to the model, one is the solid angle that the region comprises, the other is to take into account the relative normalization between the detectors (this two constants make it possible to link parameters between different regions and different instruments, since they are properly scaled). In sequence there are the background components: one unabsorbed component representing the LHB, two absorbed components taking the role of the halo emission (and possibly emission from the Local Group), and lastly the extragalactic power law. Finally, the last absorbed *apec* component representing the cluster emission. With 49 parameters for each spectrum and three spectra per annulus (MOS1, MOS2 and pn), the total number of parameters can reach 1470 for 10 annuli. Gladly, not all the parameters are free, and after all parameter freezes and links we can reduce this number to around 100 free parameters. The challenge of this part of the analysis is to generate scripts that, for any observation and any number of regions, automatically loads the spectra from each annulus, gives initial guesses for each parameter and fits the model to the data. Fortunately, with the exception of the cluster redshift and the equivalent hydrogen column in the line of sight, all the parameters from the instrumental lines and CXB components can either be frozen or linked, in a manner that is independent of the observation.

To help constraint the background parameters, spectra from the ROSAT all sky survey

(RASS) are used. We extract the spectra from an annulus with inner radius of 1° , and outer radius of 2° , centered in the cluster. This is assumed to represent well the background emission in the line of sight. We apply the same model (4.1) to these spectra, but with normalization of the cluster emission and all gaussian lines set to zero. Next it is necessary to link the background components with the ones in the XMM-Newton spectra.

4.3 Summary

In this section there is a brief summary of the steps for data reduction and analysis procedure, following the overall structure of the (significantly longer) scripts developed:

- Create a summary file `*SUM.SAS` from all Observation Data Files (ODF) using the command `odfingest`.
- Generate the appropriate calibration files for the observation with `cifbuild`.
- Create event files and clean the data for flares using `epchain` and `emchain` together with `pn-filter` and `mos-filter`.
- Determine which CCDs are operating in an anomalous state or if it is not working at all. CCDs #6 and #3 from the MOS1 detector were hit by micrometeoroids in 2005 and 2012 respectively, therefore if a observation is posterior to these events the CCDs must be explicitly excluded from the analysis.
- Detect and mask point sources using the task `cheese`.
- Determine the proper center and radius of the annuli to be used in the spectra extraction and fitting processes and create `.txt` files for each region and each detector, with the annulus coordinates using a pre-defined format.
- Generate a quiescent particle background (QPB) spectrum for each detector and each region with the tasks `mos-back` and `pn-back`.
- Extract a QPB subtracted spectrum, together with its response files (ARF and RMF), for each region and each detector using `mos-spectra` and `pn-spectra`.
- With `grapha`, group the spectra and its response files from a single region in a grouped file to simplify the input in the fitting process.

-
- Run the task *proton-scale* to obtain the area in arcmin^2 of the regions and also the normalization for the soft proton events of a given instrument and region.
 - Download a ROSAT All Sky Survey (RASS) spectrum and response file from an annulus sufficiently big in the direction of the cluster to represent the X-ray background in that direction. This RASS spectrum is used to constraint the background during the fitting process.
 - Obtain the equivalent hydrogen column in the direction of the observation.
 - Initialize *XSPEC* and input all the necessary data and models for the fit.
 - Establish the correct initial values and linkages of the parameters (more than a thousand for a typical observation).
 - Fit the model and determine the goodness-of-fit by using χ^2 , repeating it if needed.
 - Plot temperature and metallicity profiles using the fitted parameters.
 - Finally generate an image combining all three detectors.

Galaxy selection using Kernel Density Estimators

In this chapter, we turn ourselves to the optical data analysis, since we will be exploring the photometric properties of galaxies with respect to the properties of the ICM. Our goal here is to select cluster members by subtracting foreground and background objects.

Given the incompleteness of spectroscopic data and poor photometric redshift errors from the SDSS, a statistical approach to the subtraction of foreground and background galaxies (hereby only referred to as background) is desirable. In this section we outline a novel method that uses Kernel Density Estimators (KDEs) to obtain two dimensional probability density functions (PDF) that represent the distribution of galaxies in the $(g - r) \times r$ color-magnitude diagram (CMD), and with these in hand we obtain a formula that estimates the PDF representing the “true” distribution, from which we can assign a probability of membership for each galaxy.

5.1 Motivation and the classical binning method

Historically, a straightforward way of removing background galaxies is choosing a region, where it is assumed no cluster/structure is present, to represent the background (hereafter we will call this region “*field*”), and use it to numerically subtract the weighted number count of galaxies from the contaminated cluster region (i.e., cluster plus background). This assumes that the field does not vary much from the cluster to the region where the field is estimated. In the works of Pimblet et al. (2002); Kodama and Bower (2001), among others, this subtraction is done by binning the CMD from both the *field* and contaminated cluster. We improve on their method by using Gaussian Kernel Density Estimators (KDE) to avoid binning issues. Firstly we present their method, which we will

call “classical”, to illustrate the motivation for the use of KDEs.

The main goal is to, for each galaxy in the (contaminated) cluster region, assign a probability of such galaxy being a contamination, $P^{\text{bin}}(F)$. The method consists of binning the color-magnitude diagram of both our cluster region and the field, using a sensible binning size, that will be discussed shortly. Then, for each region, we count the number of galaxies that lie on a given bin, and we define the probability of a cluster galaxy being a contamination by:

$$P^{\text{bin}}(F) = \text{norm} \cdot \frac{N_F^{\text{bin}}}{N_{CLcont}^{\text{bin}}}, \quad (5.1)$$

where N_F^{bin} and N_{CLcont}^{bin} represent the number of galaxies that lie in the field and (contaminated) cluster regions respectively, while norm is defined as:

$$\text{norm} = \frac{A_{CLcont}}{A_F}, \quad (5.2)$$

which is simply the ratio between the physical areas (sky coordinates) in question.

The inherent problem with this approach is that probability is assigned to *all galaxies* that reside in the bin, which obviously may cause issues when being too generous with the bin size. Another very common problem stems from the inevitable instances where the probability happens to be greater than one, i.e. in the given region the normalized number of galaxies in the field is greater than in the cluster, due to statistical fluctuations (or, worse, some systematic error). Different authors proposed countermeasures to this problem as show in Pimbblet et al. (2002) and briefly summarized in Fig. 5.1. Although still present, the use of KDEs circumvent this issue, since these “anomalous” galaxies are isolated, and therefore doesn’t change the overall PDF, while in the binning scenario, all the galaxies within a bin would have artificial probabilities that originate from re-binning attempts to obtain probabilities less than one, as seen Fig. 5.1.

The next step is to have Monte Carlo runs, where a series of populations of galaxies are generated, given the probability of them actually belonging to the cluster, $P^{\text{bin}}(CL)$, which evidently is just:

$$P^{\text{bin}}(CL) = 1 - P^{\text{bin}}(F). \quad (5.3)$$

	4	0.5	0.5	0.5	0.5		4	0.416	0.416	0.416	0.416	
	3	0.5	0.5	0.5	0.5		3	0.416	0.416	0.416	0.416	
	2	0.5	0.5	1.2	0.5		2	0.416	0.416	1.0	0.416	
	1	0.5	0.5	0.5	0.5		1	0.416	0.416	0.416	0.416	
		1	2	3	4			1	2	3	4	

	4	0.5	0.5	0.5	0.5		4	0.5	0.5	0.5	0.5	
	3	0.5	0.525	0.525	0.525		3	0.5	0.5	0.675	0.675	
	2	0.5	0.525	1.0	0.525		2	0.5	0.5	0.675	0.675	
	1	0.5	0.525	0.525	0.525		1	0.5	0.5	0.5	0.5	
		1	2	3	4			1	2	3	4	

Figure 5.1: Summary of ways of dealing with the problem when some probabilities are greater than one in the binning method. **Top left:** an isolated bin has assigned probability greater than one. **Top right:** first method where all the bins are normalized by the anomalous one. **Bottom left:** second method where the excess probability is distributed equally to all adjacent bins. **Bottom right:** adaptive bin method adopted in Pimblet et al. (2002), where the bin size is increased and the probability calculated again. We emphasize that our method doesn't suffer from these shortcomings due to the use of continuous PDFs obtained using KDEs.

5.2 Kernel density estimators

An approximation using kernel density estimators is a method of attempting to recover the underlying probability density function from a set of data points. Here is a brief summary in the one dimensional case.

Let (x_1, x_2, \dots, x_n) be a set of independent and identically distributed data points, sampled from a probability density function f . The density estimator \hat{f} , using a kernel function K_h and a bandwidth h , is defined as (Silverman, 1986):

$$\hat{f}(x) = \frac{1}{n} \sum_{i=1}^n K_h(x - x_i) = \frac{1}{nh} \sum_{i=1}^n K\left(\frac{x - x_i}{h}\right). \quad (5.4)$$

If K_h is chosen such that it satisfies the condition

$$\int_{-\infty}^{\infty} K_h(x) dx = 1, \quad (5.5)$$

then by construction \hat{f} is also normalized,

$$\int_{-\infty}^{\infty} \hat{f}(x) dx = 1. \quad (5.6)$$

The intuition behind this definition is rather simple: centered on each data point, we sum “bumps”, the form of which is given by the kernel function, while its width is given by the factor h . Evidently the final shape of our density estimator \hat{f} is very sensitive to the choice of the bandwidth, as illustrated in Fig. 5.2.

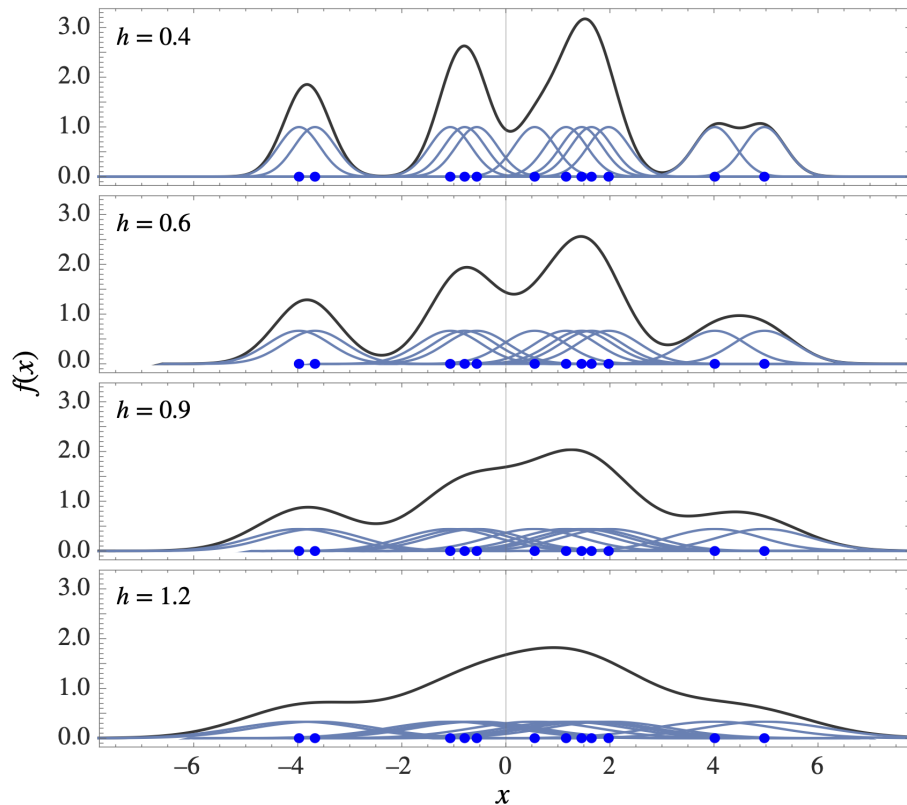


Figure 5.2: Example of how the bandwidth, h , affects the final kernel density estimation (black curves). A sample of 12 numbers are drawn from some probability density function. These data points are represented by small blue ovals on the x -axis, and a density estimation is applied using several bandwidth (light blue curves), from the narrowest (top panel) to a considerably larger one (bottom panel). Notice how sensitive the final shape of our density estimator is to the choice of the bandwidth. Figure based on Silverman (1986).

Unfortunately, there is no general guide that gives the right choice of bandwidth for a given data set. In this work it was deemed satisfactory the use of Scott’s rule (Scott, 2015):

$$h = n^{-\frac{1}{d+4}}, \quad (5.7)$$

here n is the sample size and d the dimension. While this section uses scalars ($d = 1$) to illustrate the concept, the method is applied to color-magnitude diagrams, in other words $d = 2$.

Moreover, since we wish to obtain a normalized probability density function, and we postulate that it should be smooth, derivable and tend to zero in infinity, then the normal distribution is an obvious choice for the Kernel function. Therefore the chosen tool to obtain our KDEs was the `gaussian_kde` class from SciPy¹.

5.2.1 Statistical background subtraction using KDEs

In our method, the first objective is to obtain a probability density function (PDF) representative of the distribution of points in the $(g - r) \times r$ color-magnitude diagrams of the *field* and contaminated cluster regions. But first and foremost, it is important to define a reasonable area of the sky to call *field*. Kodama and Bower (2001), for example, uses a sizeable portion of the sky with an area of 137.5 arcmin^2 . Here, we opted to use a circular annulus with an inner radius of at least $4R_{200}$, the choice of which might depend on the presence of structures or gaps in the SDSS footprint, as shown in Fig. 5.3.

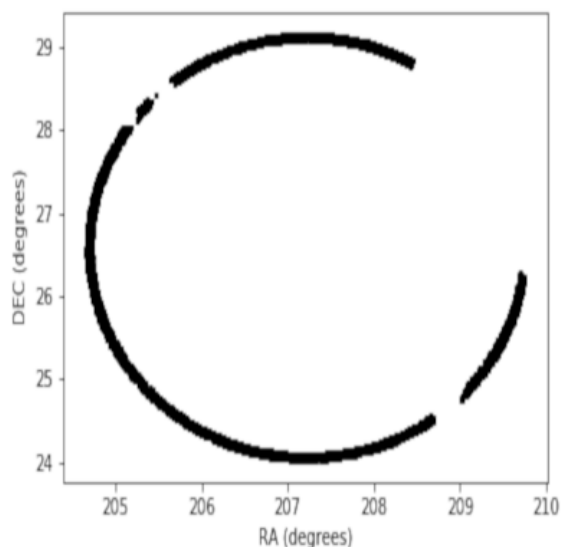


Figure 5.3: An example of a bad field choice for Abell 85, notice the gaps in the SDSS footprint. In these cases the region’s radius is increased by small increments, starting from $r_0 = 4R_{200}$, and visually checked, until a suitable and representative field region is obtained.

¹ docs.scipy.org/doc/scipy/reference/generated/scipy.stats.gaussian_kde.html.

With our PDFs in hands, we must assign a membership probability for each galaxy based on our PDF estimations. Taking a look at equation (5.1), either N_F^{bin} or N_{CLcont}^{bin} can be rewritten as:

$$N^{\text{bin}} = N_{\text{tot}} \iint_{\text{bin}} \hat{f}(\text{bin}) dA, \quad (5.8)$$

while N_{tot} is the total number of galaxies in the given region, and we use our kernel estimator \hat{f} as the PDF, calculated in the midpoint.

Now, making our bin infinitesimally small, Eq. (5.8) tends to zero, but the ratio in Eq. (5.1) tends to a finite number:

$$P(F) = \text{norm.} \frac{N_{F\text{tot}} \hat{f}_F}{N_{CL\text{tot}} \hat{f}_{CL}}. \quad (5.9)$$

Noting that *norm* is the ratio between the areas of the contaminated cluster region and the field, the above equation can neatly be rewritten as:

$$P(F) = \frac{\overline{\rho}_F \hat{f}_F}{\overline{\rho}_{CL} \hat{f}_{CL}}, \quad (5.10)$$

where $\overline{\rho}_F$ and $\overline{\rho}_{CL}$ are the mean densities of galaxies in each region (normally in units of *galaxies/arcmin*²).

This probability can be improved if we use photometric redshift information as a prior. Not all galaxies in SDSS have reliable photo-z error estimates. The ones that does so are flagged with *photoErrorClass* = 1. For these galaxies we can therefore use the equation:

$$P(CL) = \left(1 - \frac{\overline{\rho}_F \hat{f}_F}{\overline{\rho}_{CL} \hat{f}_{CL}} \right) \text{prior}(\text{photo-z}), \quad (5.11)$$

where we are now talking about the probability of the galaxy being a cluster member. The prior is taken to be the probability that the galaxy actually lies in the cluster redshift, assuming a gaussian distribution, and inside a tolerance interval:

$$\text{prior}(\text{photo-z}) = \int_{z_{cl}-\sigma}^{z_{cl}+\sigma} \text{gauss}(z|z_{gal}; \sigma_{gal}) dz. \quad (5.12)$$

It is worth noting that, while we showed how to obtain the probabilities for each galaxy directly, conceptually we actually derived a formula for the “true” PDF of galaxies in the cluster CMD, which hereby is called *clean*. To showcase the intuition behind it, it is useful to rewrite 5.11 as:

$$P(CL) = \frac{\overline{\rho_{CL}} \hat{f}_{CL}(r, g-r) - \overline{\rho_F} \hat{f}_F(r, g-r)}{\overline{\rho_{CL}} \hat{f}_{CL}(r, g-r)}, \quad (5.13)$$

without the photo-z prior, since we are treating the general case. It is also explicitly indicated that the KDEs are functions whose domain is the $(r, g-r)$ plane. Comparing 5.13 with equation 5.10, which gives the probability of a galaxy being from the *field*, we can expect that:

$$P(CL) = \frac{\overline{\rho_{CL}} \hat{f}_{CL}(r, g-r) - \overline{\rho_F} \hat{f}_F(r, g-r)}{\overline{\rho_{CL}} \hat{f}_{CL}(r, g-r)} = \frac{\overline{\rho_{clean}} \hat{f}_{clean}(r, g-r)}{\overline{\rho_{CL}} \hat{f}_{CL}(r, g-r)}. \quad (5.14)$$

Finally, comparing the numerators, we can define \hat{f}_{clean} as:

$$\hat{f}_{clean}(r, g-r) = \frac{\overline{\rho_{CL}} \hat{f}_{CL}(r, g-r) - \overline{\rho_F} \hat{f}_F(r, g-r)}{\overline{\rho_{CL}} - \overline{\rho_F}}. \quad (5.15)$$

Therefore \hat{f}_{clean} is the simple subtraction of the *field* KDE (\hat{f}_F) from the *dirty* KDE (\hat{f}_{CL}), normalized by the difference between mean galaxy densities of the projected 2D regions. Moreover, since by definition \hat{f}_{CL} and \hat{f}_F are normalized, \hat{f}_{clean} is also normalized:

$$\iint_{-\infty}^{\infty} \hat{f}_{clean} dr d(g-r) = \frac{\overline{\rho_{CL}} - \overline{\rho_F}}{\overline{\rho_{CL}} - \overline{\rho_F}} = 1. \quad (5.16)$$

In Fig. 5.4 is shown a schematic diagram of our method applied to Abell 1795. Comparing the elements of our general formula 5.15 with the figure, the *Dirty* cluster PDF is $\hat{f}_{CL}(r, g-r)$, the *Field* PDF is given by $\hat{f}_F(r, g-r)$, while the final result *Clean* cluster PDF is of course $\hat{f}_{clean}(r, g-r)$. In the figure there is also a Monte Carlo sample of a “true” galaxy population of A1795, to illustrate what the *clean* PDF represents.

5.2.2 Overall photometric properties

Since we are interested in photometric properties averaged over the entire population of galaxies, we do not need Monte Carlo runs to generate a clean sample of members. A more direct approach is to use the probabilities as weights for the desired quantity. For example, the average color of the galaxy population, taking into account the probability of membership, is given by:

$$\overline{(G-R)} = \frac{1}{\sum_{i=1}^n P_i} \sum_{i=1}^n P_i (G-R)_i, \quad (5.17)$$

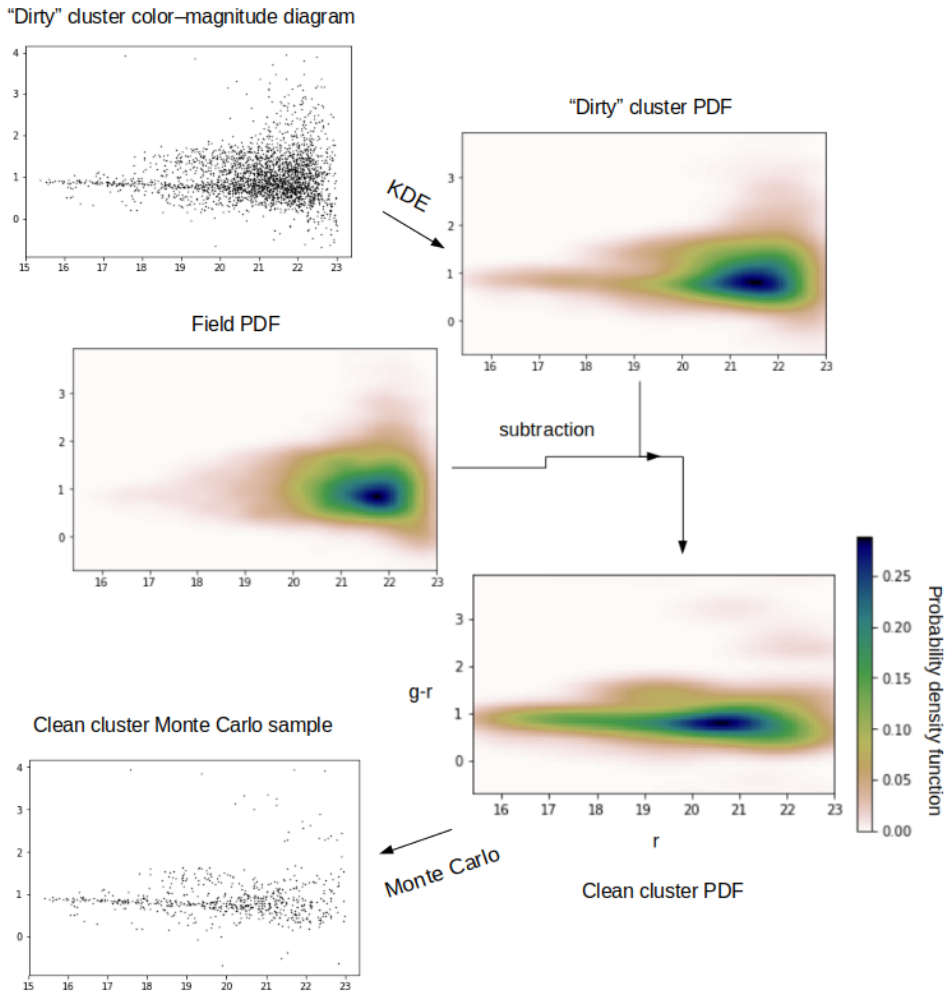


Figure 5.4: Schematics of the subtraction applied for A1795. Various axes labels were omitted for clarity. After using a KDE to obtain PDFs that are representative of the point distributions, the *clean* PDF is given by 5.15. The last step shows the result of a Monte Carlo run.

with G and R being absolute magnitudes, and P_i is estimated using the formula (5.11).

For the creation of histograms the same approach might be taken. Let's say one is interested in plotting the histogram of the distribution of galaxies around the red-sequence (as shall be used in this work to discriminate between galactic populations, in Fig. 5.5). In a bin where we count the number of galaxies with distances to the red-sequence that fall between $\Delta(G - R)$ and $\Delta(G - R) + binsize$, we might estimate the "effective number" by using the probability of a galaxy being a member:

$$N_{bin} = \sum_i P_i, \quad (5.18)$$

which evidently will not necessarily be an integer.

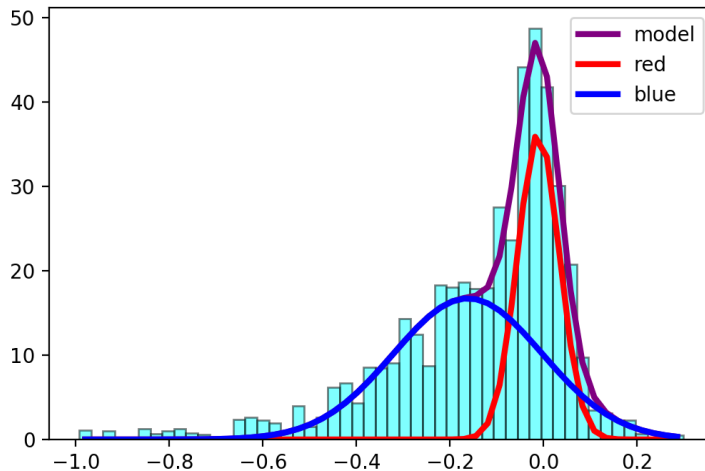


Figure 5.5: Histogram of the distance to the red-sequence, with the fitted red and blue populations. The weighted number of galaxies that fall within a bin are given by equation (5.18). This approach has the advantage of explicitly taking into account the probability of membership of each galaxy. If it has a 50% chance of being a member, it will count as 0.5 in the histogram, instead of a full 1.0. Therefore the histogram maps the *clean* PDF.

5.3 Final remarks

In conclusion it is worth noting the simplicity of the formula 5.15. With our KDEs in hands representing the *dirty* and the *field* PDFs, it is only necessary to calculate the normalizing factors to obtain a theoretical *clean* PDF, that is a simple weighted subtraction of the *field* from the *dirty* KDEs.

One small drawback of the method is that when calculating individual probabilities for each galaxy, using 5.11, for a few galaxies in the upper border of the CMD (red galaxies above the red-sequence) negative values are obtained, or in other words, the probability $P(F)$ of being a background galaxy is greater than one. These galaxies are deemed non-cluster members, and the probability of being a member is set to zero. Not much more than a couple galaxies per cluster had this issue.

We emphasize that these “negative” galaxies does not change the overall shape of the *clean* PDF, since it is a statistical function representing the distribution of hundreds (or thousands) of data points.

We will come back to this question in section 6.3.

Results and Analysis

6.1 Sample and overall cluster properties

In order to select our sample, we used the following criteria. The redshift range chosen was $0.03 < z < 0.3$, due to typical lack of good photon statistics for clusters further than $z = 0.3$, and also due to the 30 arcmin FoV of the EPIC cameras, that poses a limit to clusters that are too close to fit in the detectors. We sampled through clusters observed by XMM-Newton, that were also present in the SDSS footprint, and had exposure times greater than 12000 s. Due to problems of time consumption by the ESAS tasks (see section 6.2 below), and complexity of spectral analysis, the sample size was initially deemed to be sufficient at around a few tens of objects. Therefore, we randomly choose 21 clusters.

Worth mentioning is the case of Abell 781, the highest redshift cluster in our initial sample with $z = 0.298$, whose temperature and metallicity profiles extraction were not possible, with only average temperatures and metallicities measured. While working on this cluster, we noticed that it was very small on the field-of-view and showed strong bimodality. Thus, Abell 781 was not used further in our analysis, and our final sample size was set at 20. The final cluster sample used in this work is presented in table 6.1.

Appendix A shows the metallicity and temperature profiles of the clusters in our sample. Table 6.2 presents the temperature and metallicity measurements in two regions for each cluster, the *core* region defined as $R_c < 0.15 R_{500}$, and the *mean* or bulk region, defined as $0.15 R_{500} < R_m < 1.0 R_{500}$, with the core excluded. The exclusion of the core is widely used to estimate the mean temperature (Maughan et al., 2012). This is due to a strong bias induced in the temperature estimation of some clusters, specially strong cool-cores, that originate from a high density, low temperature core that inevitably brings the mean

temperature down if the region is not properly excluded. The radius R_{500} was estimated by an iterative method using the scaling relation (Evrard et al., 1996):

$$R_{500} = (1.24 \pm 0.09) \left(\frac{kTm}{10 \text{ keV}} \right)^{1/2} (1+z)^{-3/2} h^{-1} \text{ Mpc}, \quad (6.1)$$

where kTm is the mean emission-weighted temperature in units of keV and z is the cluster redshift.

The iterative method is as follows: a region that contains most of the cluster emission is used as a first guess, from where spectra are extracted and fit, thus obtaining a temperature (following the method explained in section 4); with this first approximation to kTm , we plug it into equation (6.1) and obtain a first estimate of R_{500} . Within this new region, we again extract and fit new spectra and repeat the process until convergence is attained (always excluding the core region in order to exclude the possible presence of a cool-core). In this way, the temperature estimation should be a fair approximation of the virial temperature associated with the gravitational potential, and thus, appropriate for estimating R_{500} .

Since it is not possible to extract temperature profiles for every galaxy cluster observation due to varying data quality (as was the case with Abell 781 in our initial sample), in the literature there are many definitions of a cool-core cluster using a plethora of physical properties, with many explored and compared very thoroughly, such as in the works of Hudson et al. (2010) and Andrade-Santos et al. (2017). In the present work, we use the straightforward definition of temperature drop. We compare the temperature of the innermost annulus of each temperature radial profile with the mean temperature kTm . If the first is, within the error bars, inferior to kTm , then the cluster is marked as cool-core (as simple as this definition sounds, it shows to be quite efficient in discriminating clusters when compared to other more complex criteria as shown in Hudson et al. (2010)). We emphasize that not all cool-cores in our sample necessarily has $kTc < kTm$ according to our definitions (kTc is the mean temperature inside $0.15R_{500}$). The only cluster where this oddity occurs is Abell 2065. Due to its extremely steep central temperature drop, and also steep temperature decline in the outskirts (figure A.4 of the appendix), kTc is slightly higher than kTm , but within the error bars, they might be considered equal.

Cluster	R.A. (deg)	DEC. (deg)	redshift	cool-core*	ObsID**	Exposure (s)
RXCJ0043.4-2037	10.84	-20.61	0.292	x	0042340201	14973
Abell 85	10.44	-9.37	0.052	✓	0065140101	13118
Abell 773	139.49	51.69	0.217	x	0084230601	25211
Abell 963	154.24	39.01	0.206	x	0084230701	27461
Abell 1763	203.8	41.0	0.223	x	0084230901	26937
Abell 1689	197.88	-1.35	0.183	x	0093030101	39763
RXJ2129.6+0005	322.40	0.094	0.2350	✓	0093030201	58916
Abell 1650	194.67	-1.76	0.084	x	0093200101	43103
Abell 1795	207.24	26.58	0.062	✓	0097820101	66559
Abell 1775	205.45	26.35	0.0717	x	0108460101	33021
E1455+2232	224.30	22.34	0.2578	✓	0108670201	46705
Abell 2390	328.41	17.69	0.231	✓	0111270101	23105
Abell 1914	216.49	37.83	0.171	x	0112230201	25815
Abell 2034	227.53	33.49	0.151	x	0149880101	26413
Abell 2065	230.61	27.7	0.072	✓	0202080201	34110
ZwCl1215	184.41	3.65	0.077	x	0300211401	29215
Abell 781	140.09	30.49	0.298	x	0401170101	81913
RXCJ1720.1+2638	260.03	26.61	0.164	✓	0500670201	30409
Abell 1201	168.22	13.43	0.1688	x	0500760101	51825
Abell 1413	178.81	23.39	0.143	x	0502690201	82448
Abell 2261	260.61	32.14	0.224	x	0693180901	29916

Table 6.1 - List of galaxy clusters used in this work, all observed by XMM-Newton. * according to our definition outlined in 6.1. ** As used for identification in the XMM-Newton Science Archive (XSA).

6.2 Applicability and performance of the X-ray spectral fitting and data reduction algorithm

Despite the complexity and number of model parameters the method employed for data reduction and spectral fitting, based on (Snowden et al., 2008), proved to be rather robust. Nevertheless it is useful to point some of its drawbacks.

Firstly, the extraction of the QPB reduced spectra for several annuli could very often take several hours, depending on the hardware performance. The tasks used, *mos-back* and *pn-back*, are perl scripts integral to the ESAS package that takes no input or parameters that makes the extraction quicker. Any improvement on time performance would require explicit editing of the task's source code.

Another part of the data reduction that might be problematic is the point-source detection using *cheese* (since we are interested in the cluster diffuse emission). Eventually the task would miss a few obvious sources that had to be manually excluded. But the greatest drawback is that a human eye is always needed at the end to visually check the suitability of the mask generated, which eventually leads to some parameter tweaking and reruns of the task, which might take some extra time. Even if the user gets creative and employs some kind of cross reference with other point-source detection methods, or completely replace the task *cheese* altogether, eventually it is always a good idea to visually check the end product nonetheless.

Last but not least is the tweaking of model parameters during the spectral fitting process, including manually linking and freezing/thawing (i.e, making some parameter fixed during the fitting or making it a free parameter). The script developed in this project automatically deals with parameters constraints, but eventually *XSPEC* might get stuck in some local minimum chi-square in the parameter space, or some parameter normalization might freeze with a null value or overshoot to infinity. These situations often arise due to lower count rates from the outer regions of some observations. Unfortunately, there is no obvious method to deal with these situations autonomously, and human intervention is still needed.

Despite these problems the advantages of this method are evident. Even in the eventual situation where a blank-sky map represents a good approximation of the “true” background, the method employed here has the advantage of quantifying the contribution of each background component. This of course has a great value for those interested in the X-ray and particle background itself.

6.3 The KDE method for background galaxy subtraction

The method developed in this work for the subtraction of background galaxies, using KDEs to estimate galaxy number density in the $(g-r) \times r$ color-magnitude diagram (CMD), generates as an output a PDF, that we call “*clean*”, that is a probabilistic estimate of the true galaxy distribution in the CMD, given by equation (5.15). We consider all galaxies in the FoV, inside a radius of R_{200} (which is a standard approximation to the virial radius). The *clean* PDF in turn is used to assign a probability of membership for every galaxy in

the cluster FoV. Evidently, all galaxies that have spectroscopic redshifts in the SDSS, and were confirmed as members within the informed errors, were promptly assigned probability of membership = 1.0, while the ones rejected are assigned null probability.

In the appendix B we show the *clean* PDFs for our cluster sample, including the *dirty* KDEs, which are simply the KDEs generated from the raw CMD comprising all galaxies in the cluster FoV, and the *field* KDEs, obtained as explained in chapter 5. The galaxies superimposed on the *clean* PDFs are not real, they are generated by a simple Monte Carlo sampling using the *clean* PDFs to estimate the probability of a galaxy in the FoV being a member of the cluster. This is not used in the analysis and is a relic of the original binning method, and serve only to illustrate the effectiveness of the background reduction.

The conceptual simplicity of the method contributes to its reliability. It also proved to be surprisingly sensitive to the presence of structures in the CMDs, prominently the red-sequence. One extreme case is Abell 85 that, mainly due to its proximity, has a vast number of background galaxies in its FoV that makes the red-sequence indistinguishable from background noise in the densest regions of the CMD, as seen in figure 6.1. The method proved to be very effective in detecting the red-sequence in these scenarios.

Even more subtle structures can be seen in the *clean* PDF of some clusters, as in figure 6.2, for example. Above the red-sequence there is a slight extension in yellow/green, with also some minor regions with non zero probability in the upper right corner. Similar regions can also be seen in figure 6.1. Although these might be mere residues of the statistical method, they might also represent sub-structures of the cluster itself, or even background groups or clusters in higher redshifts. To confirm these suspicions, careful examination of each system would be needed.

6.4 The “universal” temperature profile and self-similarity

Here, we apply the methods developed and described above in a study of the ICM temperature radial profile.

It is well established that galaxy clusters present self-similar properties, or in other words, they are scaled versions of each other (see, e.g. Böhringer and Werner, 2010). To be more precise, when comparing profiles of thermodynamical properties of the ICM, one would expect that these profiles would present the same shape, in average, while

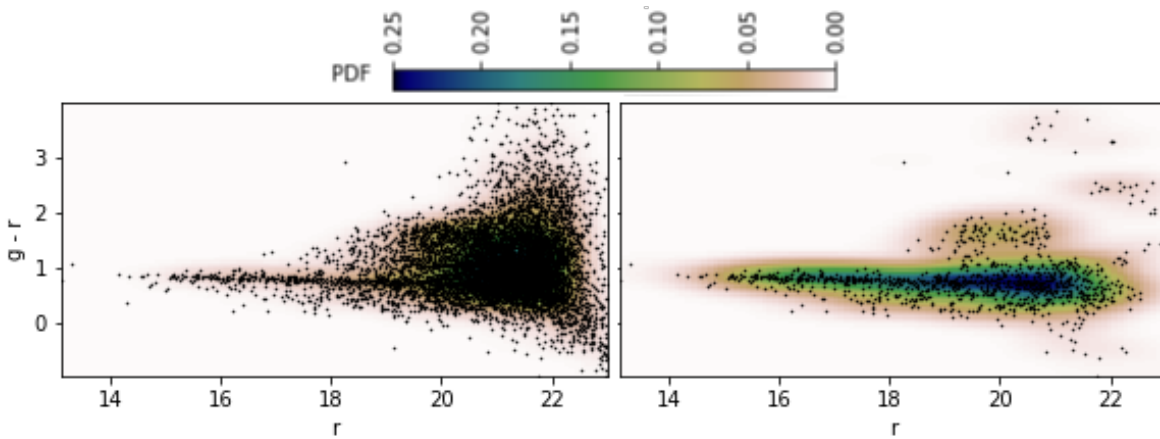


Figure 6.1: KDE subtraction applied to Abell 85. Left: *dirty* KDE and real FoV galaxies; right: *clean* PDF and monte-carlo galaxies. Notice how effectively the red-sequence is separated from background noise.

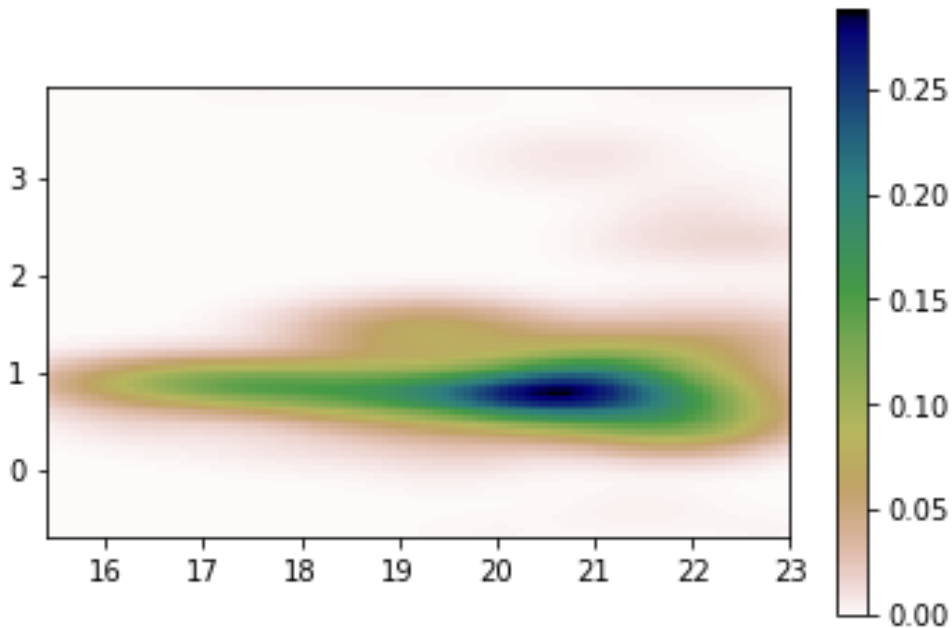


Figure 6.2: *Clean* PDF for Abell 1795. Notice the subtle linear non-zero probabilities above the cluster's red-sequence. These might be red-sequences from substructures or galaxy groups in the FoV.

differing mostly in normalization after scaling the radial distance (i.e., by scaling to R_{200} or R_{500} , for example). Several authors verified this self-similar behaviour when comparing temperature, mass and entropy profiles of real galaxy clusters, while others tried to recreate this phenomenon in simulations, with varied degrees of success (e.g. Kaastra et al., 2008).

We were able to confirm this scenario of self-similarity for the temperature profiles with

our sample (Fig. 6.3), and we also compared our results to the radial profiles obtained by Pratt et al. (2007), which also used XMM-Newton data of a different sample comprising of 15 galaxy clusters (Fig. 6.4). Notice that although there is a considerable scatter in the central regions (stemming from the presence or not of a cool-core), the outskirts are surprisingly similar. These results serve as a proof of concept for the method employed in this work for spectral analysis, since the referred authors used a completely different procedure of X-ray data analysis and reduction.

Another interesting observation is that the dichotomy between CCs and NCCs, in other words where the temperature begins to decline in CCs, becomes more accentuated around $R \approx 0.1 - 0.15 R_{500}$. This corroborates the choice of $R_c = 0.15 R_{500}$ as our core region, as mentioned above. This is most evident in the log plot of figure 6.3. Another corroboration of our choice of regions stems from the fact that the profiles were scaled by kTm , measured within $0.15 R_{500} < r < 1.0 R_{500}$. The low scatter of the intermediate regions shows that kTm has a solid physical origin, and therefore must be a good approximation of the virial temperature (equilibrium temperature).

6.5 Metal content in the core of galaxy clusters

From our spectral analysis, we also obtain information regarding the abundance in the ICM. It is well known (for exemple, De Grandi and Molendi, 2001) that cool-core clusters present a metal rich core compared to non-cool-cores. The origin of these metals is widely debated, although some believe this peak might have an origin in the Brightest Cluster Galaxy (BCG), specifically from SN Ia explosions where the metals did not escape the gravitational potential well (see, Kaastra et al., 2008; Böhringer and Werner, 2010; Mernier et al., 2018).

We noted an interesting correlation between the cool-core strength (represented by the ratio kT_0/kTm , where kT_0 is the temperature of the innermost region of the temperature profile, and kTm the average temperature inside $0.15 R_{500} < r < R_{500}$) and the core metallicity as illustrated in Fig. 6.5. We see this as an indicator that the same feedback mechanisms that may deposit energy in the core are also responsible for the transport and mixing of metals towards the cluster outskirts (or preserving a metal rich core, in the lack of said mechanisms). Some similar results might be found in the literature, as for example

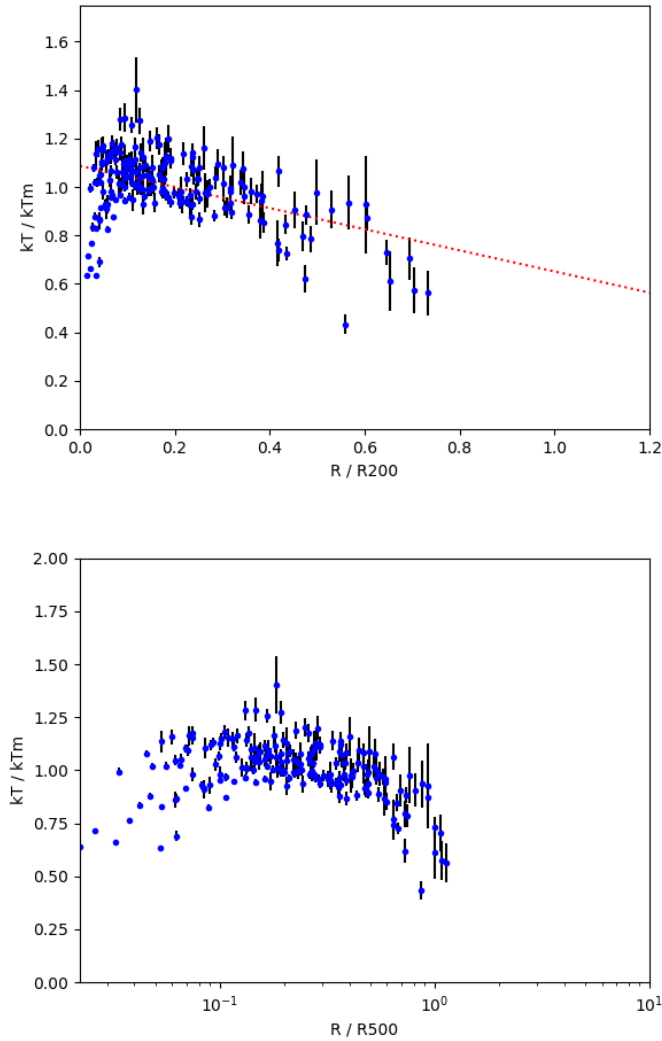


Figure 6.3: Temperature profiles of our sample in linear (upper) and logarithmic (lower) scales. The profiles are scaled by the average temperature inside R_{500} . A simple linear fit is shown in red in the linear scale, which only represents the slope in the outskirts. The radius scale in the linear fit is in units of R_{200} so it can be compared with the work of Pratt et al. (2007) as show in figure 6.4. Using the logarithmic scale it becomes even more evident the self-similar nature of galaxy clusters (specially in the intermediate regions where there is lower scatter).

in Leccardi et al. (2010).

6.5.1 Comparison with Leccardi et al. (2010) results

Using a sample of 60 clusters, Leccardi et al. (2010) characterize their cores using thermodynamic and chemical properties and employ an entropy estimator (σ) used to classify clusters into high, medium and low entropy cores: HEC, MEC and LEC respectively. The entropy estimator, called pseudo-entropy ratio, is given by:

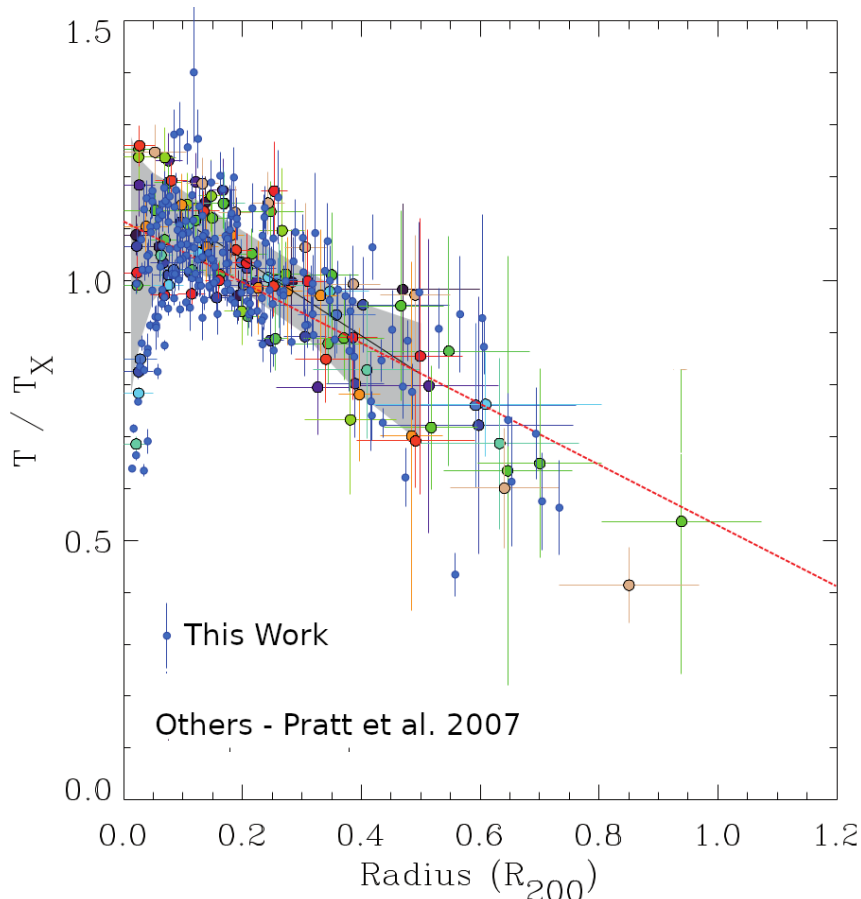


Figure 6.4: Temperature profiles of our sample (blue) and of Pratt et al. (2007) (colored points). The profiles are scaled by the average temperature inside R_{500} (which is equivalent to $0.65 R_{200}$). A simple linear fit is shown in red, which only represents the slope in the outskirts.

$$\sigma = \left(\frac{T_{in}}{T_{out}} \right) \times \left(\frac{EM_{in}}{EM_{out}} \right)^{-1/3}, \quad (6.2)$$

Where the region *IN* is defined as interior to $0.05 R_{180}$ and *OUT* as $[0.05-0.20] R_{180}$, while *EM* is the region emission measure defined as (Sarazin, 1986):

$$EM = \int n_p n_e dV, \quad (6.3)$$

where n_e and n_p are the electron and proton numerical densities, and the integral is done over the volume of the cluster.

They proceed to plot the metallicity inside the *IN* region versus the pseudo-entropy ratio as seen in figure 6.6. Here, we see a very similar result compared to figure 6.5. In blue are cool-cores, green are intermediate systems, while red and gray are non cool-cores. Moreover, the red color corresponds to merger (or collision) systems, while gray are non-

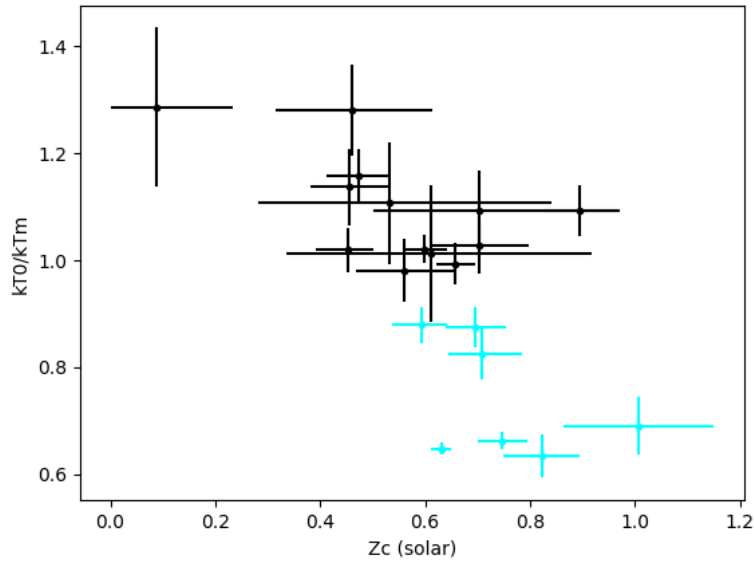


Figure 6.5: Cool-core strength plotted against core metallicity (inside $0.15 R_{500}$). Note that there is a continuous transition between cool-core and non cool-core systems. Cool-core clusters have a $kT_0/kTm < 1.0$ (which is a commonly used diagnostic, Hudson et al. (2010)) and are here presented in cyan.

interacting objects. Evidently a direct comparison is impossible due to different region sizes and the use of different parameters, but it is clear that they illustrate the same physical processes. This once more shows that the disruption or absence of high metallicity cores and the heating of the ICM are correlated.

6.6 Correlations between galaxy photometry and X-ray properties

It is well known that the metals that enrich the ICM originate mostly inside the galaxies from stellar nucleosynthesis, while significantly smaller amounts may be produced “in situ” by the stars that make up the intracluster light. Therefore one might argue that there must be some correlation between the photometric properties of the galaxies and the overall X-ray observables obtained by spectral analysis. With this in mind we explored the relationship between the mean metallicity, temperature and colors of the galaxy population.

Figure 6.7 shows the relation between Zm , kTm and mean $(g - r)$ color index. As explained previously, Zm and kTm are obtained by spectral fits in the region $0.15 R_{500} < r < 1.0 R_{500}$, while the galaxies are contained within a volume with a radius of R_{200} . A stronger correlation is seen in the plot relating to the mean abundance, while the tempe-

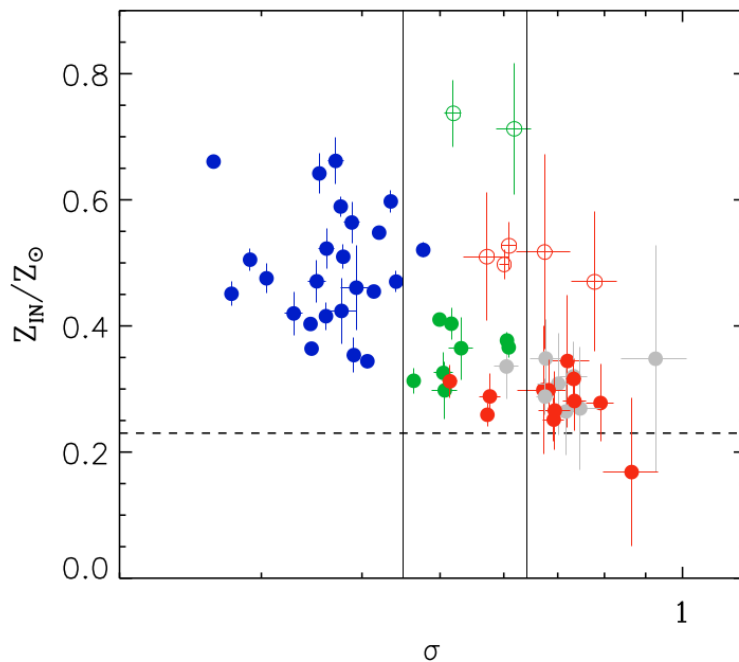


Figure 6.6: Core metallicity versus pseudo-entropy ratio from (Leccardi et al., 2010). Notice the transition from cool-cores to non cool-core clusters comparable to our results in figure 6.5. In blue are cool-core clusters, green are intermediate cases, while red and gray are non cool-cores, divided in mergers and non interacting respectively. Solid vertical lines represent different entropy classes (view text) while the horizontal dashed line is the mean metallicity from the outer regions of clusters.

temperature correlation is significantly weaker. Moreover, the presence of cool-cores does not appear to have any influence as no trend is observed. These results show that higher metallicity and lower temperature clusters appear to have a bluer galactic population. To better understand if these correlations imply an underlying unifying cause, the information of both plots are combined in a single graph, as shown in figure 6.8.

Figure 6.8 shows that the three quantities are correlated, while still not showing any dependence on cool-cores. While cooler clusters are metal rich and have a bluer galactic population, higher temperature clusters are metal poor and have a slightly redder population. The most likely explanation for this relationship is the mass difference. By the well established $M - T_x$ relation, hot clusters also tends to be more massive (Evrard et al., 1996; Hjorth et al., 1998). Therefore our results imply that the mass of clusters are correlated to the color of the galactic population.

This trend of metallicity with cluster temperature have already been observed. Balestra et al. (2007) showed that for clusters with $kT < 5$ keV the Fe abundance is on average

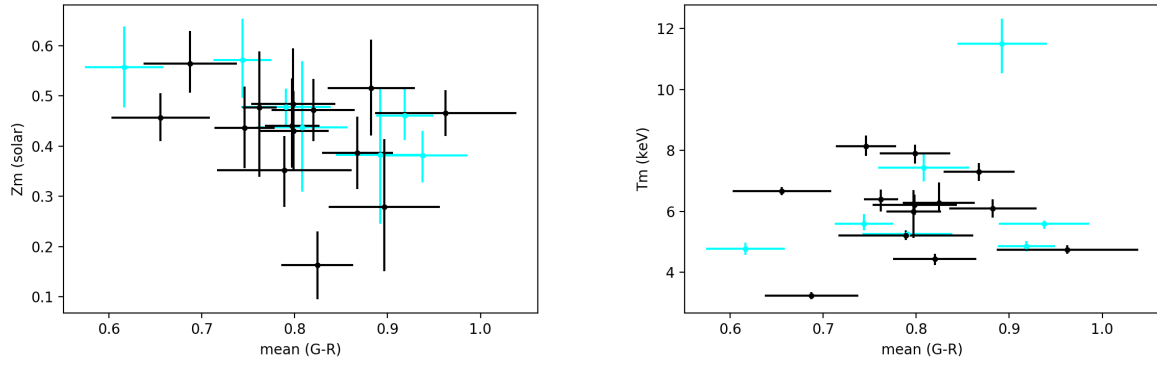


Figure 6.7: Mean metallicity and mean temperature plotted against mean $(g - r)$ color, computed inside R_{200} . Cool-core clusters are in cyan.

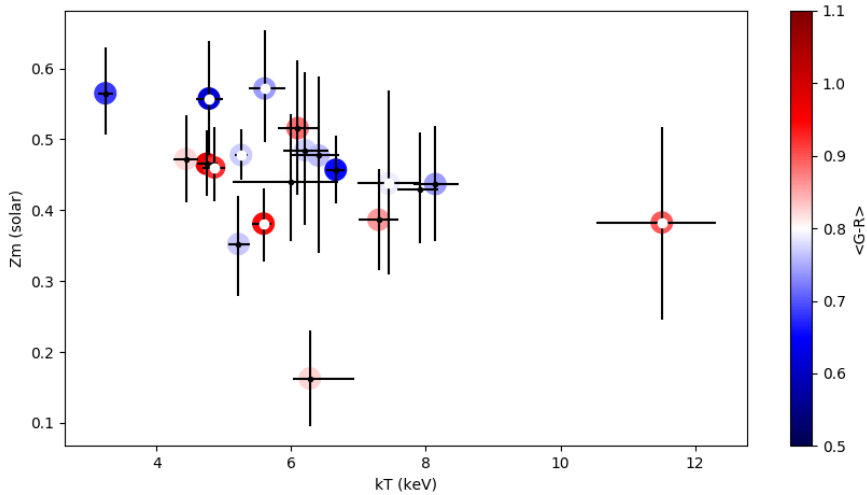


Figure 6.8: Mean metallicity plotted against mean temperature, both with the core excluded. Color coded from blue to red is the mean $(g - r)$ color index. White circles are cool-core clusters.

double than that of hotter clusters, for measurements within $0.15 - 0.3R_{500}$. The most favourable explanation is that this trend originates from the variable stellar over gas mass ratios of clusters (Böhringer and Werner, 2010). As mentioned in chapter 2, larger more massive clusters have a larger ICM mass compared to the stellar mass, in other words, the star formation efficiency is lower for more massive clusters (Laganá et al., 2013). With proportionally more stars and less ICM to dilute the metals, less massive clusters are therefore more likely to be metal rich. Although our results admittedly present a rather weak correlation between the three studied properties, they fit extremely well in the scenario explained above.

Another interesting property is the presence of a color gradient between outer and inner regions of clusters. We therefore define the gradient as:

$$grad(g - r) = \frac{\overline{(g - r)}_{(0.5R_{200} < R < R_{200})} - \overline{(g - r)}_{(R < 0.5R_{200})}}{\log(0.75R_{200}) - \log(0.25R_{200})}. \quad (6.4)$$

A similar formula is used to study color gradients within galaxies (Marian et al., 2018). The relation of the color gradient with the mean metallicity is presented in figure 6.9, with the mean temperature color coded. Again, no apparent dichotomy between cool-cores and non-cool-cores is observed. Interestingly we see that metal rich clusters have a stronger negative gradient, i.e. there is a greater difference between inner and outer galaxies, with a redder population residing in the inner regions. Metal poor (more massive) clusters tend to be more uniform, with a gradient closer to zero, or possibly slightly positive. These might be indication of not so old merger activity, with newer (bluer) galaxies residing in the cluster outskirts. The dependence on temperature (and mass) is slightly clearer on figure 6.10.

This scenario, where less massive clusters show a more intense color gradient, is corroborated if we assume that these systems had a less intensive merger history, since they did not grow as much as massive clusters. Therefore their galaxy population evolved passively reflecting the Butcher-Oemler effect, with poor clusters having a greater population of blue galaxies (Margoniner et al., 2001).

The results presented in this section demonstrate the intricate relationship that galaxies have with their environment. It also proves that our statistical approach of dealing with the photometry of the galaxy population has a solid footing in real physics, i.e. they probe actual physical process that vary in intensity with cluster total mass, and that also leaves imprints in the mean color of the galaxy population.

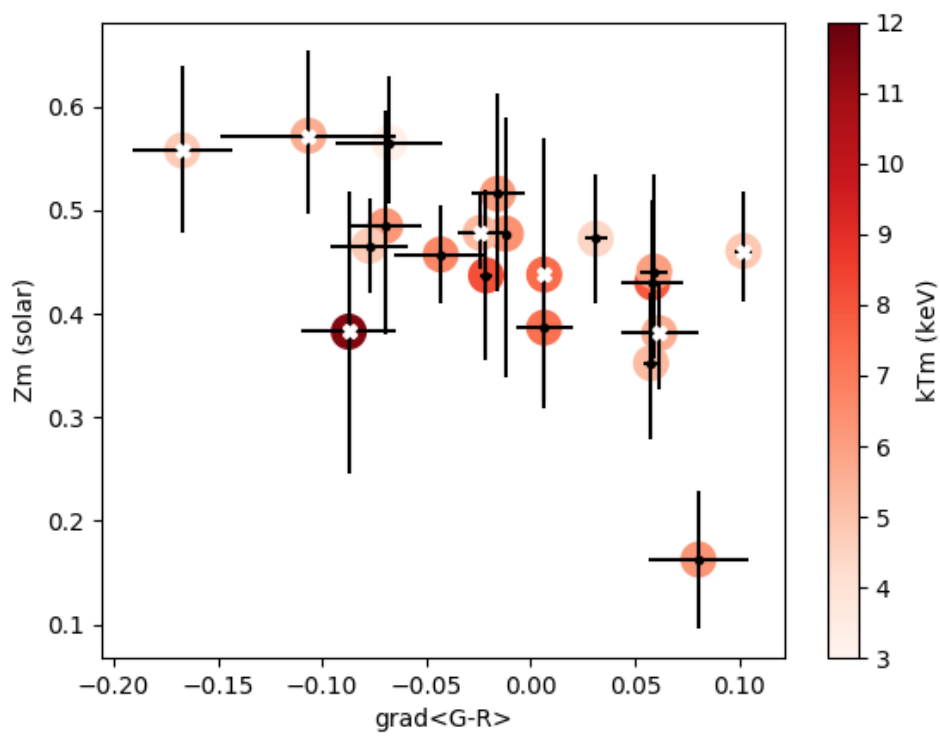


Figure 6.9: Mean metallicity plotted against the color gradient, between $r < 0.5 R_{200}$ and $r > 0.5 R_{200}$. Color coded in the vertical bar is the average temperature of the ICM. White Stars are cool-core clusters.

Cluster	kTc (keV)	kTm (keV)	Zc (solar)	Zm (solar)	R_{500} (arcmin)	cool-core
RXCJ0043.4-2037	$7.02^{+0.72}_{-0.70}$	$5.94^{+0.49}_{-0.45}$	$0.53^{+0.31}_{-0.25}$	$0.28^{+0.13}_{-0.12}$	3.57	x
Abell 85	$4.66^{+0.05}_{-0.07}$	$5.59^{+0.11}_{-0.17}$	$0.75^{+0.05}_{-0.05}$	$0.38^{+0.05}_{-0.05}$	19.99	✓
Abell 773	$7.85^{+0.44}_{-0.44}$	$6.21^{+0.34}_{-0.33}$	$0.46^{+0.15}_{-0.14}$	$0.48^{+0.11}_{-0.10}$	4.96	x
Abell 963	$5.85^{+0.22}_{-0.20}$	$6.10^{+0.30}_{-0.29}$	$0.56^{+0.10}_{-0.09}$	$0.51^{+0.10}_{-0.09}$	5.14	x
Abell 1763	$7.10^{+0.57}_{-0.48}$	$6.40^{+0.31}_{-0.41}$	$0.70^{+0.27}_{-0.20}$	$0.48^{+0.11}_{-0.14}$	4.67	x
Abell 1689	$8.34^{+0.15}_{-0.14}$	$7.91^{+0.28}_{-0.34}$	$0.45^{+0.05}_{-0.06}$	$0.43^{+0.08}_{-0.08}$	6.82	x
RXJ2129.6+0005	$5.03^{+0.10}_{-0.11}$	$5.60^{+0.31}_{-0.23}$	$0.71^{+0.08}_{-0.06}$	$0.57^{+0.08}_{-0.07}$	4.34	✓
Abell 1650	$5.17^{+0.06}_{-0.06}$	$4.74^{+0.15}_{-0.14}$	$0.66^{+0.04}_{-0.04}$	$0.46^{+0.05}_{-0.04}$	11.31	x
Abell 1795	$4.58^{+0.04}_{-0.04}$	$5.25^{+0.09}_{-0.10}$	$0.63^{+0.02}_{-0.02}$	$0.32^{+0.04}_{-0.03}$	17.20	✓
Abell 1775	$3.66^{+0.08}_{-0.08}$	$3.24^{+0.11}_{-0.11}$	$0.89^{+0.07}_{-0.07}$	$0.56^{+0.06}_{-0.06}$	11.07	x
E1455+2232	$4.25^{+0.08}_{-0.06}$	$4.78^{+0.20}_{-0.20}$	$0.70^{+0.06}_{-0.06}$	$0.56^{+0.08}_{-0.08}$	3.60	✓
Abell 2390	$9.27^{+0.44}_{-0.45}$	$11.51^{+0.81}_{-0.98}$	$1.01^{+0.14}_{-0.14}$	$0.38^{+0.13}_{-0.14}$	6.12	✓
Abell 1914	$8.90^{+0.31}_{-0.30}$	$8.14^{+0.35}_{-0.32}$	$0.46^{+0.08}_{-0.07}$	$0.44^{+0.08}_{-0.08}$	7.21	x
Abell 2034	$8.01^{+0.48}_{-0.59}$	$6.28^{+0.67}_{-0.26}$	$0.09^{+0.14}_{-0.09}$	$0.16^{+0.07}_{-0.07}$	7.18	x
Abell 2065	$5.00^{+0.07}_{-0.11}$	$4.85^{+0.17}_{-0.17}$	$0.59^{+0.05}_{-0.06}$	$0.46^{+0.06}_{-0.05}$	13.78	✓
ZwCl1215	$6.00^{+0.19}_{-0.15}$	$5.21^{+0.16}_{-0.15}$	$0.47^{+0.06}_{-0.06}$	$0.35^{+0.07}_{-0.07}$	13.15	x
Abell 781	$6.64^{+0.74}_{-0.65}$	$6.00^{+0.70}_{-0.87}$	$0.61^{+0.30}_{-0.27}$	$0.44^{+0.09}_{-0.08}$	3.49	x
RXCJ1720.1+2638	$5.68^{+0.13}_{-0.15}$	$7.44^{+0.45}_{-0.45}$	$0.82^{+0.07}_{-0.07}$	$0.44^{+0.13}_{-0.13}$	7.27	✓
Abell 1201	$4.64^{+0.17}_{-0.14}$	$4.43^{+0.18}_{-0.19}$	$0.70^{+0.09}_{-0.09}$	$0.47^{+0.06}_{-0.06}$	5.42	x
Abell 1413	$6.81^{+0.13}_{-0.08}$	$6.66^{+0.14}_{-0.13}$	$0.60^{+0.04}_{-0.04}$	$0.46^{+0.05}_{-0.05}$	7.90	x
Abell 2261	$7.53^{+0.20}_{-0.22}$	$7.30^{+0.29}_{-0.30}$	$0.61^{+0.08}_{-0.07}$	$0.39^{+0.07}_{-0.07}$	5.14	x

Table 6.2 - Table containing the adjusted temperatures and metallicities for the core region (kTc and Zc , comprising $r < 0.15 R_{500}$) and for the bulk of the cluster, excluding the core (kTm and Zm , comprising $0.15 R_{500} < r < 1.0 R_{500}$). R_{500} is estimated by an iterative method as described in section 6.1. Errors represent a 90% confidence interval.

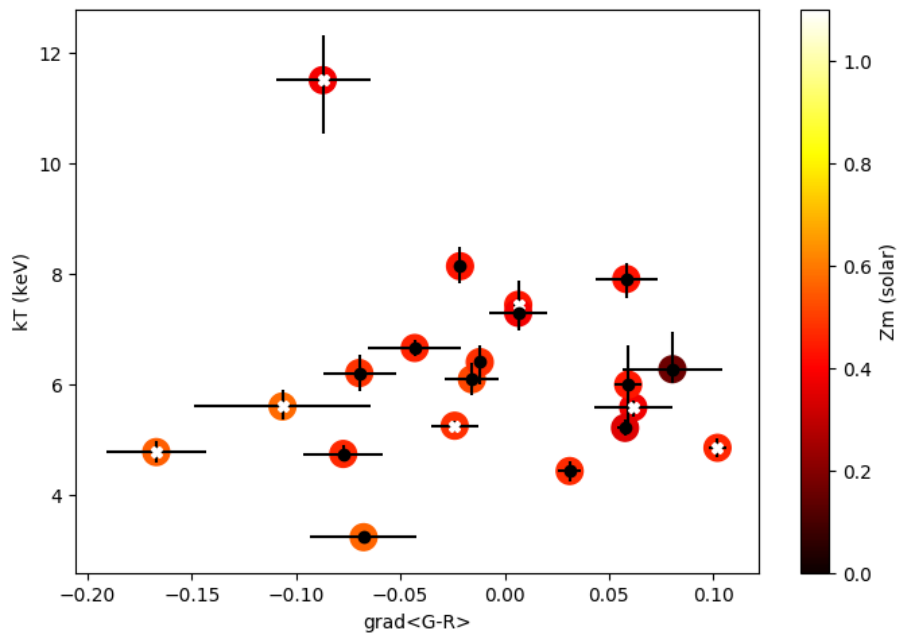


Figure 6.10: Mean temperature plotted against the color gradient, between $r < 0.5 R_{200}$ and $r > 0.5 R_{200}$. Color coded in the vertical bar is the average metallicity of the ICM. White Stars are cool-core clusters.

Conclusion

In this work, with the objective of studying photometrical properties of galaxies in cool-core and non-cool-core clusters, it was developed a novel technique of background (and foreground) galaxy subtraction that assigns a probability of membership for each galaxy. Furthermore, for the X-ray spectral analysis, it was implemented and employed a comprehensive methodology first described in Snowden et al. (2008) that explicitly models the X-ray and particle backgrounds. With this arsenal of tools in our disposal, some interesting results and considerations were obtained, and not only they shed light in the cluster-galactic population relationship, they also proved to be a great test for the methodology developed and employed in this work.

Despite its complexity, the method applied for the spectral fitting showed to be reliable and robust. We successfully dealt with the multitude of parameters and were capable of obtaining temperature and metallicity profiles for our sample. By stacking the temperature profiles, normalized by the mean temperature (within $0.15 R_{500} < r < 1.0 R_{500}$), we were able to verify the self-similarity of galaxy clusters. Although showing a spread in the inner regions (presence or not of a cool-core), the temperature profiles of galaxy clusters are surprisingly similar in the outskirts and intermediate regions.

The method of background galaxy subtraction using KDEs showed a remarkable sensitivity to detect the red-sequence and minor details and structures in the CMDs. Also noteworthy is the simplicity of the formula for estimating the *clean* PDF, equation 5.15, and for calculating the probability of membership, equation 5.11. Since it is essentially a probabilistic technique, it avoids methods that involve magnitude and color cuts in the CMD to determine cluster membership. Moreover, the method was applied only to the $(g - r) \times r$ CMD, but nothing prevents it to be applied to different colors. This might be

a good topic of investigation for further works.

By employing the central temperature drop criteria (kT_0/kT_m) to distinguish between cool-cores and non-cool-cores, and using it as a parameter to measure "cool-core strength", we found a strong correlation with the core ($r < 0.15 R_{500}$) metallicity (Z_c). Also present is a continuous transition between CCs and NCCs, covering intermediate values of Z_c . This result illustrates the close relationship between cool cores and the high metallicity peak found in CCs. This means that the feedback mechanisms that dissipate and dilute the high metallicity cores, might simultaneously be responsible for the heating and disruption of cool cores. The most likely candidates are major mergers and AGN feedback.

Finally, when investigating correlations between X-ray and photometric properties, it was established that the mean metallicity, temperature and color of galaxy clusters have a dependency on mass, and therefore are intertwined. Due to the decrease of the stellar mass over gas mass ratio with increasing total cluster mass (or temperature), cooler (or less massive) clusters have more efficient star formation, with a galaxy population that is bluer, and a metal rich ICM. Moreover, more massive clusters tend to have a more uniform (and redder) galaxy population, while less massive systems show stronger color gradients. No dichotomy was found in these correlations between CCs and NCCs. But we note that, since CCs are on average less massive, more statistically complete samples of clusters might be more efficient in differentiating photometric properties between these classifications.

To further improve on our work and methods, several ideas might be presented. Maybe the most evident is the lack of X-ray surface brightness profiles in the current work. This coupled with X-ray spectroscopy, could provide reliable mass estimates to verify our considerations regarding the mass dependency of the mean cluster temperature, metallicity and galaxy colors. The use of surface brightness profiles could also make possible further exploration of a greater variety of cool-core definitions. Furthermore, improvements on our spectral fitting scripts could be made, to completely eliminate the need of user input. With a more efficient and reliable script, the cluster sample can be increased to enhance the statistical significance of the explored correlations in chapter 6. On the photometric side, correlations with the BCG properties can be explored, as well the use of other higher energy filters, such as the SDSS u band, to better probe star formation.

Bibliography

- Abazajian K., Adelman-McCarthy J. K., Agüeros M. A., Allam S. S., Anderson S. F., Annis J., Bahcall N. A., Baldry I. K., Bastian S., Berlind The First Data Release of the Sloan Digital Sky Survey, *AJ*, 2003, vol. 126, p. 2081
- Abell G. O., The Distribution of Rich Clusters of Galaxies., *ApJS*, 1958, vol. 3, p. 211
- Abell G. O., Corwin Harold G. J., Olowin R. P., A Catalog of Rich Clusters of Galaxies, *ApJS*, 1989, vol. 70, p. 1
- Andrade-Santos F., Jones C., Forman W. R., Lovisari L., Vikhlinin A., van Weeren R. J., Murray S. S., Arnaud M., Pratt G. W., et al. The Fraction of Cool-core Clusters in X-Ray versus SZ Samples Using Chandra Observations, *ApJ*, 2017, vol. 843, p. 76
- Arnaud K., Smith R., Siemiginowska A., Handbook of X-ray Astronomy. Cambridge Univ. Press, 2011
- Aschenbach B., Briel U. G., Haberl F., Braeuninger H. W., Burkert W., Oppitz A., Gondoin P., Lumb D. H., Imaging performance of the XMM-Newton x-ray telescopes. In Proc. SPIE, vol. 4012 of Society of Photo-Optical Instrumentation Engineers (SPIE) Conference Series, 2000, p. 731
- Balestra I., Tozzi P., Ettori S., Rosati P., Borgani S., Mainieri V., Norman C., Viola M., Tracing the evolution in the iron content of the intra-cluster medium, *A&A*, 2007, vol. 462, p. 429
- Benítez N., Dupke R., Moles M., Sodr e L., Cenarro A. J., Mar n Franch A., Taylor K., Crist bal D., Fern ndez-Soto A., Mendes de Oliveira C., J-PAS Collaboration, J-PAS: The Javalambre-Physics of the Accelerated Universe Astrophysical Survey. In Highlights of Spanish Astrophysics VIII , 2015, p. 148
- Birkinshaw M., Using the Sunyaev-Zel'dovich Effect to Probe the Gas in Clusters. In Clusters of Galaxies: Probes of Cosmological Structure and Galaxy Evolution , 2004, p. 161
- Birkinshaw M., Gull S. F., Northover K. J. E., Extent of hot intergalactic gas in the cluster Abell 2218, *Nature*, 1978, vol. 275, p. 40,41

- Biviano A., From Messier to Abell: 200 Years of Science with Galaxy Clusters. In *Constructing the Universe with Clusters of Galaxies*, 2000, p. 1
- Böhringer H., Werner N., X-ray spectroscopy of galaxy clusters: studying astrophysical processes in the largest celestial laboratories, *A&A Rev.*, 2010, vol. 18, p. 127
- Burns J. O., Hallman E. J., Gantner B., Motl P. M., Norman M. L., Why Do Only Some Galaxy Clusters Have Cool Cores?, *ApJ*, 2008, vol. 675, p. 1125
- Butcher H., Oemler A. J., The evolution of galaxies in clusters. V. A study of populations since $Z = 0.5$, *ApJ*, 1984, vol. 285, p. 426
- Cavaliere A., Fusco-Femiano R., X-rays from hot plasma in clusters of galaxies., *A&A*, 1976, vol. 500, p. 95
- David L. P., Nulsen P. E. J., McNamara B. R., Forman W., Jones C., Ponman T., Robertson B., Wise M., A High-Resolution Study of the Hydra A Cluster with Chandra: Comparison of the Core Mass Distribution with Theoretical Predictions and Evidence for Feedback in the Cooling Flow, *ApJ*, 2001, vol. 557, p. 546
- De Grandi S., Molendi S., Metallicity Gradients in X-Ray Clusters of Galaxies, *ApJ*, 2001, vol. 551, p. 153
- den Herder J. W., Brinkman A. C., Kahn S. M., Branduardi-Raymont G., Thomsen K., Aarts H., Audard M., Bixler J. V., den Boggende A. J., Cottam J., Decker T., Dubbeldam L., Erd C., Goulooze H., Güdel M., Guttridge P., Hailey C. J., The Reflection Grating Spectrometer on board XMM-Newton, *A&A*, 2001, vol. 365, p. L7
- Evrard A. E., Metzler C. A., Navarro J. F., Mass Estimates of X-Ray Clusters, *ApJ*, 1996, vol. 469, p. 494
- Faber S. M., Variations in Spectral-Energy Distributions and Absorption-Line Strengths among Elliptical Galaxies, *ApJ*, 1973, vol. 179, p. 731
- Fabian A. C., Nulsen P. E. J., Subsonic accretion of cooling gas in clusters of galaxies., *MNRAS*, 1977, vol. 180, p. 479
- Fabian A. C., Nulsen P. E. J., Canizares C. R., Cooling flows in clusters of galaxies, *Nature*, 1984, vol. 310, p. 733
- Fabian A. C., Sanders J. S., Taylor G. B., Allen S. W., A deep Chandra observation of the Centaurus cluster: bubbles, filaments and edges, *MNRAS*, 2005, vol. 360, p. L20
- Ferreras I., Charlot S., Silk J., The Age and Metallicity Range of Early-Type Galaxies in Clusters, *ApJ*, 1999, vol. 521, p. 81

- Gastaldello F., Ghizzardi S., Marelli M., Salvetti D., Molendi S., De Luca A., Moretti A., Rossetti M., Tiengo A., A systematic analysis of the XMM-Newton background: IV. Origin of the unfocused and focused components, *Experimental Astronomy*, 2017, vol. 44, p. 321
- Ghizzardi S., Marelli M., Salvetti D., Gastaldello F., Molendi S., De Luca A., Moretti A., Rossetti M., Tiengo A., A systematic analysis of the XMM-Newton background: III. Impact of the magnetospheric environment, *Experimental Astronomy*, 2017, vol. 44, p. 273
- Gladders M. D., Yee H. K. C., A New Method For Galaxy Cluster Detection. I. The Algorithm, *AJ*, 2000, vol. 120, p. 2148
- Heckman T. M., Armus L., Miley G. K., On the Nature and Implications of Starburst-driven Galactic Superwinds, *ApJS*, 1990, vol. 74, p. 833
- Henning J. W., Gantner B., Burns J. O., Hallman E. J., On the Origin of Cool Core Galaxy Clusters: Comparing X-ray Observations with Numerical Simulations, *ApJ*, 2009, vol. 697, p. 1597
- Hjorth J., Oukbir J., van Kampen E., The mass-temperature relation for clusters of galaxies, *MNRAS*, 1998, vol. 298, p. L1
- Hoskin M. A., The 'Great Debate': What Really Happened, *Journal for the History of Astronomy*, 1976, vol. 7, p. 169
- Hudson D. S., Mittal R., Reiprich T. H., Nulsen P. E. J., Andernach H., Sarazin C. L., What is a cool-core cluster? a detailed analysis of the cores of the X-ray flux-limited HIFLUGCS cluster sample, *A&A*, 2010, vol. 513, p. A37
- Jansen F., Lumb D., Altieri B., Clavel J., Ehle M., Erd C., Gabriel C., Guainazzi M., Gondoin P., Much R., Munoz R., Santos M., Schartel N., Texier D., Vacanti G., XMM-Newton observatory. I. The spacecraft and operations, *A&A*, 2001, vol. 365, p. L1
- Kaastra J. S., Bykov A. M., Schindler S., Bleeker J. A. M., Borgani S., Diaferio A., Dolag K., Durret F., Nevalainen J., Ohashi T., Paerels F. B. S., Petrosian V., Rephaeli Y., Richter P., Schaye J., Werner N., Clusters of Galaxies: Beyond the Thermal View, *Space Sci. Rev.*, 2008, vol. 134, p. 1
- Kaastra J. S., Ferrigno C., Tamura T., Paerels F. B. S., Peterson J. R., Mittaz J. P. D., XMM-Newton observations of the cluster of galaxies Sérsic 159-03, *A&A*, 2001, vol. 365, p. L99
- Kodama T., Bower R. G., Reconstructing the history of star formation in rich cluster cores, *MNRAS*, 2001, vol. 321, p. 18
- Kuntz K., Collier M. R., Robertson I., Hansen K., Snowden S. L., Cravens T., Quantifying the Exospheric Component of Soft X-ray Emission. In *AGU Fall Meeting Abstracts*, vol. 2007, 2007, p. SH12A

- Laganá T. F., Martinet N., Durret F., Lima Neto G. B., Maughan B., Zhang Y. Y., A comprehensive picture of baryons in groups and clusters of galaxies, *A&A*, 2013, vol. 555, p. A66
- Leccardi A., Rossetti M., Molendi S., Thermo-dynamic and chemical properties of the intra-cluster medium, *A&A*, 2010, vol. 510, p. A82
- Li Y., Ruszkowski M., Bryan G. L., AGN Heating in Simulated Cool-core Clusters, *ApJ*, 2017, vol. 847, p. 106
- Margoniner V. E., de Carvalho R. R., Gal R. R., Djorgovski S. G., The Butcher-Oemler Effect in 295 Clusters: Strong Redshift Evolution and Cluster Richness Dependence, *ApJ*, 2001, vol. 548, p. L143
- Marian V., Ziegler B., Kuchner U., Verdugo M., Color gradients reflect an inside-out growth in early-type galaxies of the cluster MACS J1206.2-0847, *A&A*, 2018, vol. 617, p. A34
- Maughan B. J., Giles P. A., Randall S. W., Jones C., Forman W. R., Self-similar scaling and evolution in the galaxy cluster X-ray luminosity-temperature relation, *MNRAS*, 2012, vol. 421, p. 1583
- Mernier F., Biffi V., Yamaguchi H., Medvedev P., Simionescu A., Ettori S., Werner N., Kaastra J. S., de Plaa J., Gu L., Enrichment of the Hot Intracluster Medium: Observations, *Space Sci. Rev.*, 2018, vol. 214, p. 129
- Mushotzky R. F., Loewenstein M., Lack of Evolution in the Iron Abundance in Clusters of Galaxies and Implications for the Global Star Formation Rate at High Redshift, *ApJ*, 1997, vol. 481, p. L63
- Nulsen P. E. J., Thermal instability in cooling flows., *MNRAS*, 1986, vol. 221, p. 377
- Peterson J. R., Fabian A. C., X-ray spectroscopy of cooling clusters, *Phys. Rep.*, 2006, vol. 427, p. 1
- Peterson J. R., Paerels F. B. S., Kaastra J. S., Arnaud M., Reiprich T. H., Fabian A. C., Mushotzky R. F., Jernigan J. G., Sakelliou I., X-ray imaging-spectroscopy of Abell 1835, *A&A*, 2001, vol. 365, p. L104
- Pimblet K. A., Smail I., Kodama T., Couch W. J., Edge A. C., Zabludoff A. I., O'Hely E., The Las Campanas/AAT Rich Cluster Survey - II. The environmental dependence of galaxy colours in clusters at $z \sim 0.1$, *MNRAS*, 2002, vol. 331, p. 333
- Pratt G. W., Böhringer H., Croston J. H., Arnaud M., Borgani S., Finoguenov A., Temple R. F., Temperature profiles of a representative sample of nearby X-ray galaxy clusters, *A&A*, 2007, vol. 461, p. 71
- Prestwich A. H., Joy M., Cooling Flows and the Formation of Massive Halos in cD Galaxies, *ApJ*, 1991, vol. 369, p. L1
- Rybicki G. B., Lightman A. P., *Radiative Processes in Astrophysics*, 1986
- Sarazin C. L., X-ray emission from clusters of galaxies, *Reviews of Modern Physics*, 1986, vol. 58, p. 1

-
- Scott D. W., *Multivariate Density Estimation: Theory, Practice, and Visualization*. Wiley-Blackwell, 2015
- Shane C. D., Wirtanen C. A., The distribution of extragalactic nebulae, *AJ*, 1954, vol. 59, p. 285
- Shapley H., Luminosity Distribution and Average Density of Matter in Twenty-Five Groups of Galaxies, *Proceedings of the National Academy of Science*, 1933, vol. 19, p. 591
- Silverman B. W., *Density estimation for statistics and data analysis*. Routledge, 1986
- Snowden S. L., , 1998 A New View of the LHB and 1/4 keV X-ray Halo. Springer-Verlag pp 103–112
- Snowden S. L., Mushotzky R. F., Kuntz K. D., Davis D. S., A catalog of galaxy clusters observed by XMM-Newton, *A&A*, 2008, vol. 478, p. 615
- Strüder L., Briel U., Dennerl K., Hartmann R., Kendziorra E., Meidinger N., Pfeffermann E., Reppin C., Aschenbach B., Bornemann W., Bräuninger H., The European Photon Imaging Camera on XMM-Newton: The pn-CCD camera, *A&A*, 2001, vol. 365, p. L18
- Terlevich A. I., Kuntschner H., Bower R. G., Caldwell N., Sharples R. M., Colour-magnitude relations and spectral line strengths in the Coma cluster, *MNRAS*, 1999, vol. 310, p. 445
- Turner M. J. L., Abbey A., Arnaud M., Balasini M., Barbera M., Belsole E., Bennie P. J., Bernard J. P., Bignami G. F., Boer M., Briel U., Butler I., Cara C., Chabaud C., Cole R., Collura A., Conte M., Cros A., Denby M., Dhez P., The European Photon Imaging Camera on XMM-Newton: The MOS cameras, *A&A*, 2001, vol. 365, p. L27
- Umetsu K., Cluster-galaxy weak lensing, *A&A Rev.*, 2020, vol. 28, p. 7
- Visvanathan N., Sandage A., The color - absolute magnitude relation for E and S0 galaxies. I. Calibration and tests for universality using Virgo and eight other nearby clusters., *ApJ*, 1977, vol. 216, p. 214
- Vogelsberger M., Marinacci F., Torrey P., Genel S., Springel V., Weinberger R., Pakmor R., Hernquist L., Naiman J., Pillepich A., Nelson D., The uniformity and time-invariance of the intra-cluster metal distribution in galaxy clusters from the IllustrisTNG simulations, *MNRAS*, 2018, vol. 474, p. 2073
- York D. G., Adelman J., Anderson SDSS Collaboration The Sloan Digital Sky Survey: Technical Summary, *AJ*, 2000, vol. 120, p. 1579
- Zwicky F., Herzog E., Wild P., *Catalogue of galaxies and of clusters of galaxies*. CalTech, 1968

Appendix

Appendix A

Temperature and metallicity profiles

In this appendix, we present the temperature and metallicity radial profiles of our cluster sample. Their extraction is obtained following the method outlined in chapter 4.

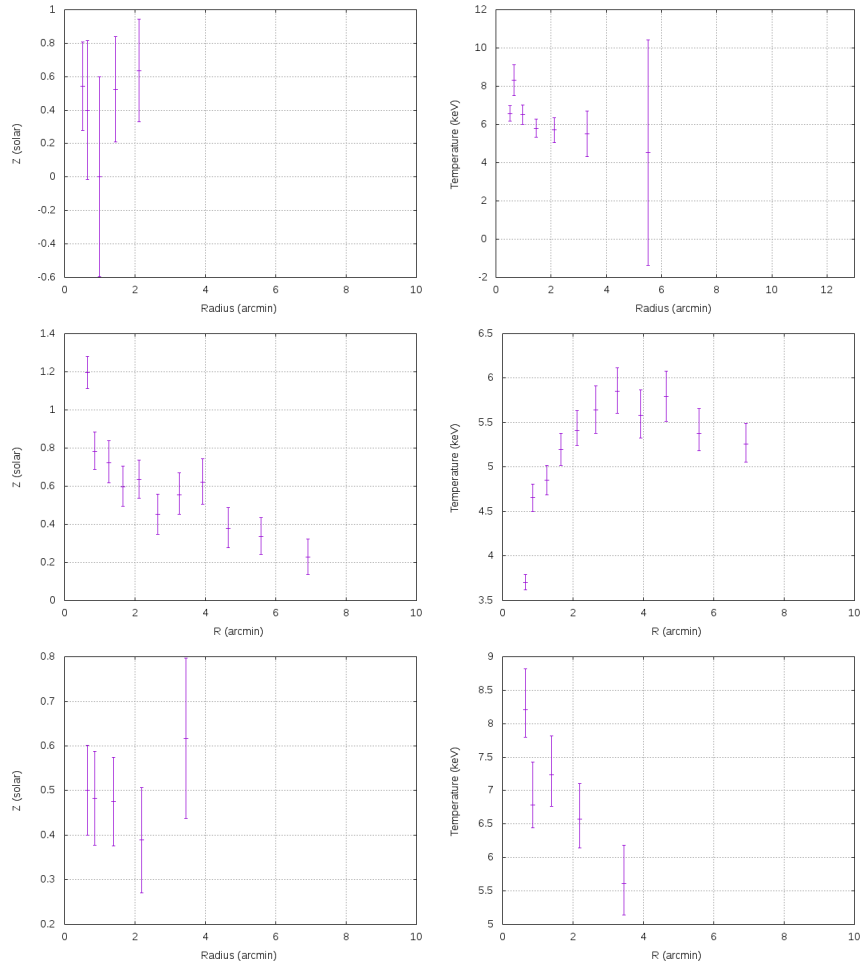


Figure A.1: RXCJ0043.4-2037, Abell 85, Abell 773.

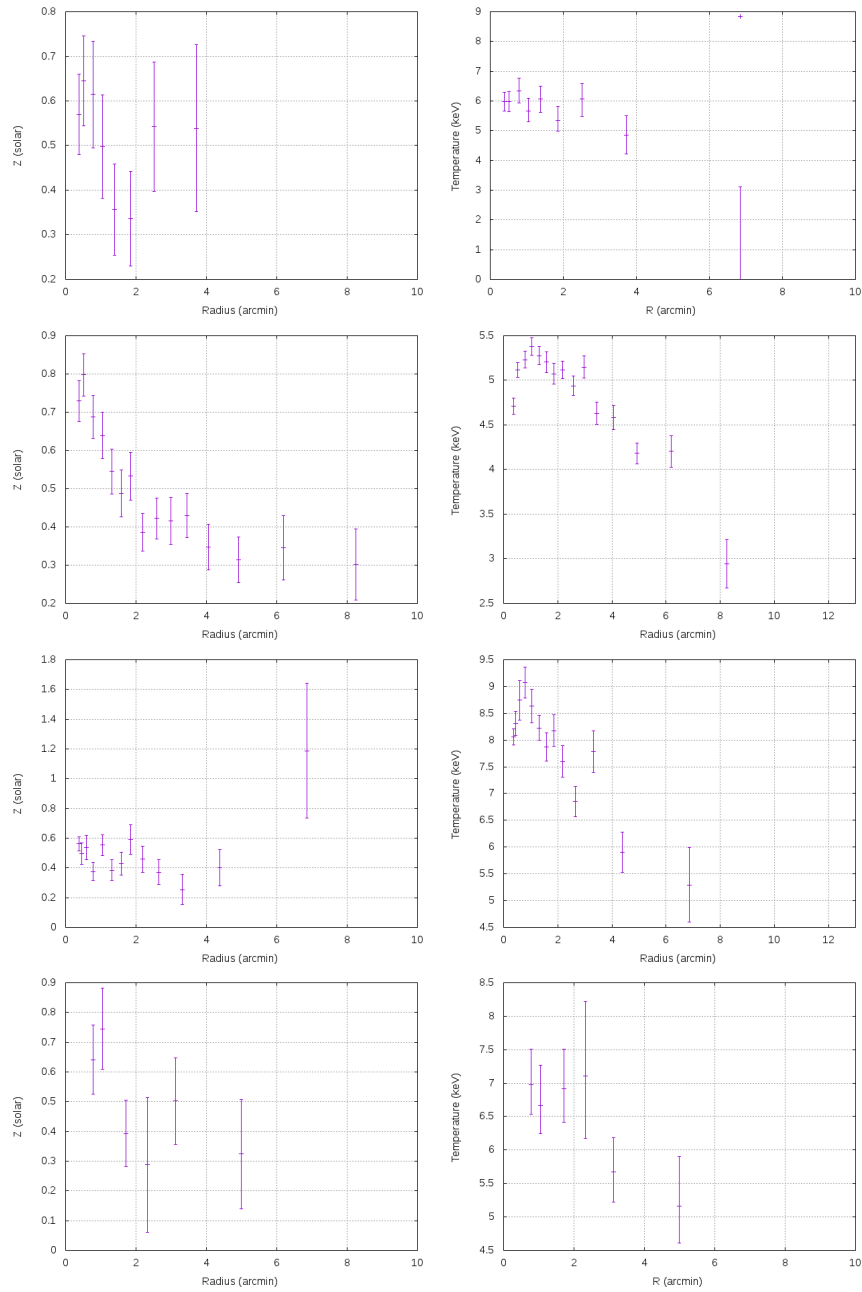


Figure A.2: Abell 963, Abell 1650, Abell 1689, Abell 1763.

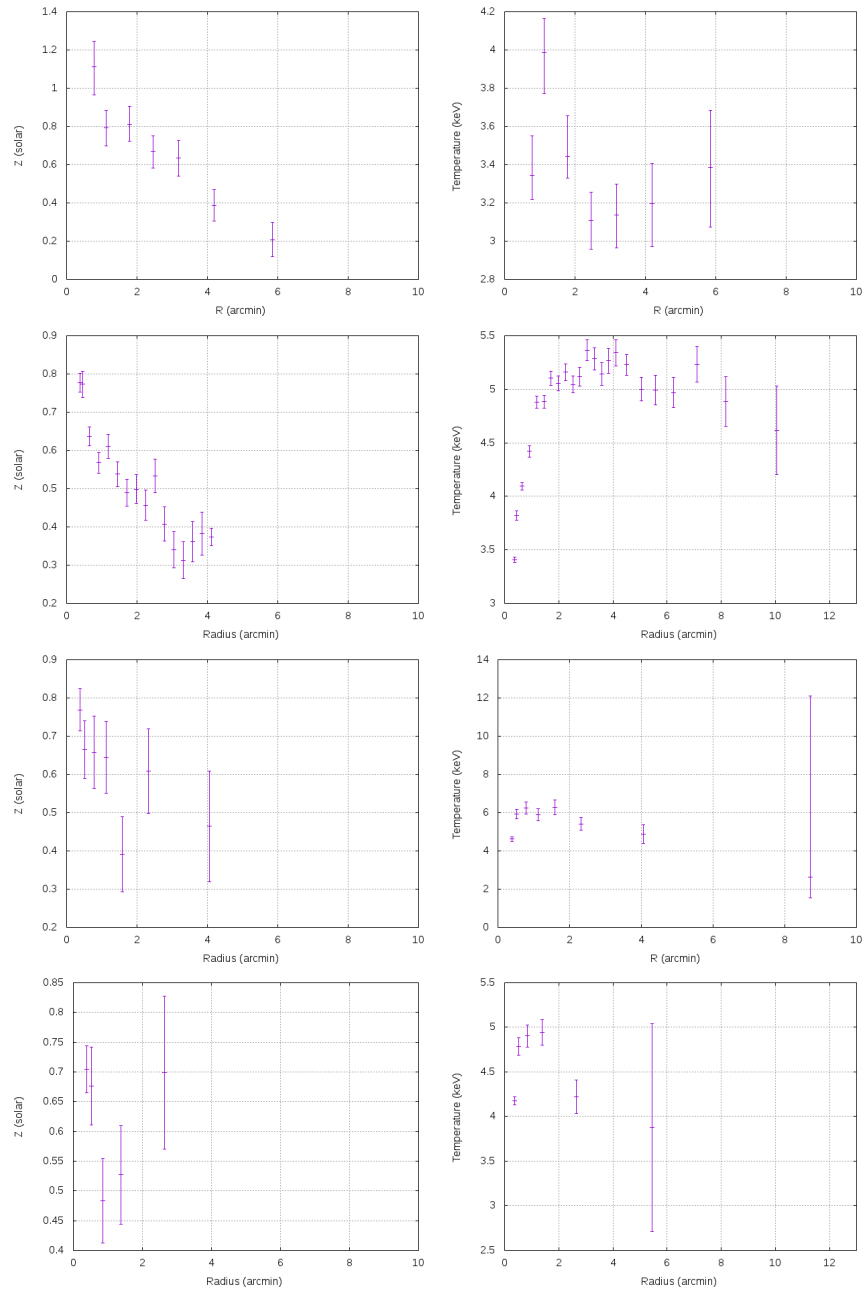


Figure A.3: Abell 1775, Abell 1795, RXJ2129.6+0005, E1455+2232.

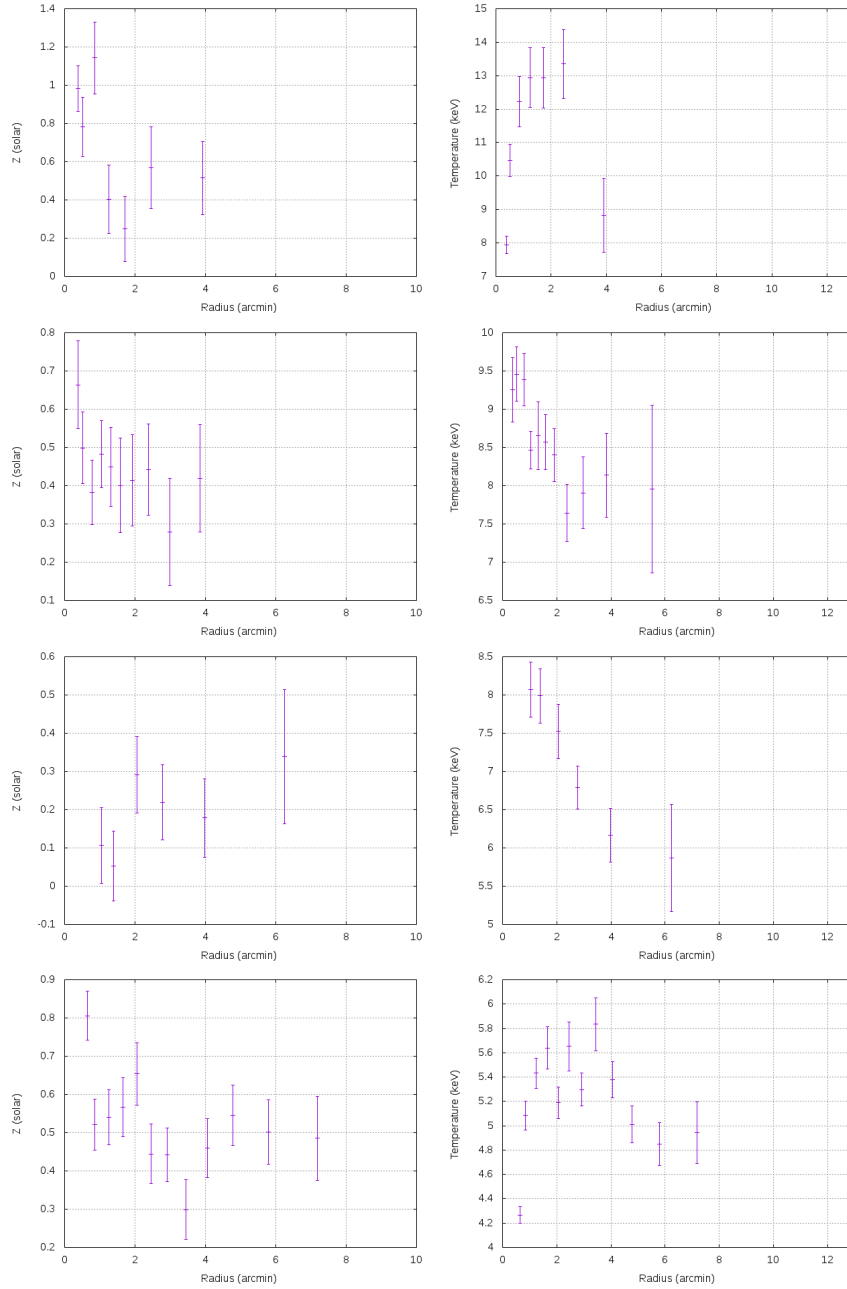


Figure A.4: Abell 2390, Abell 1914, Abell 2034, Abell 2065.

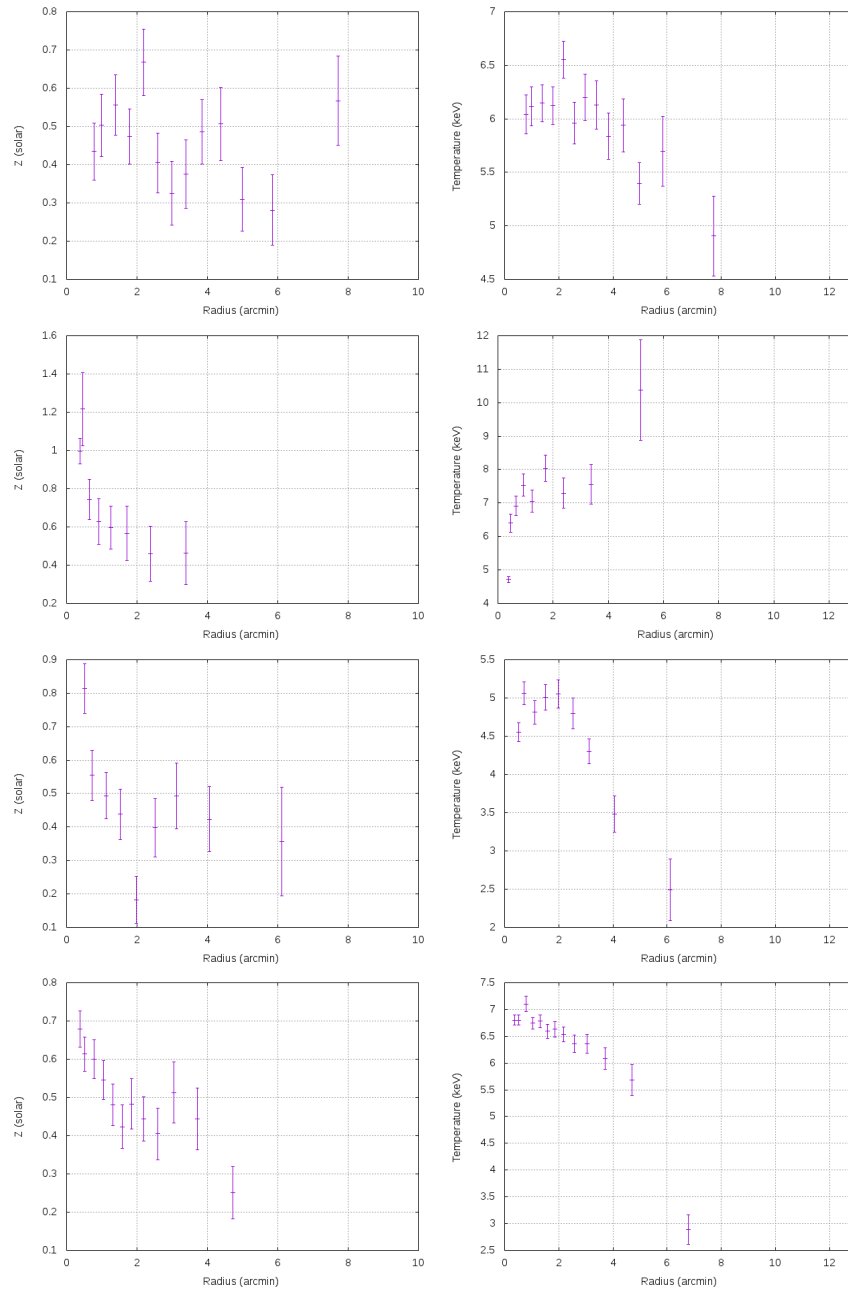


Figure A.5: ZwCl1215, RXCJ1720.1+2638, Abell 1201, Abell 1413.

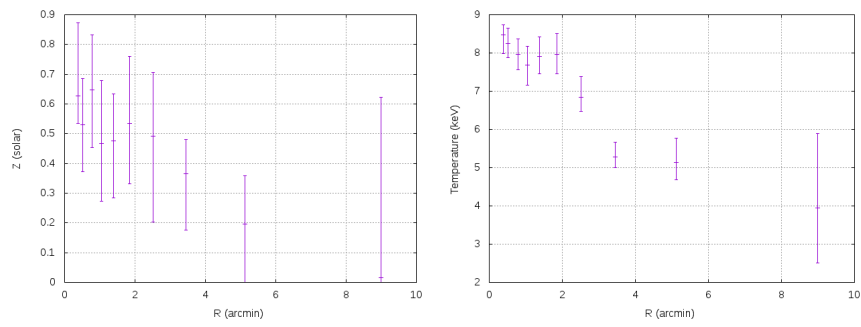


Figure A.6: Abell 2261.

Appendix B

Color-magnitude diagrams and probability density functions (KDEs)

This section contains the probability density functions (PDFs), representing the distribution of galaxies in the color-magnitude diagram, generated by our method using KDEs for each galaxy cluster (described in section 5). The *clean* PDFs are calculated using equation 5.15.

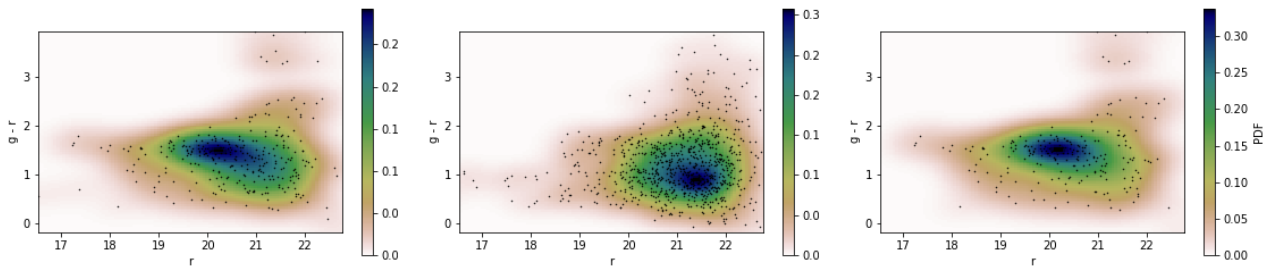


Figure B.1: RXCJ0043.4-2037 dirty, field, and clean.

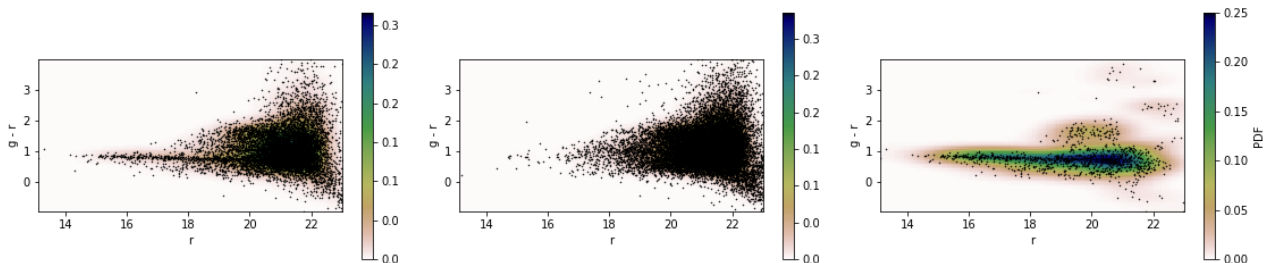


Figure B.2: Abell 85 dirty, field, and clean.

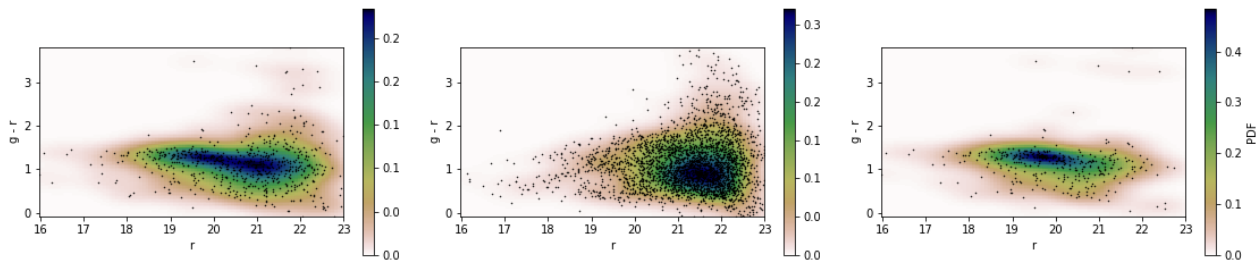


Figure B.3: Abell 773 dirty, field, clean.

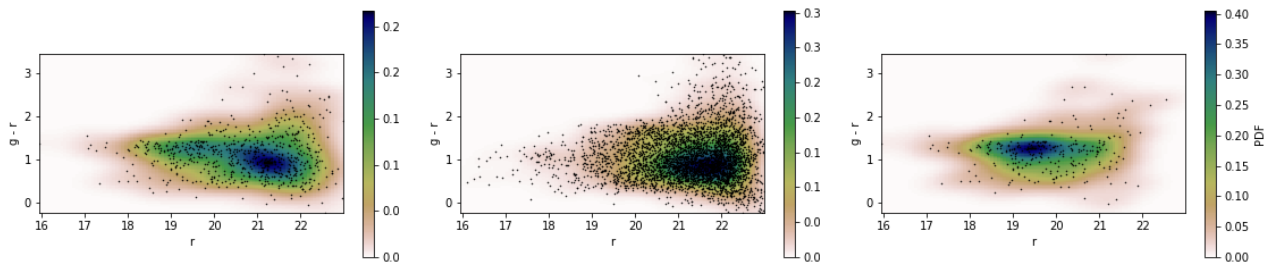


Figure B.4: Abell 963 dirty, field, clean.

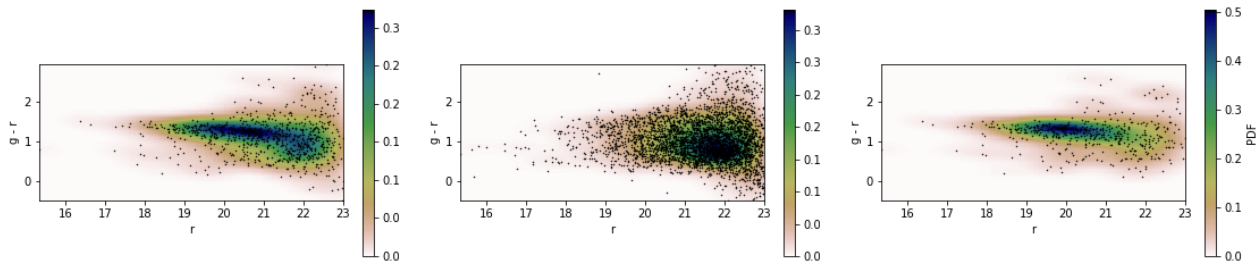


Figure B.5: Abell 1763 dirty, field, clean.

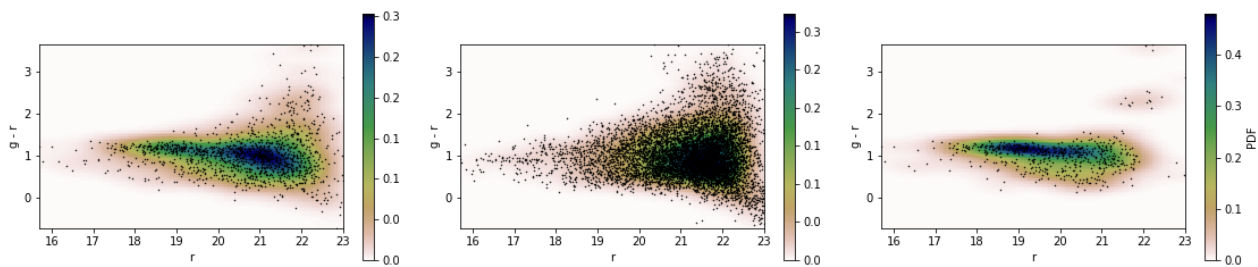


Figure B.6: Abell 1689 dirty, field, clean.

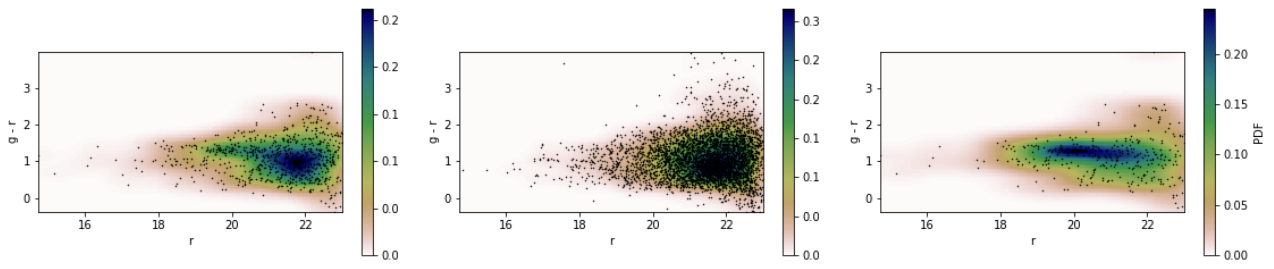


Figure B.7: RXJ2129.6+0005 dirty, field, clean.

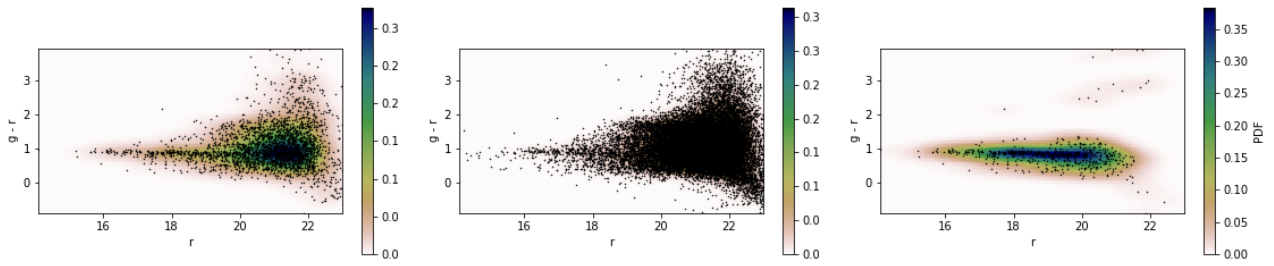


Figure B.8: Abell 1650 dirty, field, clean.

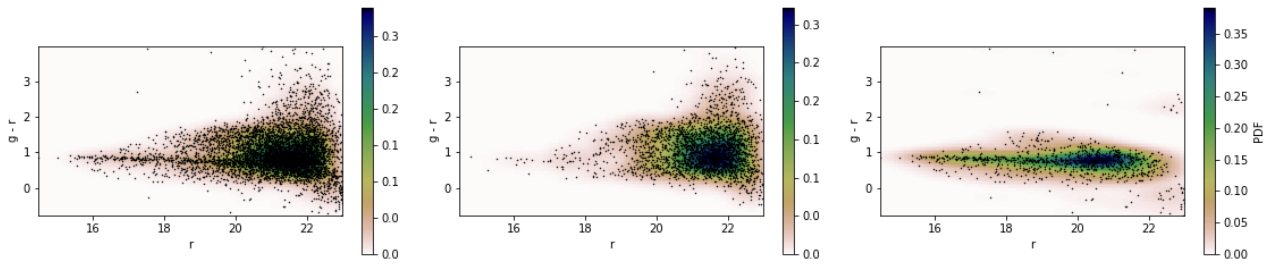


Figure B.9: Abell 1795 dirty, field, clean.

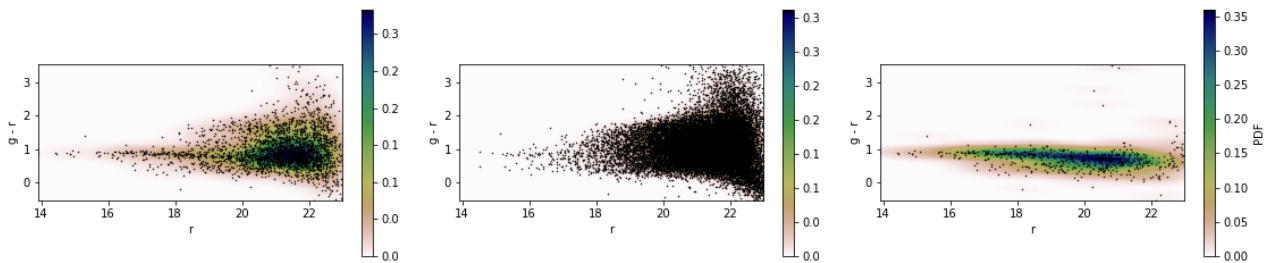


Figure B.10: Abell 1775 dirty, field, clean.

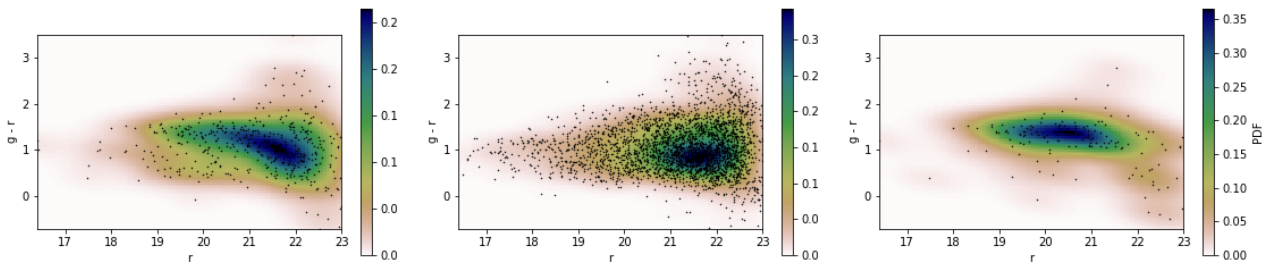


Figure B.11: NSCS-J—E1455+2232 dirty, field, clean.

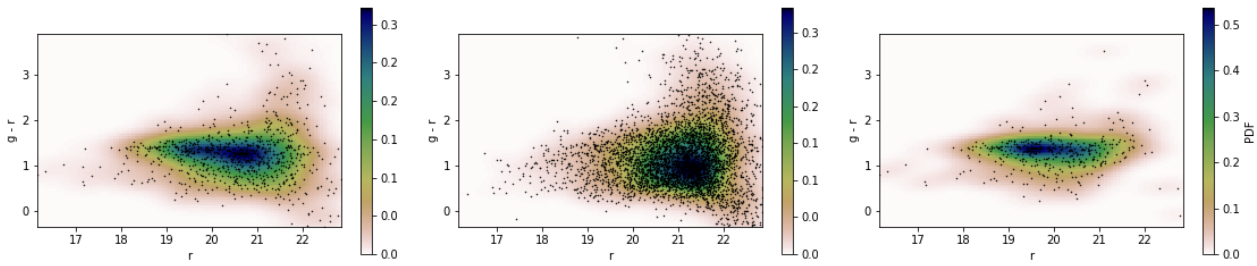


Figure B.12: Abell 2390 dirty, field, clean.

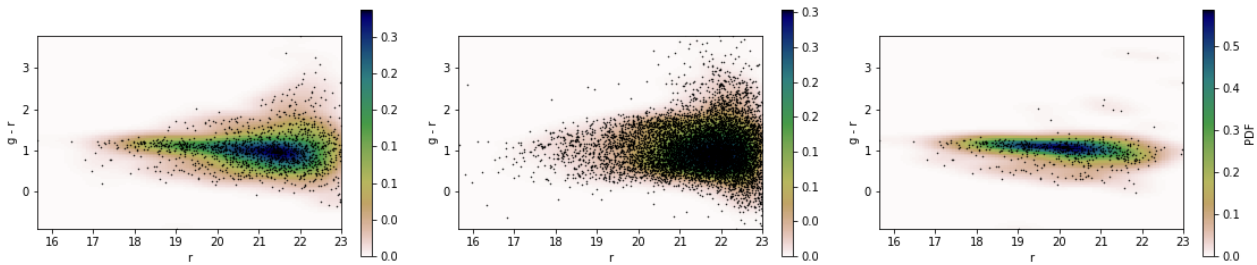


Figure B.13: Abell 1914 dirty, field, clean.

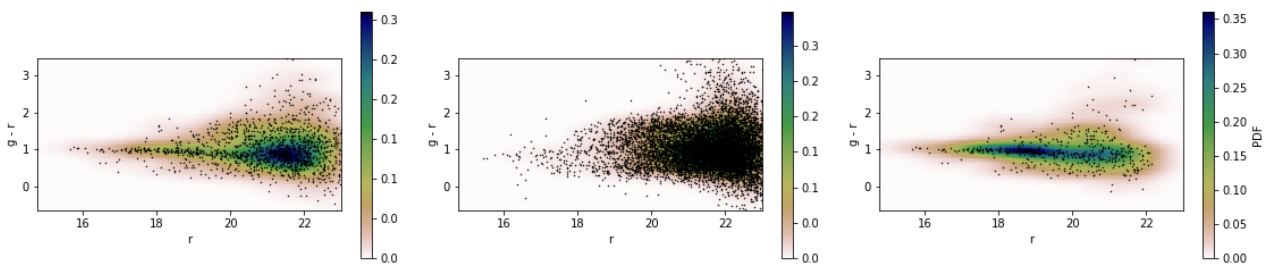


Figure B.14: Abell 2034 dirty, field, clean.

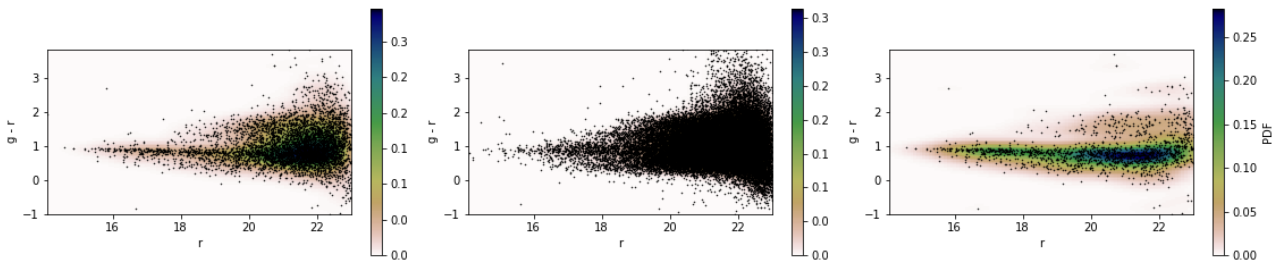


Figure B.15: Abell 2065 dirty, field, clean.

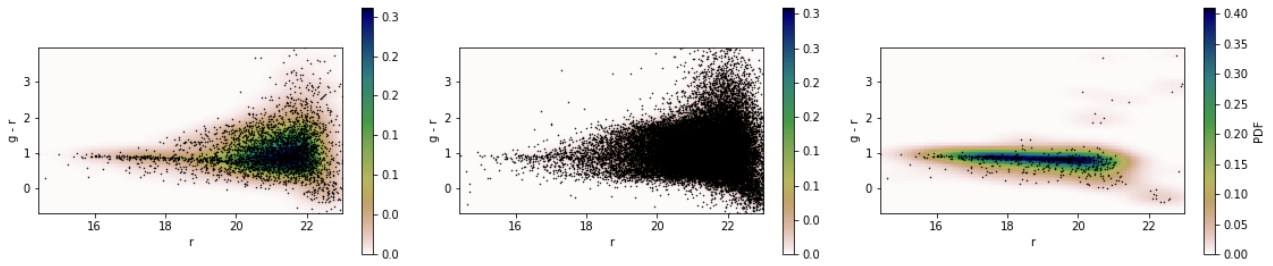


Figure B.16: ZwCL 1215 dirty, field, clean.

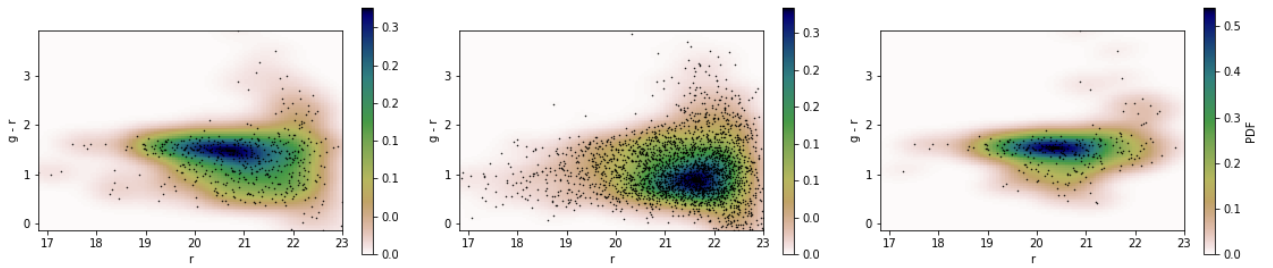


Figure B.17: Abell 781 dirty, field, clean.

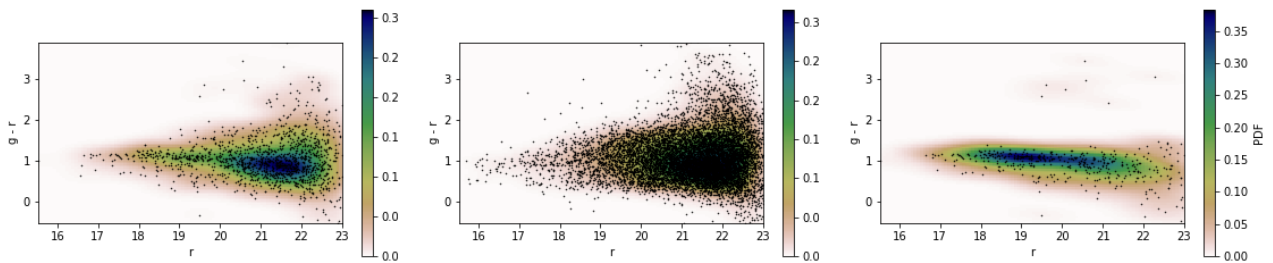


Figure B.18: RXCJ1720.1+2638 dirty, field, clean.

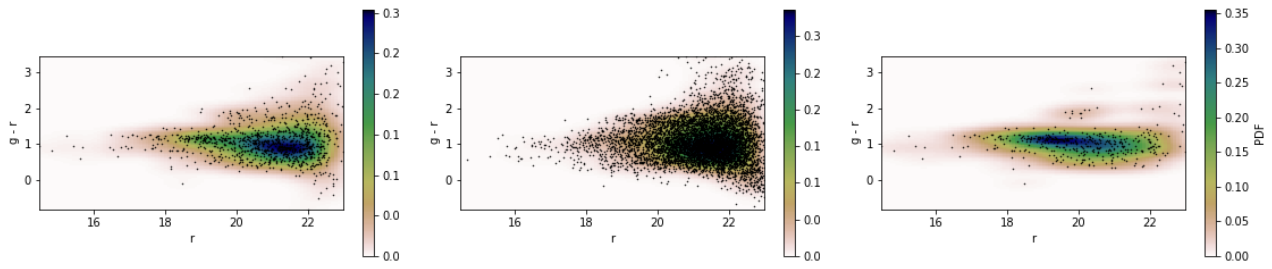


Figure B.19: Abell 1201 dirty, field, clean.

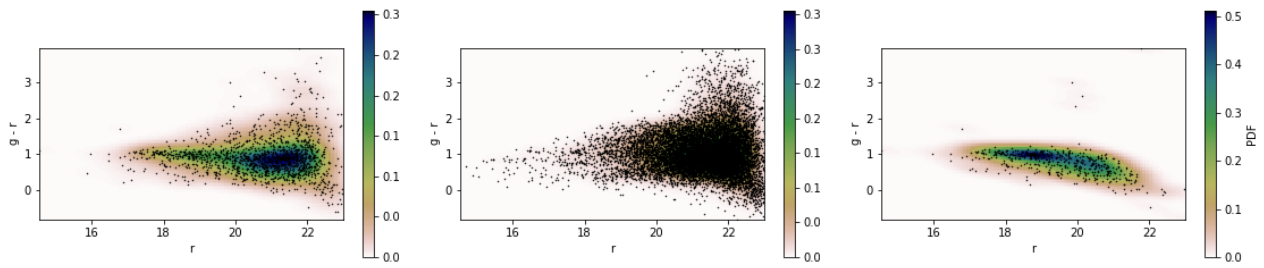


Figure B.20: Abell 1413 dirty, field, clean.

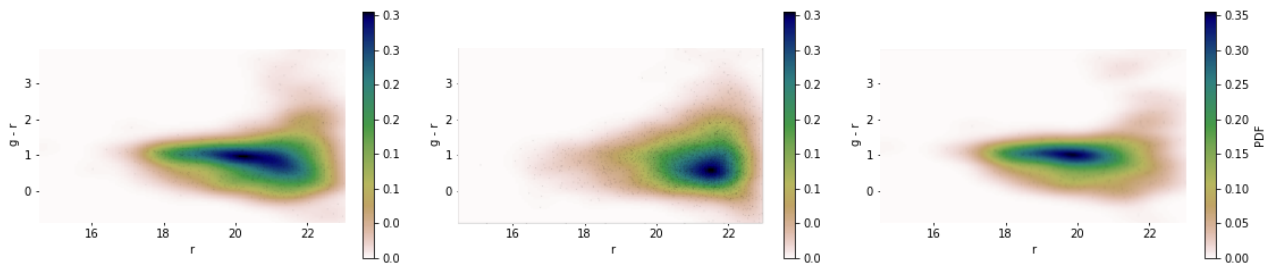


Figure B.21: Abell 2261 dirty, field, clean.

Appendix C

Model particle background subtracted images

In this appendix, we show exposure corrected images of our cluster sample with the model particle background subtracted, in the energy band 400 – 7200 eV. They are the product of the tasks *mos-back*, *pn-back* and *adapt* from the ESAS package. They are the combined images from the three detectors, MOS1, MOS2 and pn. They cover the full 30 arcmin FoV of the EPIC camera, with colors in a logarithmic scale. They are also smoothed by a circular kernel of radius encompassing a minimum of 50 counts, with the original central pixel given the average surface brightness of the pixels within the circle.

For Abell 1775, RXCJ1720.1+2638 and RXJ2129.6+0005 it was not possible to create images with the particle background subtracted due to a bug of unknown cause internal to some of the ESAS tasks.

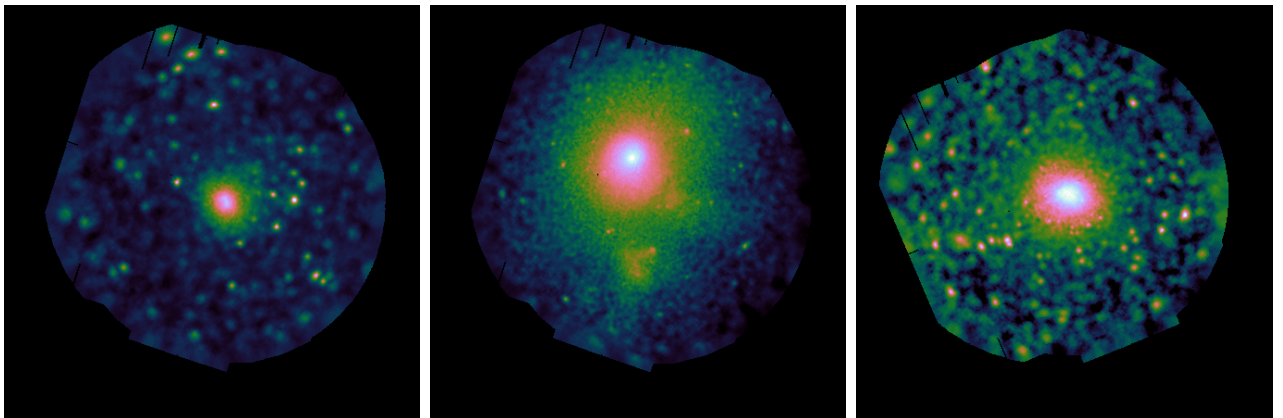


Figure C.1: RXCJ0043.4-2037, Abell 85, Abell 773

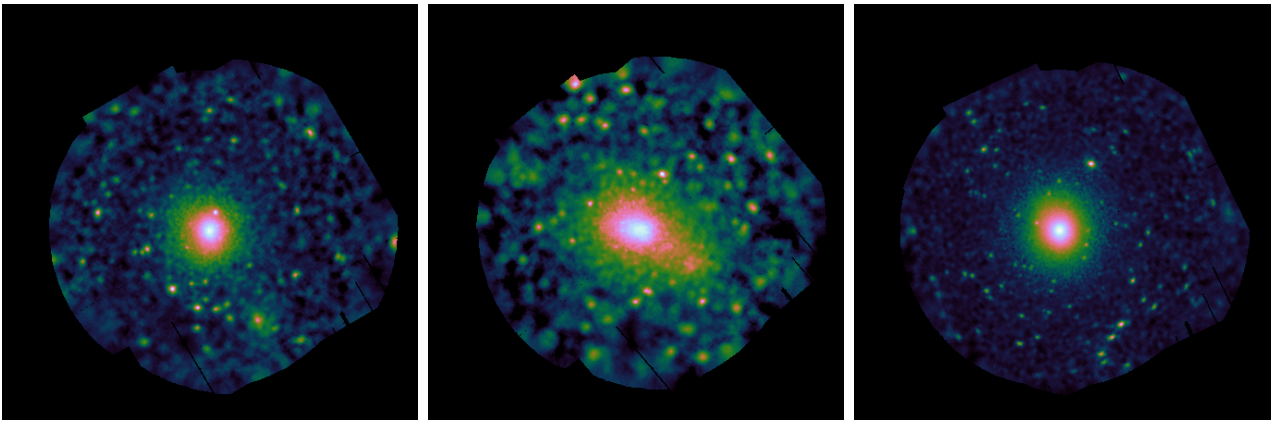


Figure C.2: Abell 963, Abell 1763, Abell 1689

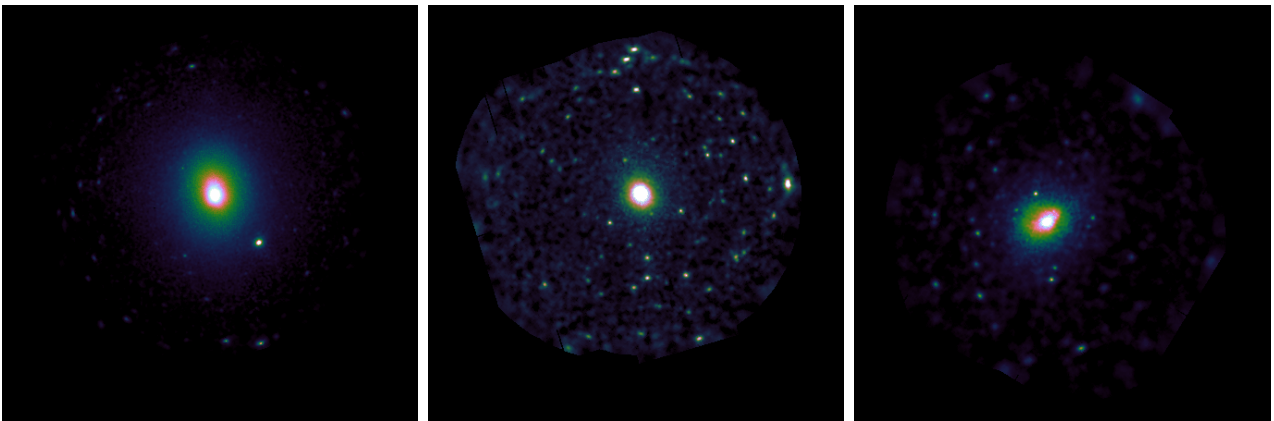


Figure C.3: Abell 1795, E1455+2232, Abell 2390

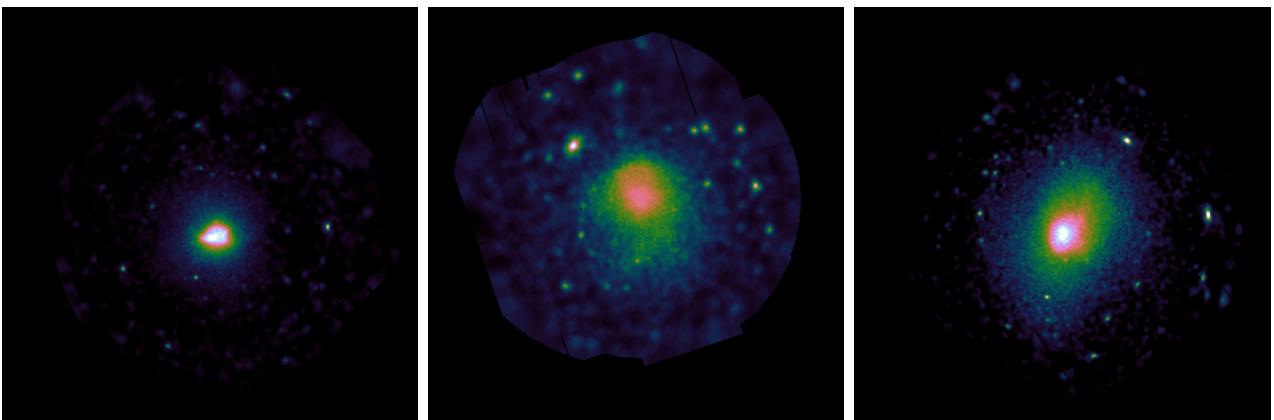


Figure C.4: Abell 1914, Abell 2034, Abell 2065

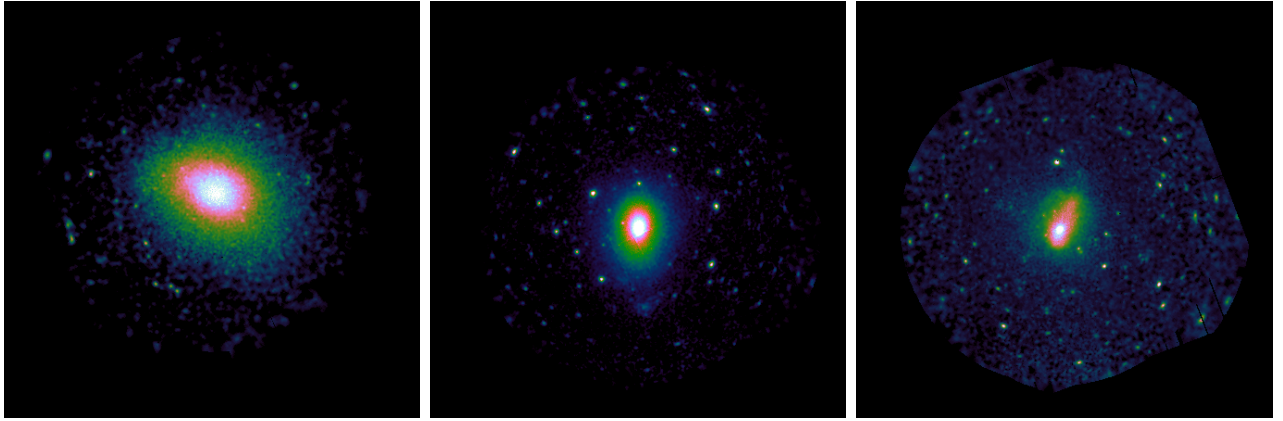


Figure C.5: ZwCl1215, Abell 1413, Abell 1201

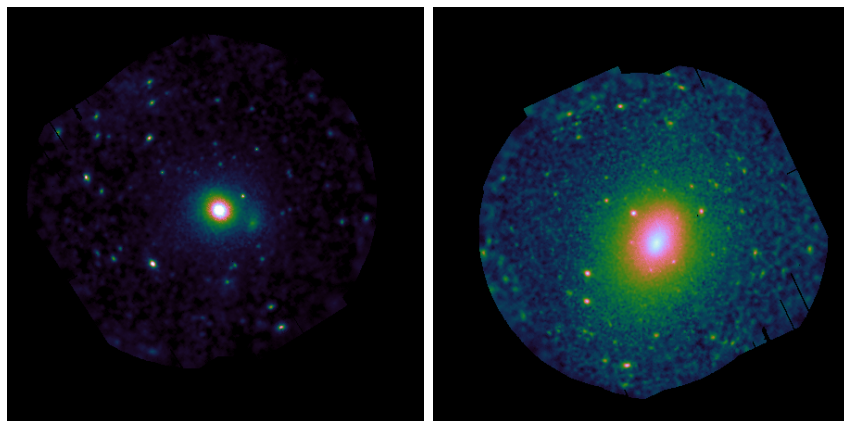


Figure C.6: Abell 2261, Abell 1650.